

VOLUME 33

AUGUST 1955

NUMBER 8

# Canadian Journal of Physics

**Editor:** G. M. VOLKOFF

**Associate Editors:**

L. G. ELLIOTT, *Atomic Energy of Canada, Ltd., Chalk River*  
J. S. FOSTER, *McGill University*  
G. HERZBERG, *National Research Council of Canada*  
L. LEPRINCE-RINGUET, *Ecole Polytechnique, Paris*  
D. W. R. MCKINLEY, *National Research Council of Canada*  
B. W. SARGENT, *Queen's University*  
Sir FRANCIS SIMON, *Clarendon Laboratory, University of Oxford*  
W. H. WATSON, *University of Toronto*

**Published by THE NATIONAL RESEARCH COUNCIL**  
**OTTAWA** **CANADA**

## CANADIAN JOURNAL OF PHYSICS

(Formerly Section A, Canadian Journal of Research)

Under the authority of the Chairman of the Committee of the Privy Council on Scientific and Industrial Research, the National Research Council issues THE CANADIAN JOURNAL OF PHYSICS and six other journals devoted to the publication, in English or French, of the results of original scientific research. Matters of general policy concerning these journals are the responsibility of a joint Editorial Board consisting of: members representing the National Research Council of Canada; the Editors of the Journals; and members representing the Royal Society of Canada and four other scientific societies.

### EDITORIAL BOARD

#### Representatives of the National Research Council

A. N. Campbell, *University of Manitoba*      E. G. D. Murray, *McGill University*  
G. E. Hall, *University of Western Ontario*      D. L. Thomson, *McGill University*  
W. H. Watson (Chairman), *University of Toronto*

#### Editors of the Journals

D. L. Bailey, *University of Toronto*      G. A. Ledingham, *National Research Council*  
T. W. M. Cameron, *Macdonald College*      Léo Marion, *National Research Council*  
J. B. Collip, *University of Western Ontario*      R. G. E. Murray, *University of Western Ontario*  
G. M. Volkoff, *University of British Columbia*

#### Representatives of Societies

D. L. Bailey, *University of Toronto*      R. G. E. Murray, *University of Western Ontario*  
Royal Society of Canada      Canadian Society of Microbiologists  
T. W. M. Cameron, *Macdonald College*      H. G. Thode, *McMaster University*  
Royal Society of Canada      Chemical Institute of Canada  
J. B. Collip, *University of Western Ontario*      T. Thorvaldson, *University of Saskatchewan*  
Canadian Physiological Society      Royal Society of Canada  
G. M. Volkoff, *University of British Columbia*  
Royal Society of Canada; Canadian Association of Physicists

#### Ex officio

Léo Marion (Editor-in-Chief), *National Research Council*

*Manuscripts* for publication should be submitted to Dr. Léo Marion, Editor-in-Chief, Canadian Journal of Physics, National Research Council, Ottawa 2, Canada.

(For instructions on preparation of copy, see **Notes to Contributors** (inside back cover).)

*Proof, correspondence concerning proof, and orders for reprints* should be sent to the Manager, Editorial Office (Research Journals), Division of Administration, National Research Council, Ottawa 2, Canada.

*Subscriptions, renewals, requests for single or back numbers, and all remittances* should be sent to Division of Administration, National Research Council, Ottawa 2, Canada. Remittances should be made payable to the Receiver General of Canada, credit National Research Council.

The journals published, frequency of publication, and prices are:

Canadian Journal of Biochemistry and Physiology	Bimonthly	\$3.00 a year
Canadian Journal of Botany	Bimonthly	\$4.00 a year
Canadian Journal of Chemistry	Monthly	\$5.00 a year
Canadian Journal of Microbiology*	Bimonthly	\$3.00 a year
Canadian Journal of Physics	Monthly	\$4.00 a year
Canadian Journal of Technology	Bimonthly	\$3.00 a year
Canadian Journal of Zoology	Bimonthly	\$3.00 a year

The price of single numbers of all journals is 75 cents.

\*Volume 1 will combine three numbers published in 1954 with six published in 1955 and will be available at the regular annual subscription rate of \$3.00.







# Canadian Journal of Physics

Issued by THE NATIONAL RESEARCH COUNCIL OF CANADA

VOLUME 33

AUGUST 1955

NUMBER 8

## A STUDY OF NUCLEON FORCES WITH REPULSIVE CORES

### I. THE EFFECT OF CORES OF FINITE STRENGTH<sup>1</sup>

By J. R. BIRD<sup>2</sup> AND M. A. PRESTON<sup>3</sup>

#### ABSTRACT

A general study of nucleon potentials with repulsive cores has been made. In this paper, consideration is given to repulsions of finite strength and, for an exponential attractive potential and for the  $^1S$   $n$ - $p$  system, it is shown to what accuracy the core may be replaced by an infinite one with a smaller radius.

#### A. INTRODUCTION

In recent years there has been considerable interest in the possibility that the force between two nucleons, attractive for separations greater than  $1 \times 10^{-13}$  cm., may become repulsive at smaller distances. This suggestion was made by Jastrow (6) after the analyses of high energy scattering made by Christian and Hart (3) and Christian and Noyes (4) showed that the hypothesis of charge independence for the neutron-proton and proton-proton forces fails for monotonic attractive potentials. The neutron-proton differential cross-section is almost symmetric about  $90^\circ$  in the center-of-mass coordinate system, indicating that the interaction is very small in states with odd angular momentum. Such an interaction would give only singlet scattering in the proton-proton case, and because of the relative signs of alternate even Legendre polynomials at  $90^\circ$ , the  $p$ - $p$  cross-section would be strongly peaked in the forward direction, provided the phase shifts all had the same sign. However, the actual cross-section is almost isotropic. Assuming potentials everywhere attractive, and therefore phase shifts always positive, Christian and Noyes were led to introduce a strong tensor force in odd states in the proton-proton interaction, thus abandoning charge independence. On the other hand a short range repulsive region surrounded by an attractive potential will produce phase shifts which may change sign as the energy increases. Jastrow showed, by approximate numerical calculation, that charge independence may be maintained and that rough agreement with experimental cross-sections is obtained with an impenetrable core of radius  $0.6 \times 10^{-13}$  cm.

<sup>1</sup>Manuscript received April 21, 1955.

Contribution from Physics Department, University of Toronto, Toronto, Ontario, and Hamilton College, McMaster University, Hamilton, Ontario. Partially supported by a grant from the National Research Council.

<sup>2</sup>Holder of a McKee-Gilchrist Scholarship 1950-1951. Present address: College of Arts and Science, Baghdad, Iraq.

<sup>3</sup>Present address: Hamilton College, McMaster University, Hamilton, Ontario.

in the singlet state and suitable attractive potentials outside this core and in the triplet state. Later Lévy (8) demonstrated on the basis of pseudoscalar meson theory that there are theoretical grounds to expect the potential between two nucleons at low energies to contain a repulsive core.\* It therefore seemed advisable to make a careful study of the properties of repulsive core potentials, at least in those lower energy regions where a potential description of nucleon forces is appropriate.

The nucleon scattering cross-sections can be analyzed in terms of the phase-shifts appropriate to the various values of angular momentum present. It is well known that there exist expansions in powers of the energy for suitable functions of these phase-shifts (e.g., 1, 2, 5). For *S*-state neutron-proton scattering this expansion is

$$[A. 1] \quad k \cot \delta = -a^{-1} + \frac{1}{2}r_0k^2 - Pr_0^3k^4 + Qr_0^5k^6 \dots$$

In this equation

$$[A. 2] \quad k^2 = 2\mu E_c/\hbar^2 = 1.205 E \times 10^{24} \text{ cm.}^{-2},$$

$\mu$  is the reduced mass of the system,  $E_c$  is the energy in the center-of-mass coordinate system,  $E$  is the energy in the laboratory coordinate system in Mev., and  $\delta$  is the *S*-wave phase-shift.

There is a similar expression for proton-proton scattering with a more complicated function of  $\delta$  on the left-hand side. In these two cases—and also for singlet and triplet states—the constants  $a$ ,  $r_0$ ,  $P$ , and  $Q$  may have different numerical values, but have the same significance, viz.  $a$  is the “scattering length”,  $r_0$  is the “effective range”, and  $P$  and  $Q$  are respectively the first and second “shape-dependent parameters”. The phase-shift at any energy and hence the values of the constants  $a$ ,  $r_0$ ,  $P$ , and  $Q$  are, of course, determined if a scattering potential is assumed. Since any nuclear potential will contain at least two constants (a range parameter and a strength parameter), the constants in any potential can be adjusted so that the values calculated for  $a$  and  $r_0$  are the experimental values found from scattering experiments at low energies, or, for the triplet state of the neutron-proton system, from the binding energy of the deuteron. Thus any reasonable shape of potential can be made to fit the low energy properties of a given spin state of a two-nucleon system. Any effects of potential shape are seen only when we consider energies sufficiently great that the terms in  $P$  and  $Q$  are important. Consequently any information which may indicate the agreement or disagreement of repulsive core potentials with experiment must come from a consideration of energies sufficiently high that at least the term in  $P$  is significant.

In later papers in this series, the values of  $P$  and  $Q$  and other low energy properties of families of potentials, all with impenetrable cores, will be presented in an attempt to determine what the core radii may be and what shapes the external attractive potential may take in order to retain agreement with experiment. A study of the possibility of retaining the charge independence

\*Lévy predicted also an explicit attractive potential. This part of his work is now known to contain errors (7), but the conclusion about the core is unaltered.

hypothesis will be included; a preliminary report of this phase of the work has already appeared (9). In this paper, we consider repulsive cores of finite strength—and hence not entirely impenetrable—and examine the effects of varying the strength. It is found that for “reasonable” core radii, and for potentials which give approximate agreement with experiment, the departures from the results for infinite cores are quite small. This is our justification for studying only infinite cores in the later papers.

### B. FINITE CORES

We study a potential  $V(r)$  for the  $S$ -state of the form

$$\begin{aligned} V &= V_i, & r < r_c, \\ \text{[B. 1]} \quad &= -V_0 \exp[-(r-r_c)/r_s], & r > r_c, \end{aligned}$$

where  $V_i$  and  $V_0$  are positive. (See Fig. 1.) Then  $r_c$  is the core radius,  $V_0$  is the maximum depth of the attractive potential (occurring at the core radius), and  $r_s$  is the range parameter. The exponential form for the attractive part

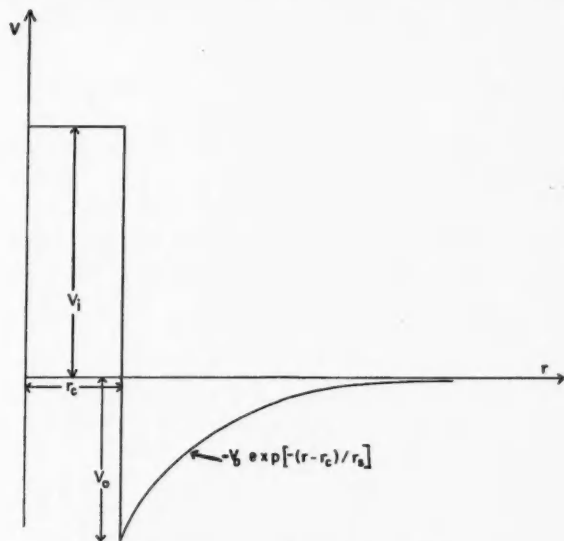


FIG. 1. A repulsive core potential.

has been chosen because analytic solutions for phase-shifts are then possible, because it is one of the shapes providing a long tail which is suggested by the experimental data (3), and because the effect of the magnitude of  $V_i$ , which we wish to investigate, is not expected to be very sensitive to the shape of the attractive part.

We proceed to find expressions for the phase-shift at any energy and for the scattering length  $a$  and the effective range  $r_0$ , which can be found in terms

of the zero-energy wave-function, confining ourselves to the singlet neutron-proton system.

Let

$$[B. 2] \quad k_i^2 = 2\mu V_i/\hbar^2, \quad k_0^2 = 2\mu V_0/\hbar^2.$$

If  $u$  is the wave function multiplied by  $r$ , we have for an  $S$ -state

$$[B. 3] \quad \frac{d^2 u}{dr^2} + (k^2 - k_i^2) u = 0, \quad r < r_c,$$

$$[B. 4] \quad y^2 \frac{d^2 u}{dy^2} + y \frac{du}{dy} + (\lambda^2 + y^2) u = 0, \quad r > r_c,$$

where

$$\begin{aligned} \lambda &= 2r_s k, \\ [B. 5] \quad \mu &= 2r_s k_0, \\ y &= \mu \exp[-(r - r_c)/2r_s]. \end{aligned}$$

The solutions are

$$[B. 6] \quad u = C_1 \sinh\{(k_i^2 - k^2)^{1/2} r\}, \quad r < r_c,$$

$$[B. 7] \quad u = C_2 J_{i\lambda}(y) + C_3 J_{-i\lambda}(y), \quad r > r_c.$$

In writing [B. 6] the condition  $u = 0$  at  $r = 0$  has been applied. Continuity of  $u$  and  $du/dr$  at  $r = r_c$  fixes  $C_2$  and  $C_3$  in terms of  $C_1$  and finally the normalization of  $u$  and, more significantly, the phase-shift are fixed by the assertion (1) that the asymptotic value of  $u$  for large  $r$  is

$$[B. 8] \quad u(r) \sim \psi(r) = \sin(kr + \delta)/\sin \delta.$$

For large  $r$ ,  $y$  is small and  $J_{i\lambda}(y) \sim (\frac{1}{2}y)^{i\lambda}/(i\lambda)!$  Using this result and the continuity conditions and the fact that  $dJ_\nu(x)/dx = \frac{1}{2}(J_{\nu-1}(x) - J_{\nu+1}(x))$ , we find

$$[B. 9] \quad \delta + kr_c = \arg\{(\frac{1}{2}\mu)^{-i\lambda}(i\lambda)![(k_i^2 - k^2)^{1/2} J_{i\lambda}(\mu) + \frac{1}{2}k_0 \tanh((k_i^2 - k^2)^{1/2} r_c)(J_{i\lambda-1}(\mu) - J_{i\lambda+1}(\mu))]\}.$$

To find the scattering length  $a$  and effective range  $r_0$ , we consider the wave-function at zero energy  $u_0(r)$  and recall that  $a$  and  $r_0$  are determined by the following two equations (1):

$$[B.10] \quad u_0(r) \sim \psi_0(r) = 1 - r/a,$$

$$[B.11] \quad r_0 = 2 \int_0^\infty [\psi_0^2(r) - u_0^2(r)] dr.$$

It is possible to let  $k$  approach zero in [B. 6] to [B. 9] but it is just as simple to repeat the calculation, writing

$$[B. 12] \quad u_0 = C_1 \sinh k_i r, \quad r < r_c,$$

$$[B. 13] \quad u_0 = C_2 J_0(y) + C_3 N_0(y), \quad r > r_c.$$

Then from the continuity at  $r = r_c$  and from the asymptotic forms

$$[B.14] \quad J_0(y) \sim 1, \quad N_0(y) \sim \frac{2}{\pi} (C + \ln \frac{1}{2}y)$$

where  $C = \text{Euler's constant } 0.577216$ , we obtain

$$[B. 15] \quad a = r_c + 2r_s \ln \frac{1}{2}\mu + 2Cr_s - \pi r_s \frac{k_0 N_1(\mu) - k_i \coth(k_i r_c) N_0(\mu)}{k_0 J_1(\mu) - k_i \coth(k_i r_c) J_0(\mu)},$$

$$[B. 16] \quad C_1 = (\pi r_s / a) k_0 [N_0(\mu) J_1(\mu) - J_0(\mu) N_1(\mu)] \\ \times [k_0 J_1(\mu) \sinh(k_i r_c) - J_0(\mu) k_i \cosh(k_i r_c)]^{-1},$$

$$[B. 17] \quad C_2 = -(\pi r_s / a) [k_0 N_1(\mu) - N_0(\mu) k_i \coth(k_i r_c)] \\ \times [k_0 J_1(\mu) - J_0(\mu) k_i \coth(k_i r_c)]^{-1},$$

$$[B. 18] \quad C_3 = \pi r_s / a.$$

Thus for a given potential we can find the zero-energy constants  $a$ ,  $r_0$  from [B. 15], [B. 16], [B. 17], [B. 18], and [B. 11] and the phase-shift  $\delta$  at any energy from [B. 9].

We have found series of potentials which are equivalent in the sense that they give the same values of  $a$ ,  $r_0$ , and the phase shift  $\delta$  at 40 Mev. The value used for  $a$  was  $-23.68 \times 10^{-13}$  cm., a good value for the singlet  $n$ - $p$  scattering length. The value used for  $\delta$  ( $40^\circ 22'$ ) is of the order of the rather uncertain experimental value and this particular number was used because it is the value obtained with Jastrow's original potential,  $V_i = \infty$ ,  $V_0 = 375$  Mev.,  $r_c = 0.60 \times 10^{-13}$  cm.,  $r_s = 0.40 \times 10^{-13}$  cm. Since the  $n$ - $p$  singlet effective range is not at present well determined, various values were used. The calculations were performed as follows. For fixed values of  $r_s$  and  $k_0$ , i.e., the range and strength of the outer potential, equations [B. 15] and [B. 9] were solved for  $r_c$  and  $k_i$  by numerical iteration. Thus for a fixed value of  $r_s$ , potentials were found, one for each value of  $r_c$ , each of which gave the desired values of  $a$  and  $\delta$ . For each such potential, the value of the effective range  $r_0$  was calculated using [B. 11]. Fig. 2 contains the results for  $r_0$ , which show that  $r_0$  is effectively determined by  $r_s$  and is only very slightly dependent on  $r_c$ . If the

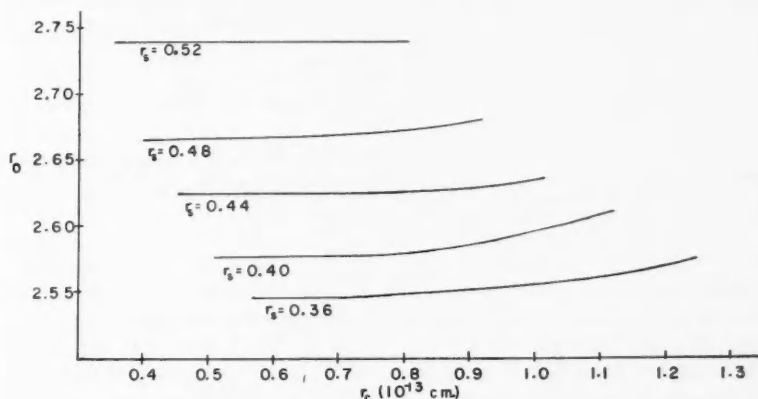


FIG. 2. The effective range  $r_0$  is shown as a function of core radius  $r_c$  for various values of the range parameter  $r_s$ . All lengths in units  $10^{-13}$  cm.

effective range were known fairly accurately, the possible values of the range parameter  $r_s$  would thus be restricted to a small interval, but a reasonable range of values would still be available for the core radius  $r_c$ . However, since the present data indicate only that  $r_0$  lies between about  $2.2$  and  $2.8 \times 10^{-13}$  cm., all of the values of  $r_s$  used in these calculations are still possible.

The values of the repulsive potential  $V_i$  are shown in Fig. 3 as functions of  $r_c$  for given values of  $r_s$  (and  $r_0$ ). The curves  $V_i = V_0$ ,  $V_i = 2V_0$ , and  $V_i$

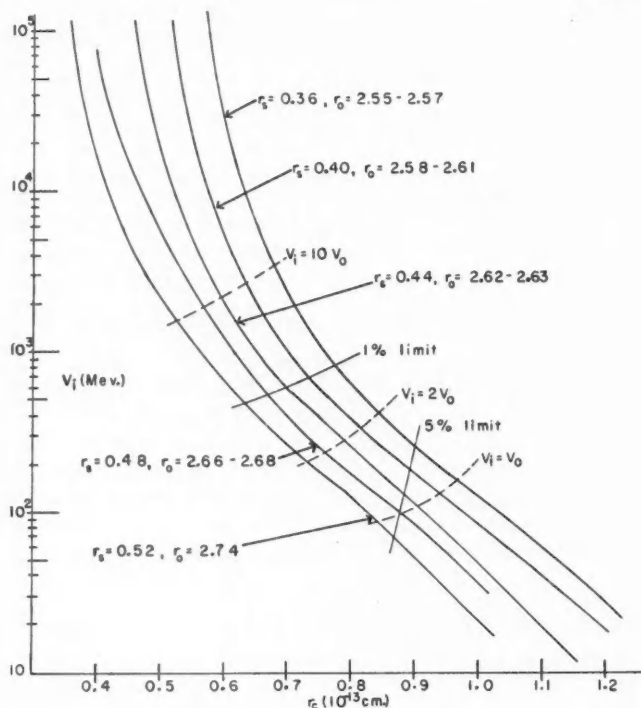


FIG. 3. The value of the repulsive core potential  $V_i$  as a function of  $r_c$  for various values of  $r_s$ . The curves for  $r_s$  are also labelled with the corresponding values of  $r_0$ . The curves  $V_i = nV_0$ ,  $n = 1, 2, 10$ , are also shown. The curves labelled "1% limit" and "5% limit" give the values of  $V_i^{\text{min}}$  for each  $r_s$ .

$= 10V_0$  are shown on this figure in order to make possible quantitative statements as to the core radii for which  $V_i$  is "large". It is seen that for a given value of  $V_i$ , large core radii are associated with shorter ranges for the attractive force, as would be expected.

The most interesting feature of the results is the very slight variation with  $r_c$  of the function  $V_0 \exp(r_c/r_s)$ , illustrated in Fig. 4. Since  $V = -[V_0 \exp(r_c/r_s)] \exp(-r/r_s)$ , this result shows that, for a given value of  $r_s$ , the

potential outside the core is nearly independent of the core radius. More exactly, curves are drawn in Fig. 4 showing the values of core radius for which the potential varies by more than one per cent and five per cent from its value for small core radii. Thus for  $r_s = 0.52 \times 10^{-13}$  cm., the potential is

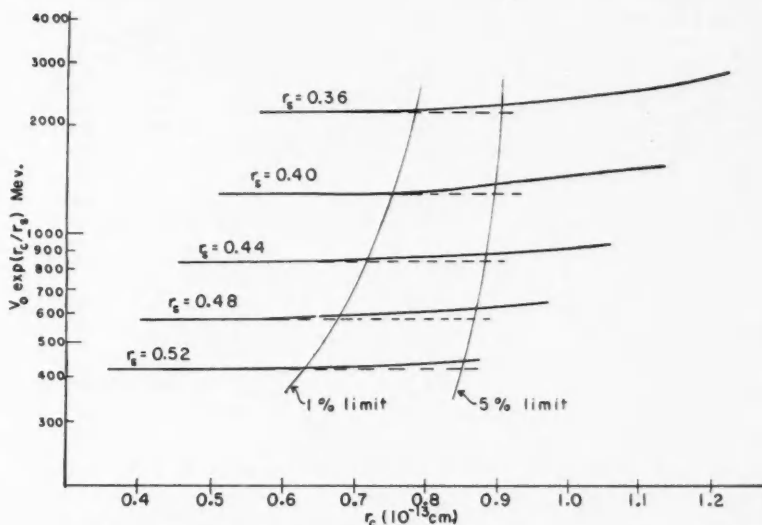


FIG. 4. The quantity  $V_0 \exp(r_c/r_s)$ , which determines the attractive potential, as a function of  $r_s$  for several values of  $r_s$ . The values of  $r_c$  for which the ordinate exceeds its minimum value by 1% and 5% are joined by the lines so labelled.

constant to 1% for all  $r_c < 0.63 \times 10^{-13}$  cm., while for  $r_s = 0.36 \times 10^{-13}$  cm. the corresponding figure is  $r_c < 0.79 \times 10^{-13}$  cm. Similarly the potential is constant to within 5% for all core radii less than  $0.85 \times 10^{-13}$  cm., irrespective of the value of  $r_s$ . The same limits are shown on Fig. 3. For all values of repulsive potential greater than 700 Mev. the attractive potential is constant to less than one per cent for a given  $r_s$ . For the higher values of  $r_s$  (around  $0.52 \times 10^{-13}$  cm.), this minimum value of  $V_i$  falls from 700 Mev. to 500 Mev. The five per cent limit on  $V_i$  depends more strongly on  $r_s$ ; for  $r_s = 0.52 \times 10^{-13}$  cm., the attractive potential is constant to five per cent for all  $V_i > 70$  Mev.; for  $r_s = 0.36 \times 10^{-13}$  cm., the corresponding figure is 260 Mev.

Consequently, for a given  $r_s$ , there is a set of potentials, defined by a lower limit on  $V_i$ , say  $V_i^{\min}$ , or an upper limit on  $r_c$ , which are "equivalent" in that they give essentially the same scattering length, effective range, and phase shift at 40 Mev. and have the same attractive potential at each value of  $r$  outside the core. It is only when  $V_i < V_i^{\min}$  that the reduction in the strength of the core affects the attractive potential. Hence it seems reasonable that for energies up to about 40 Mev. most properties of the neutron-proton system

will be independent of the value of  $V_i$ , provided it exceeds  $V_i^{\text{min}}$ . There is no reason to suppose that this behavior is connected in any essential way with the use of an exponential potential. Thus we have quantitative confirmation of the fact that for low energy states calculations with infinite repulsive cores will give results in close agreement with those for any reasonably strong repulsion. The core radius is, of course, different in the two cases.

## REFERENCES

1. BETHE, H. A. Phys. Rev. 76: 38. 1949.
2. BLATT, J. M. and JACKSON, J. D. Phys. Rev. 76: 18. 1949.
3. CHRISTIAN, R. S. and HART, E. W. Phys. Rev. 77: 441. 1950.
4. CHRISTIAN, R. S. and NOYES, H. P. Phys. Rev. 79: 85. 1950.
5. JACKSON, J. D. and BLATT, J. M. Revs. Mod. Phys. 22: 77. 1950.
6. JASTROW, R. Phys. Rev. 81: 165. 1951.
7. KLEIN, A. Phys. Rev. 89: 1158. 1953.
8. LÉVY, M. M. Phys. Rev. 88: 725. 1952.
9. PRESTON, M. A. and SHAPIRO, J. Phys. Rev. 96: 813. 1954.



# DIFFRACTION OF MICROWAVES BY LONG METAL CYLINDERS<sup>1</sup>

BY ALBERT W. ADEY<sup>2</sup>

## ABSTRACT

A parallel-plate transmission line has been applied to the study of the amplitude and phase of the diffracted electric field near metal cylinders of circular, square, and rectangular cross-section. The transverse dimensions of the cylinders are comparable with the wavelength (3.280 cm.). A travelling dipole probe inserted in the line through a slot in one of the plates permits investigation of the field. Absorbing wedges at the boundary of the line make the plates effectively infinite in extent. Essentially plane wave conditions exist in the region utilized in the measurements. Good agreement is obtained between calculation and experiment for circular cylinders. Measured results are given for square and rectangular cylinders. For one orientation of the rectangles the measured results are compared with approximate calculations.

## INTRODUCTION

Although much theoretical work has been done on diffraction by cylindrical obstacles (8, 10, 11, 14, 16, 18, 19, 22), comparatively little experimental work has been attempted (1, 3, 7, 9, 18, 23), because of the difficulties inherent in the free-space method, which was, until recently, the only one available. When this study was initiated, the only previous attempt, known to the author, made to compare theory with experiment for the near field of a dielectric cylinder, under reasonably equivalent conditions of calculation and measurement, was that of Schaefer and Grossman (18) and Kobayashi-Iwao (8). They used damped waves and cylinders small with respect to the wavelength. Also the measurements had been confined to cylinders of circular cross-section. A recent paper (4) gives some calculated and measured results for circular cylinders of radius comparable with the wavelength (3 cm.).

As a first attempt toward improvement over the free-space method, Kodis (9) used a single image plane. Then independently, at Imperial College by El-Kharadly (2), and at Harvard University by Row (17), the parallel-plate transmission line technique was developed to treat essentially two-dimensional problems. A 10 cm. line, similar in design to that of Row, is at present being developed at the Radio Physics Laboratory.

In the following there is described a 3 cm. line based on the general design used by El-Kharadly (2) and Primich (15). Calculated and experimental results are given for diffraction by circular cylinders of metal as a standard problem to assess the usefulness of the equipment, which is then applied to the study of the diffraction by metal cylinders of square and rectangular cross-section.

The following tables were used in the calculations:

<sup>1</sup>Manuscript received March 22, 1955.

Contribution from the Department of Electrical Engineering, Imperial College of Science and Technology, London, S.W.7, England.

The material of this paper formed part of a Thesis accepted by the University of London for the Ph.D. degree in Electrical Engineering, October 1954.

<sup>2</sup>Present address: Radio Physics Laboratory, Defence Research Board, Ottawa, Canada.

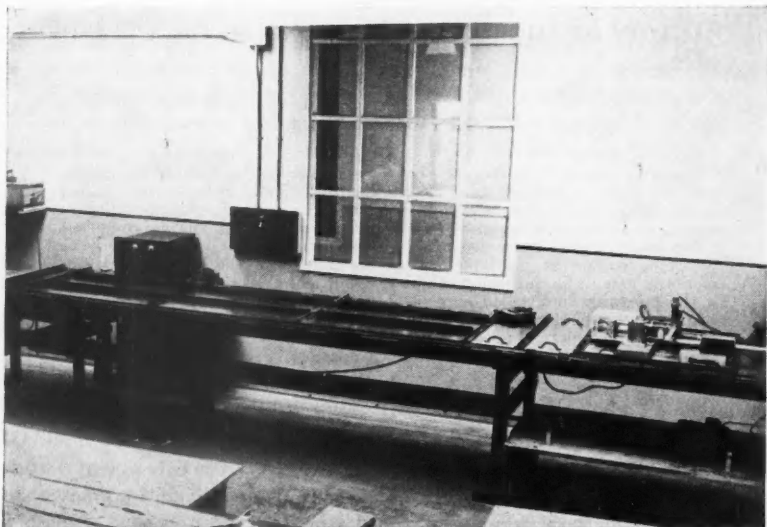


FIG. 1. General view of the parallel-plate equipment.

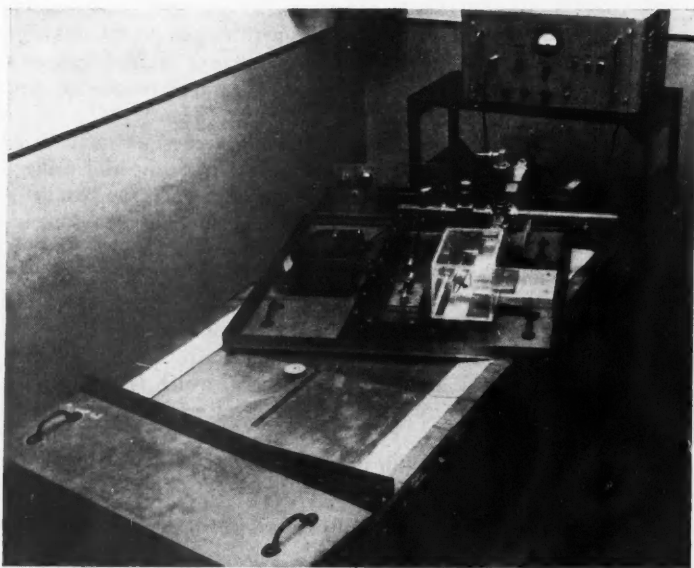


FIG. 2. View of the measuring end of the equipment, with the hinged and detector plates removed to show arrangement of the wedges, the obstacle mount, and the section angles.

(1) Bessel Functions. British Association Mathematical Tables. Vol. VI (1937) and Vol. X (1952). Cambridge University Press.

(2) Fresnel Integrals. Tables of the Scientific Computing Service, London, England.

### EQUIPMENT

The general features of the 3 cm. line are shown in Figs. 1, 2, and 3. The system involved confining the main lobe of a 24 in., H-plane, sectoral horn between two conducting plates separated by 0.480 in. The plates were spaced, and the line terminated, by wooden wedges. The side wedges were of oak, flat for 1½ in. and tapered for 4 in. and with a voltage standing wave ratio less than 1.03. The end wedge was of teak, flat for 2 in. and tapered for 5 in. and with a voltage standing wave ratio of 1.02. The wedges were coated with Aquadag on all surfaces except the tapered one.

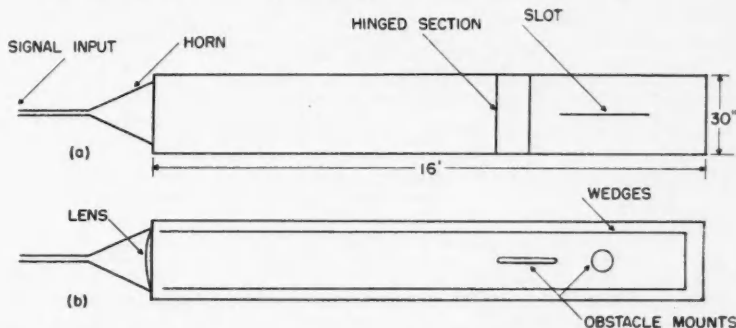


Fig. 3. Top view of the parallel-plate region and the feed system. (a) Top plate on. (b) Top plate removed.

Since the plate spacing was less than a half-wavelength, the only possible propagating component of the electric field was that normal to the plates.

A plano-convex lens of polystyrene was used in the horn aperture for phase correction of the aperture distribution.

In order to provide a fairly smooth axial distribution of the electric field, the line was made sufficiently long that the aperture covered less than one Fresnel Zone in the measuring region (about 120 degrees).

The plates consisted mainly of  $\frac{3}{8}$  in. bakelite sections, each covered on the inner surface with a 0.001 in. layer of tin foil to simulate a conducting surface, and they were provided with drilled angles for fastening them together. The plates in the measuring region were of either  $\frac{1}{4}$  or  $\frac{3}{8}$  in. brass (Fig. 3). A hinged plate provided access to the line interior for removing and inserting obstacles. This is shown unfastened in Fig. 2. The cylinder could also be inserted through a trap door in the bottom plate of the detector section. This section was of  $\frac{3}{8}$  in. brass, 30 in. square, and was provided with a 1/16 in. by 21 in. slot in the top plate for a 0.007 in. travelling probe. The top plate could be oriented with the slot either along the line axis or normal to it, for

the measurement of either the transverse or the axial distribution of the electric field.

The transverse distribution of the field was not plane, but the departure was negligible in the region occupied by the cylinders. Because of the wave-guide type of mode in the line, the measured wavelength was slightly longer than for free space—3.280 cm. compared with 3.275 cm.

The schematic layout is given in Fig. 4. The CV-129 reflex klystron was driven from a stabilized power unit, with square wave modulation at 2500 c.p.s. Frequency and amplitude monitoring facilities were provided.

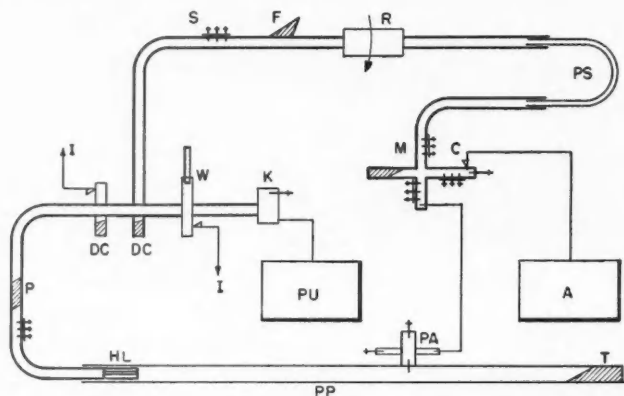


FIG. 4. Schematic layout of the parallel-plate region and associated equipment.

- |                              |                           |
|------------------------------|---------------------------|
| A—Selective audio-amplifier. | PA—Probe assembly.        |
| C—Crystal rectifier.         | PP—Parallel-plate region. |
| DC—Directional coupler.      | PS—Phase shifter.         |
| F—Flap attenuator.           | PU—Power unit.            |
| HL—Horn and lens.            | R—Rotary attenuator.      |
| I—To indicator.              | S—Tuning screws.          |
| K—CV-129 klystron.           | T—Line termination.       |
| M—Magic T.                   | W—Wavemeter.              |
| P—Padding attenuator.        |                           |

Phase was measured by the standard bridge method, with independent control of the amplitude and the phase of the reference signal being possible through the use of (a) a constant-phase rotary attenuator (5) (Elliott Model No. B 204) and (b) a trombone phase shifter based on the telescoping of the two sizes of X-band wave guide— $\frac{1}{2}$  and 1 in. I.D. and O.D. respectively. For amplitude measurements the coaxial line carrying the probe signal to the magic T could be disconnected at the probe carriage and the signal taken off through an inserted crystal rectifier. The bridge arms were equalized to minimize phase drift due to frequency changes.

The procedure was to measure the amplitude and phase along the slot, first for an empty line and then with the cylinder inserted, following which the point-by-point amplitude ratio and phase shift due to the cylinder were calculated.

The initial results for circular metal cylinders are described in the next

section. They indicated a measuring accuracy within  $3^\circ$  for phase and 3% for amplitude.

#### DIFFRACTION BY AN INFINITELY-LONG CIRCULAR METAL CYLINDER A. Problem

This problem has become a form of standard for checking diffraction equipment. It can be formulated with reference to Fig. 5.



FIG. 5. Coordinate system for plane-wave scattering by a cylinder.

The plane wave that is incident on the cylinder has its electric vector polarized parallel to the cylinder axis and is propagating in the direction  $\phi = 0$  in a medium that can be considered as free space. The problem is thus a scalar one. Rationalized m.k.s. units are used throughout and the time factor  $e^{-i\omega t}$  is omitted.

If the incident amplitude is taken as unity, for convenience, the electric field is given by

$$[1] \quad E_{inc}(r, \phi) = e^{ikr \cos \phi}$$

where  $k = 2\pi/\text{wavelength}$ . The absence of any detectable falling-off in the electric field amplitude along the slot in the measuring region validated this "plane wave" assumption. Equation [1] can be expanded as

$$[2] \quad E_{inc}(r, \phi) = \sum_0^{\infty} \epsilon_n (i)^n J_n(kr) \cos n\phi$$

where  $\epsilon_0 = 1$ ;  $\epsilon_n = 2$ ,  $n = 1, 2, \dots$ ; and the  $J_n(kr)$  are the Bessel functions of the first kind.

The scattered field is assumed of the form

$$[3] \quad E_{sc}(r, \phi) = \sum_0^{\infty} \epsilon_n B_n H_n^{(1)}(kr) \cos n\phi$$

where

$$[4] \quad H_n^{(1)}(kr) = J_n(kr) + iY_n(kr)$$

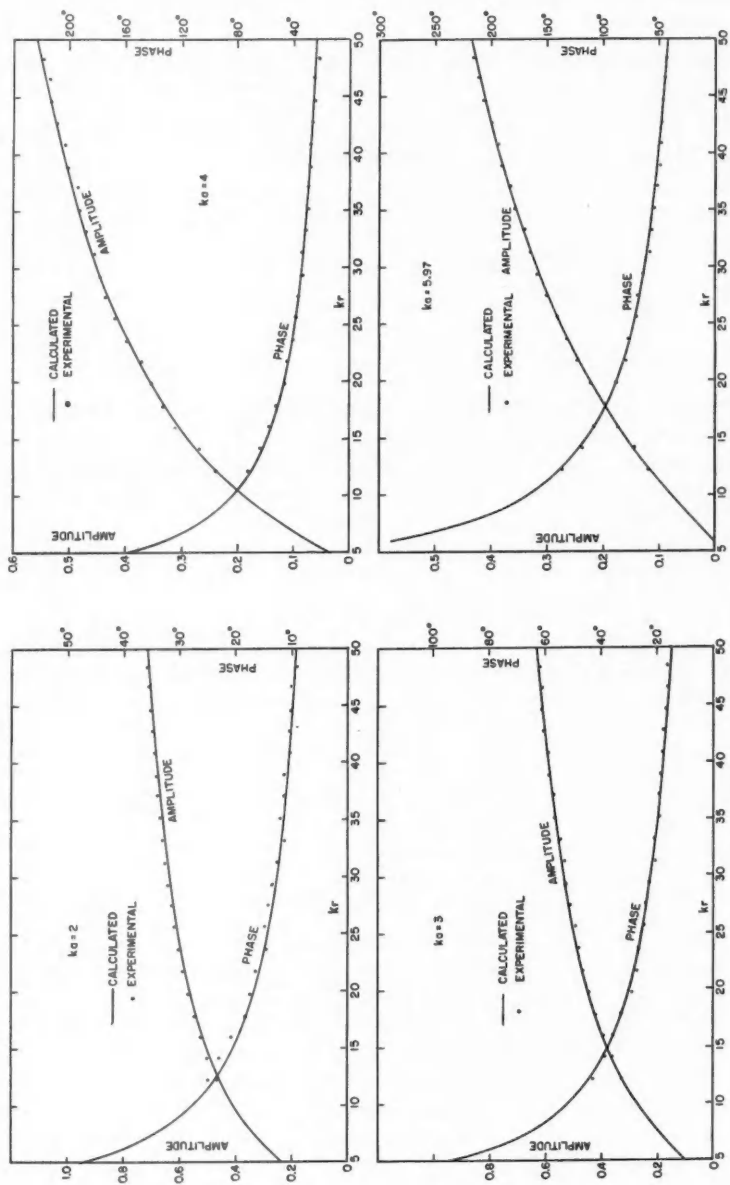
are the Hankel functions of the first kind and the  $B_n$  are to be determined from the boundary condition. This requires that

$$[5] \quad E_{total}(a, \phi) = E_{inc}(a, \phi) + E_{sc}(a, \phi) = 0$$

from which, through use of equations [2] and [3],

$$[6] \quad B_n = -(i)^n J_n(ka) / H_n^{(1)}(ka).$$

The scattered field is thus specified by equations [3] and [6]. The total field is found by adding the scattered field to the incident field given by equation [1].

FIG. 6. Shadow electric field of a conducting cylinder ( $\phi = 0$ ).

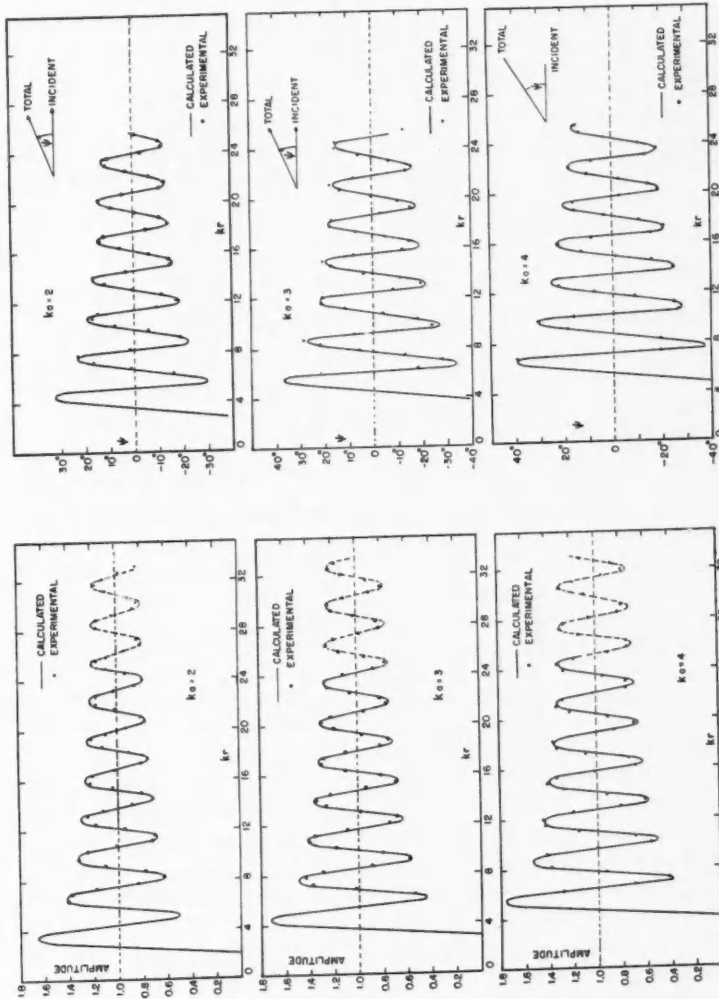


FIG. 7. Amplitude of electric field on illuminated side of a conducting cylinder ( $\phi = \pi$ ).

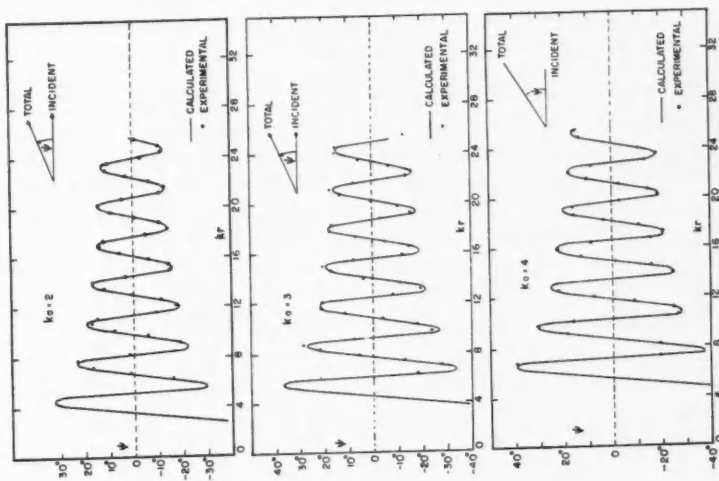


FIG. 8. Phase of electric field on illuminated side of a conducting cylinder ( $\phi = \pi$ ).

### B. Total Field

Some of the results obtained for forward scattering ( $\phi = 0$ ) and back scattering ( $\phi = \pi$ ) are given in Figs. 6, 7, and 8. They illustrate the deep shadow effect behind a metal cylinder and the typical standing wave in front. No standing wave appears in the shadow, where the incident and scattered waves travel in the same direction with comparable phase constants.

### C. Diffraction by Metal Cylinders of Square and Rectangular Cross-section

The only results that appear to be available for scattering by a cylindrical obstacle of square or rectangular cross-section are the theoretical ones by Jones (6) for diffraction of a plane wave by a thick metal plate of finite length. These do not strictly apply, however, to the interesting case where the dimensions of the obstacle are of the order of a wavelength.

It was decided, therefore, to apply the parallel plate technique to the experimental study of the shadow field of the following cases:

(a) Metal squares for incidence along a normal and along a diagonal.

(b) Metal rectangles for incidence along a normal to each of the two dimensions. For the case of one of the orientations a very rough approximation regarding the surface current distribution was used to make calculations for comparison with the experimental results.

#### Case I. Metal Squares

The measurements were made on a family of seven metal squares in the  $ka$  range 1.45–5.07, where " $a$ " is the half-side. The results were first plotted in detail for each value of  $ka$ , and then a cross-section taken through the family of curves for several values of  $kr$ .

Fig. 9 gives the results for normal incidence and Fig. 10 for diagonal incidence. The behavior with respect to  $ka$  is similar to that for the circular metal cylinders—a deepening of the shadow and an increase in phase as the dimension is increased, and an increase in amplitude and decrease in phase as the distance from the obstacle is increased.

An additional feature of the square cylinder case, however, due probably to interaction between the front and back faces, is the tendency for the curves to flatten for  $ka$  values between 3 and 4. A plot of the results was made in the complex plane. This plot, not given here, showed that, for diagonal incidence, a sharp bend occurred in the curves for  $ka$  values of 1.6 and 3.3 which correspond to sides of approximately one half and one wavelength respectively. The bends became more pronounced with increasing  $kr$ . For normal incidence one bend occurred, for  $ka$  between 2.3 and 3.4, corresponding to a side of the order of a wavelength. It, too, was more pronounced for increasing  $kr$ .

On comparing the curves, Figs. 9 and 10, for square cylinders with the corresponding ones (not shown) for circular cylinders the following points are observed:

(a) The circular cylinder curves are smooth functions of  $ka$ , while those for the square cylinder are oscillating functions of the half-side.



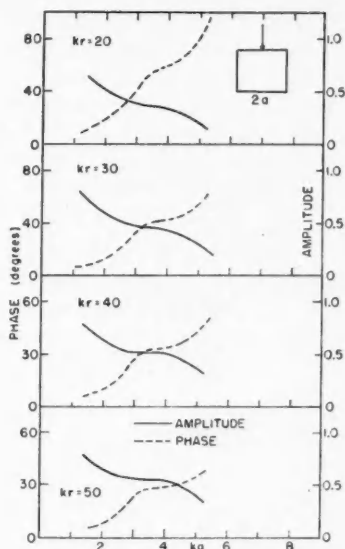


FIG. 9. Shadow electric field of metal squares. Normal incidence.

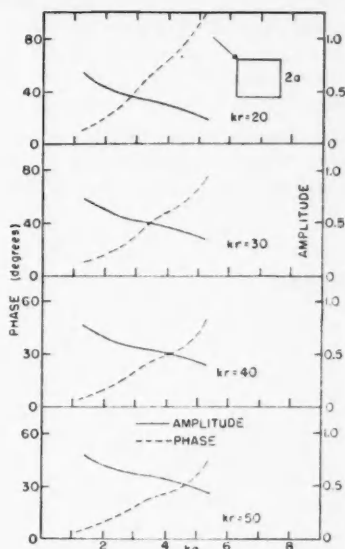


FIG. 10. Shadow electric field of metal squares. Diagonal incidence.

(b) The square cylinder amplitude curves oscillate about smooth curves below those for the circular cylinder. For diagonal incidence the oscillations occur about a curve corresponding to a circular cylinder for which the ratio radius/half-side = 1.06. For normal incidence the ratio is 1.12.

(c) The square cylinder phase curves oscillate about smooth curves above those for the circular cylinder. The ratios corresponding to those of (b) are 1.27 and 1.15 respectively.

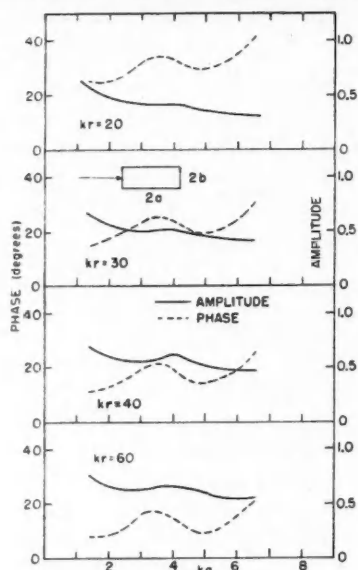
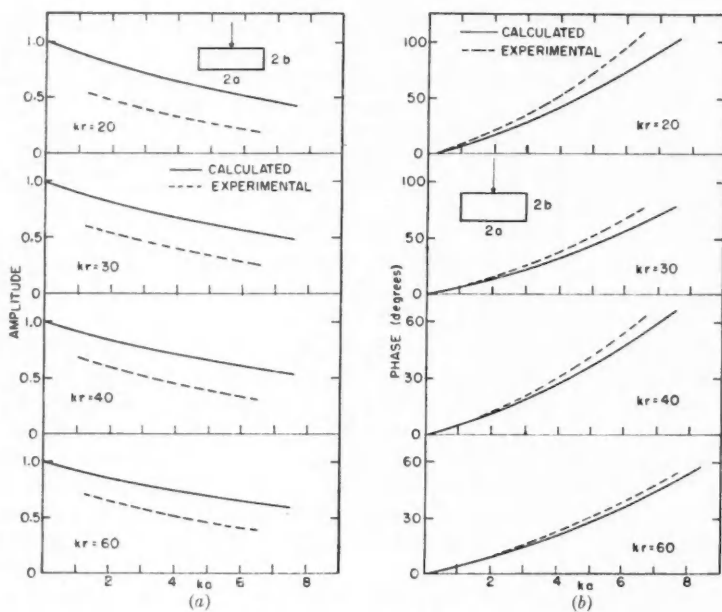
The product of the ratios for normal incidence, i.e.,  $1.06 \times 1.27$ , thus tends to be the same as that for diagonal incidence, i.e.,  $1.12 \times 1.15$ . For a particular value of  $ka$  both the amplitude and phase are less for normal incidence than for diagonal incidence.

#### Case II. Metal Rectangles

The first measurements were made, for two orientations, on a family of 11 rectangles of dimensions  $2a \times 2b$  with  $kb = 2.41$  and  $ka$  in the range 1.63–6.42.

The results for the orientation in which the dimension along the direction of incidence was varied are given in Fig. 11. As for the metal squares, the effect of interaction between the front and back faces is apparent, with a sharp bend appearing in the diagrams in the complex plane (not shown here) for  $ka$  in the region 3.0–4.0.

For the other orientation the effect of leaving constant the dimension in the direction of incidence is shown by the absence of fluctuations (Fig. 12).

FIG. 11. Shadow electric field of metal rectangles of  $kb = 2.41$ .FIG. 12. Shadow electric field of metal rectangles of  $kb = 2.41$ . (a) Amplitude. (b) Phase.

The calculations for the latter orientation were based on the approximation that the obstacle is replaced by a current sheet of horizontal width  $2a$  in the plane occupied by the front face, with the current density the same as though the obstacle were infinite in extent in the direction normal to the direction of incidence and of the electric field vector. The approximation corresponds to that used by O'Neil (13) and Muller (12) in studies of the acoustic pressure on and near metal obstacles. In the present case the assumed induced current density is given by

$$[7] \quad J = 2H_{\text{tang}} = 2H_{\text{inc}}.$$

The scattered field resulting from this current distribution is determined with reference to Fig. 13.

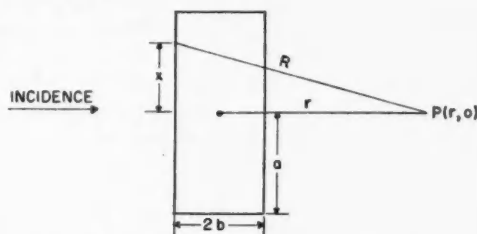


FIG. 13. Coordinate system for plane wave scattering by a rectangle.

Since the incident field is given by

$$[8a] \quad E_{\text{inc}}(r, 0) = e^{ikr},$$

$$[8b] \quad H_{\text{inc}}(r, 0) = \frac{k}{\omega\mu} e^{ikr},$$

then, from equation [7],

$$[9] \quad J = \frac{2k}{\omega\mu} e^{-ikb}.$$

The total scattered field then becomes (20)

$$[10] \quad E_{\text{sc}}(r, 0) = -\frac{k}{2} \int_{-a}^a H_0^{(1)}(kR) e^{-ikb} dx$$

which transforms, for large  $kR$ , to

$$[11] \quad E_{\text{sc}} \sim -\sqrt{2} e^{i(kr - \pi/4)} [C(t) + iS(t)]$$

where

$$[12] \quad C(x) + iS(x) = \int_0^x e^{it^2} t^{1/2} dt,$$

$$[13] \quad t = ka \left[ \frac{1}{\pi k(r+b)} \right]^{1/2}.$$

Addition of equations [11] and [8a] gives the total field, plotted in Fig. 12.

While the general form of the curves is in agreement with the experimental,

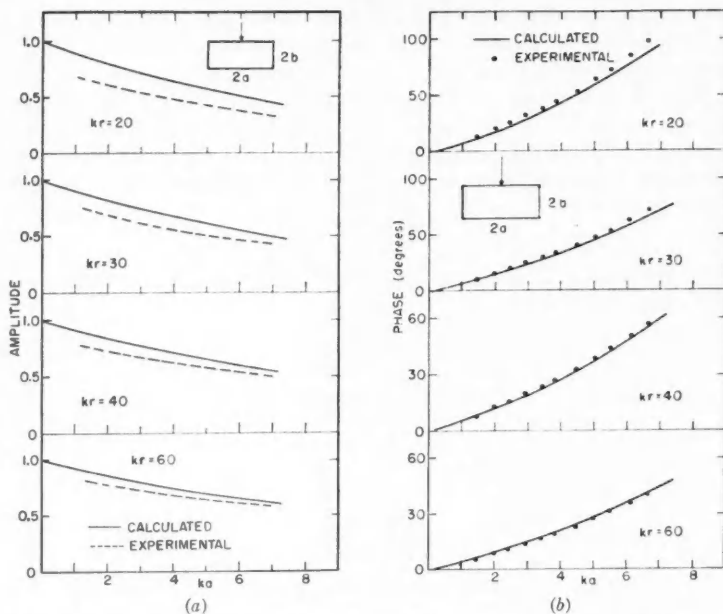


FIG. 14. Shadow electric field of metal rectangles of  $kb = 1.20$ . (a) Amplitude. (b) Phase.

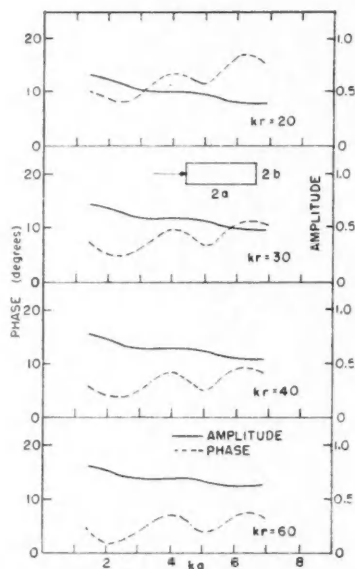


FIG. 15. Shadow electric field of metal rectangles of  $kb = 1.20$ .

the quantitative agreement is poor, particularly for the amplitude, although there is improvement with increasing  $kr$ .

In order to assess the effect of the ends of the obstacles on the experimental results, the measurements and calculations were repeated for a reduced value of  $kb = 1.20$  for 11 obstacles in the  $ka$  range 1.44–6.66. The results are given in Fig. 14 and show better agreement, particularly for the larger  $ka$  and  $kr$ . This might be anticipated from the nature of the assumptions made in deriving equation [11].

The experimental results for the other orientation are given in Fig. 15, with the form of the curves being as for Fig. 11. There was obviously little use in making the calculations for this orientation, or for the metal squares.

#### D. Conclusions

The parallel-plate equipment has been shown to provide a very useful tool for diffraction measurements on cylindrical obstacles at microwave frequencies. The main features of the technique, compared with free-space methods, are improved measuring accuracy, a more systematic measuring program, and economy of space and materials. The method can provide reliable scattering information about obstacle forms for which no exact theoretical solutions are available.

The results obtained for dielectric cylinders of the three cross-section forms will be presented in another paper.

#### ACKNOWLEDGMENTS

The guidance and advice of Dr. Willis Jackson and Mr. J. Brown of Imperial College of Science and Technology are gratefully acknowledged. Thanks are extended to the University of New Brunswick for the award of a Beaverbrook Overseas Scholarship and to the Canadian Defence Research Board for a subsequent study grant. The advice of Dr. J. R. Wait and Mr. P. A. Field in the preparation of the paper is acknowledged.

#### REFERENCES

1. BESUSZKA, S. J. *J. Acoust. Soc. Amer.* 25: 1090. 1953.
2. EL-KHARADLY, M. Z. Ph.D. Thesis, University of London. 1953.
3. FARAN, J. J. *J. Acoust. Soc. Amer.* 23: 405. 1951.
4. FROESE, C. and WAIT, J. R. *Can. J. Phys.* 32: 775. 1954.
5. HAND, B. P. *Electronics*, 27: 184. 1954.
6. JONES, D. S. *Proc. Roy. Soc. (London)*, A, 217: 153. 1953.
7. KEYS, J. M.Sc. Thesis, McMaster University, Hamilton, Ontario. 1953.
8. KOBAYASHI-IWAO. *Ann. phys.* 43: 861. 1914.
9. KODIS, R. *J. Appl. Phys.* 23: 249. 1952.
10. LAX, M. and FESHBACH, H. *J. Acoust. Soc. Amer.* 20: 108. 1948.
11. MULLIN, E. B. *Radio aerials*. The Clarendon Press, Oxford. 1949.
12. MULLER, G. G. *et al.* *J. Acoust. Soc. Amer.* 10: 6. 1938.
13. O'NEIL, H. T. and SIVIAN, L. J. *J. Acoust. Soc. Amer.* 3: 483. 1932.
14. PAPAS, C. H. *J. Appl. Phys.* 21: 318. 1950.
15. PRIMICH, R. I. Ph.D. Thesis, University of London. 1954.
16. RAYLEIGH, LORD. (a) *Phil. Mag.* 12: 81. 1881. (b) *Phil. Mag.* 36: 365. 1918.
17. ROW, R. V. *J. Appl. Phys.* 24: 1448. 1953.
18. SCHAEFER, C. L. and GROSSMAN, F. *Ann. phys.* 31: 455. 1910.
19. SEITZ, W. (a) *Ann. phys.* 16: 746. 1905. (b) *Ann. phys.* 19: 554. 1906.
20. STRATTON, J. A. *Electromagnetic theory*. McGraw-Hill Book Company, Inc., New York. 1941. p. 595.
21. TAMARKIN, P. (a) *J. Acoust. Soc. Amer.* 20: 858. 1948. (b) *J. Acoust. Soc. Amer.* 21: 612. 1949.
22. THILO, G. *Ann. phys.* 62: 531. 1920.
23. WILES, S. T. and McLAY, A. B. *Can. J. Phys.* 32: 372. 1954.

# THE VISCOSITY OF LIQUID HELIUM II<sup>1</sup>

BY W. J. HEIKKILÄ<sup>2</sup> AND A. C. HOLLIS HALLETT

## ABSTRACT

It has been found possible to use the rotating cylinder viscometer to measure the viscosity of liquid helium II between 1.13°K. and 2.18°K. provided that the fluid velocities do not exceed about 0.08 cm. sec.<sup>-1</sup>. The results, which are calculated directly from experimental observations and do not require any knowledge of the density of the normal component, can be made to fit the Landau and Khalatnikov theory for the temperatures below 1.8°K. for which the theory is applicable. The results are somewhat higher than the oscillating disk results above 1.4°K.

## 1. INTRODUCTION

The rotating cylinder viscometer has been used earlier by one of us (7) to study the frictional forces exerted by rotating liquid helium II on a solid cylindrical boundary. The results of these previous experiments indicated the existence of non-linear frictional forces in the liquid, and in the velocity range used (0.1 to 3 cm. sec.<sup>-1</sup>) these forces were considerably larger than the purely viscous forces associated with laminar flow of the normal component of liquid helium II. Estimates of the coefficient of viscosity could only be made by extrapolation of the experimental results to zero velocity.

The same apparatus has been used again with much smaller velocities of rotation of the fluid (0.01 to 0.16 cm. sec.<sup>-1</sup>). At these smaller velocities, it has been found possible to deduce values of the coefficient of viscosity directly with an experimental error of the order of 3%. The viscosity can be calculated directly from the experimental observations without the use of data for the density of the normal component which is so necessary in the reduction of the results of the oscillating disk experiment. The variation with temperature of the values of the viscosity deduced is shown to be in good agreement with the theory due to Landau and Khalatnikov (11) in the low temperature range for which the theory is applicable. There are, however, real discrepancies when the present results are compared with the oscillating disk results, particularly near the lambda-point, and the significance of these discrepancies is discussed.

## 2. THE APPARATUS

The viscometer is illustrated schematically in Fig. 1. Liquid helium was contained in the annular space between two coaxial cylinders *A* and *B* and could be set in steady rotation by the rotation of the outer cylinder *B* at various constant speeds. The viscous couple exerted by the rotating fluid on the inner cylinder *A* twisted this inner cylinder against a restoring couple provided by a torsion suspension fiber kept at room temperature above the

<sup>1</sup>Manuscript received March 29, 1955.

Contribution from the Department of Physics, University of Toronto, Toronto 5, Ontario, Canada.

<sup>2</sup>Present address: Defence Research Telecommunications Establishment, Radio Physics Laboratory, Ottawa, Ontario, Canada.

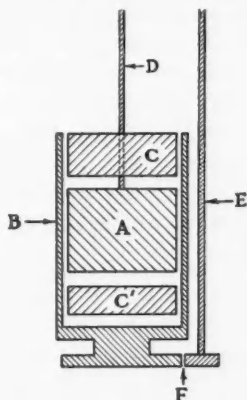


FIG. 1. Schematic diagram of the viscometer.

cryostat and connected to *A* by means of the long straight quartz rod *D*. *E* represents the driving shaft for the outer cylinder, which was connected to a Selsyn motor outside the cryostat. It transmitted the driving torque to the outer cylinder *B* by means of the gear train *F*. *C* and *C'* represent two guard cylinders, coaxial with *A* and *B*, which were provided to eliminate end effects. Full details of the construction of the viscometer may be found in the previous paper (7).

Equating the viscous couple exerted by the rotating fluid on the inner cylinder to the restoring couple,  $K\phi$ , of the suspension, it follows (13) that

$$[1] \quad \eta \frac{4\pi Rr^2h}{(R^2 - r^2)} v = K\phi,$$

where  $R$  = the radius of the outer cylinder,

$v$  = the peripheral velocity of the outer cylinder,

$r$  = the radius of the inner cylinder,

$h$  = the height of the inner cylinder,

$K$  = the torsion constant of the suspension,

$\phi$  = the angular deflection of the inner cylinder,

and  $\eta$  = the coefficient of viscosity of the fluid.

The velocity  $v$  can be determined from the time  $t$  of one complete rotation of the outer cylinder with the aid of the simple relation  $v = 2\pi R/t$ . The torsion constant  $K$  can be determined from the period  $T$  of free oscillations of the inner cylinder using the relation  $K = 4\pi^2 I/T^2$  where  $I$  is the moment of inertia of the inner cylinder.

In principle, therefore, the viscosity can be calculated directly from the observed deflection,  $\phi$ , of the inner cylinder produced by the rotation of the outer cylinder at a known constant velocity  $v$ , if the dimensions of the apparatus and the torsion constant of the suspension are known.

Measurements of the dimensions of the apparatus have not led to any changes in the values previously published (7):

$$R = 2.0970 \pm 0.0006 \text{ cm.},$$

$$r = 1.9913 \pm 0.0001 \text{ cm.},$$

$$h = 2.990 \pm 0.005 \text{ cm.}$$

A redetermination of the moment of inertia of the inner cylinder has, however, given a slightly higher value with a smaller probable error:

$$I = 46.55 \pm 0.05 \text{ gm. cm.}^2$$

Since the velocity range to be covered was to be  $10^{-2}$  to  $10^{-1}$  cm./sec., it was necessary to find suspension fibers which would have a sufficiently small torsion constant to give adequate sensitivity, and yet be strong enough to support the 20 gm. weight of the inner cylinder. Quartz fibers were first tried, but although their theoretical breaking stress was sufficiently large, they all fractured soon after installation. Consequently tungsten was tried as an alternative, and a wire of about  $15 \mu$  diameter and about 20 cm. long was found to be successful. Initially it had a large zero drift, but the inner cylinder was left suspended by the tungsten wire for two months; after this time the zero drift had decreased to a value less than  $2 \times 10^{-4}$  radians per hour. This wire was then used to obtain the bulk of the results given below. The torsion constant of this suspension was  $3.24 \times 10^{-2}$  dyne-cm. per radian deflection.

Just below the suspension, a small mirror was attached to the quartz rod *D*. This received a beam of light from a lamp and reflected it through a lens on to a fixed scale 1 meter away. Measurements of the deflection of the inner cylinder were then made by observation of the spot of light on the scale. Close to the mirror was attached a small slightly magnetized steel screw situated in the center of a pair of Helmholtz coils in which a magnetic field could be produced by closing a switch. By switching a current into the coils in the correct direction, the rotation of the steel screw, and consequently of the inner cylinder, could be checked as desired. With the current off, the damping of the system returned to that governed by the fluid surrounding the inner cylinder.

The driving system for the outer cylinder consisted of a synchronous motor connected through a continuously variable torque converter and a gear train to a Selsyn generator. This equipment was mounted some distance from the cryostat and connected to the Selsyn motor by long flexible wires. The shaft of the Selsyn motor carried a worm gear which engaged a pinion on the upper end of the drive shaft *E* of Fig. 1.

The use of a suspension of such a small torsion constant necessitated considerable precautions to ensure that the apparatus was not influenced by vibrations. To this end, the cryostat was mounted on a solid two-ton concrete pillar which rested on the floor of the laboratory. The cryostat was isolated as far as possible from the laboratory pumping line by means of flexible metal bellows. The Selsyn motor was mounted on a separate and independent support bolted to the wall, and it was connected to the cryostat only through



the worm gear which engaged the upper end of the driving shaft *E* of Fig. 1. Such precautions were effective in reducing vibration so that it did not seriously affect the experiment.

### 3. EXPERIMENTAL DETAILS

The determination of the viscosity of liquid helium with this apparatus involves the use of equation [1], determining experimentally the angular deflection  $\phi$  of the inner cylinder which is produced by the rotation of the outer cylinder with peripheral velocity  $v$  cm./sec.

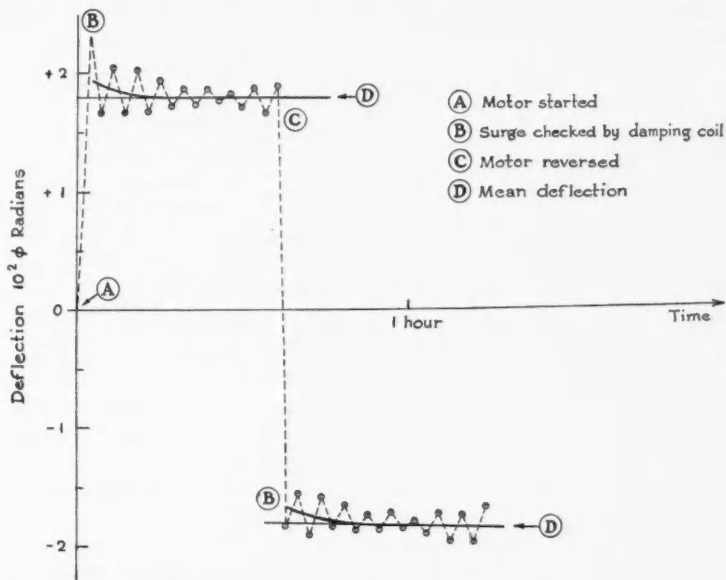


FIG. 2. The oscillations of the inner cylinder about the deflected positions corresponding to the rotation of the outer cylinder with a velocity of  $0.0614 \text{ cm. sec.}^{-1}$  at  $1.82^\circ\text{K}$ .

When rotation of the outer cylinder was started, the inner cylinder did not immediately take up a steady undisturbed deflected position at which the restoring couple of the suspension balanced the impressed viscous torque, but first overshoot the deflected position and then oscillated about it. The overshooting was usually checked by applying a magnetic field in the correct direction with the Helmholtz coils, and the results of a typical experiment at about  $1.82^\circ\text{K}$ . with a velocity  $v = 0.0614 \text{ cm./sec.}$  are shown in Fig. 2. It can be seen from this figure that the inner cylinder oscillates about a deflected position which, after about three oscillations, reaches a steady value. The fact that the oscillations had a small but rather random amplitude seemed to be due to the effects of the residual vibration which was not completely damped out by the measures taken. Once the mean deflection on one side of zero was well established, the motor drive mechanism was reversed,

and a similar pattern of oscillations about the deflected position on the other side of zero was obtained. The value of the deflection produced by the rotation of the outer cylinder at one velocity was taken to be the mean of the two deflections right and left of zero.

A value of the viscosity could be obtained by direct substitution of the observed deflection  $\phi$  and velocity of rotation  $v$  into equation [1], together with the dimensions of the apparatus and the torsion constant  $K$ . Actually it had been the practice to calibrate the apparatus by measuring the deflection and velocity of rotation when the apparatus was immersed in air at room temperature since the viscosity of air (3) and its temperature variation (12) are well known. Thus equation [1] becomes

$$[2] \quad (\phi/v) = \eta \frac{4\pi Rr^2 h}{(R^2 - r^2)K},$$

whence

$$[3] \quad \eta_{\text{He}} = \frac{(\phi/v)_{\text{He}}}{(\phi/v)_{\text{air}}} \eta_{\text{air}}$$

in which  $\eta_{\text{He}}$  and  $\eta_{\text{air}}$  are respectively the viscosities of liquid helium and gaseous air, and  $(\phi/v)_{\text{He}}$  and  $(\phi/v)_{\text{air}}$  are the ratios of deflection to velocity determined in helium and in air. Such a calibration in air immediately takes into account the small observed ellipticity of the outer cylinder, and the small correction (8) to be applied to the height of the inner cylinder in order to allow for the width of the gap between this cylinder and the two fixed guards. It should, however, be mentioned that values of  $\eta$  computed directly from equation [1] never differed from the value obtained from equation [3] by more than 2%.

Throughout the experiments there was a large and variable change of zero position which was a function of temperature rather than of time. If the oscillation zero was set on the zero of the scale when the temperature was near the lambda-point, it was observed that as the temperature was lowered, the zero position shifted progressively further to one side; at the lowest temperatures the shift increased rapidly with decreasing temperature. It seemed that part of the zero shift could be explained by the slight bending of the cryostat cap produced by the difference between atmospheric pressure outside and the smaller pressure inside the cryostat cap since a similar but smaller effect was observed at room temperature when the cryostat was evacuated. The remaining part of the zero shift not explained by mechanical deformation of the apparatus was particularly puzzling because it was not completely reproducible, and fibers of different materials gave somewhat different and discordant results. The effects were not investigated fully because it was found that by performing all experiments at carefully controlled constant temperatures, the zero shift, once determined, remained constant and did not affect the experimental results.

All temperatures were obtained from the measured vapor pressure above the liquid, using the 1949 (4) vapor pressure - temperature tables.

## 4. EVALUATION OF THE SOURCES OF ERROR

*(a) Errors in the Deflection  $\phi$* 

From Fig. 2 it can be seen that the inner cylinder never attained a steady deflected position, but performed small, rather random, oscillations about it. Allowing three or four cycles of oscillations for the deflection to reach an equilibrium value, the maxima and minima of the remaining five or six oscillations were then averaged together to give a value for the deflected position  $\phi$ . From the sum of the squares of the deviations of the individual results from the mean value, the standard error was computed in the usual manner and this figure is given for each value of  $\phi$  in the following tables.

*(b) Errors in the Velocity  $v$* 

The velocity was calculated from the relation

$$v = 2\pi R/t,$$

determining experimentally the time  $t$  of one revolution of the outer cylinder. This time of rotation was measured with a stop watch checked against a standard clock. A beam of light was reflected by a mirror attached to the drive shaft  $E$  of Fig. 1, and the time interval between transits of this beam of light across a fixed line on the laboratory wall was measured. Multiplying this time by the gear-pinion ratio ( $F$ ) (which was equal to 3) gave the time of rotation of the outer cylinder. This time was measured on several occasions during an experiment and values were obtained with an error of the order of 0.1% which is negligible compared with other experimental errors.

*(c) Errors in the Calibration in Air*

The ratio  $(\phi/v)_{\text{air}}$  (equation [3]) was obtained in conjunction with each helium experiment. The values obtained over the 10 months of experimental work rarely differed from the average by more than 1%. On one isolated day, however, the value obtained was 3% higher than the average, but this was an exception.

*(d) Errors Due to Eccentricity*

The detailed description of the apparatus given by one of us (7) indicated that the motion of the inner cylinder was constrained so that if it oscillated freely at all, the error due to eccentricity of the inner cylinder with respect to the axis of the outer was at most 1%. This was checked experimentally by deliberately throwing the apparatus out of alignment as far as possible and observing the resulting change produced in the deflection corresponding to a particular time of rotation of the outer cylinder while in air at room temperature. The maximum change in the deflection which could be produced by the allowed eccentricity was 2%, but it seemed most unlikely that during an actual experiment the alignment was so poor as to cause an error greater than 1%.

*(e) Errors Due to Contraction of the Apparatus*

On cooling the apparatus to liquid helium temperatures the apparatus certainly contracted. Consequently comparison of the observed  $(\phi/v)_{\text{He}}$

ratio with the corresponding ratio in air at room temperature leads to an error affecting all the helium results by the same factor. Because no certain knowledge of the expansion coefficients of the duralumin inner cylinder and the copper-nickel outer cylinder was available, a correction for contraction has not been applied to the results. An estimate of this correction on the basis of the Debye theory of solids suggests that the application of this correction to the rotating cylinder results will raise them by about 4%, but will only raise the oscillating disk results by about 2%. So, a 2% discrepancy between the two types of experiment can be ascribed to neglect of thermal contraction, provided that the oscillating disk results are the higher.

In general, the error in the determination of  $\phi$  is less than 1% which is the same as the error due to calibration and to eccentricity. Consequently it is possible to say that the error in the viscosity values deduced is in general less than 3%.

### 5. EXPERIMENTAL RESULTS

The experimental results at 1.82°K., which are typical of the results at all other temperatures, are shown as closed circles (●) in the upper curve of Fig. 3. Here the viscosity, calculated directly from equation [3] using the observed values of the deflection  $\phi$  and the peripheral velocity  $v$  of the outer

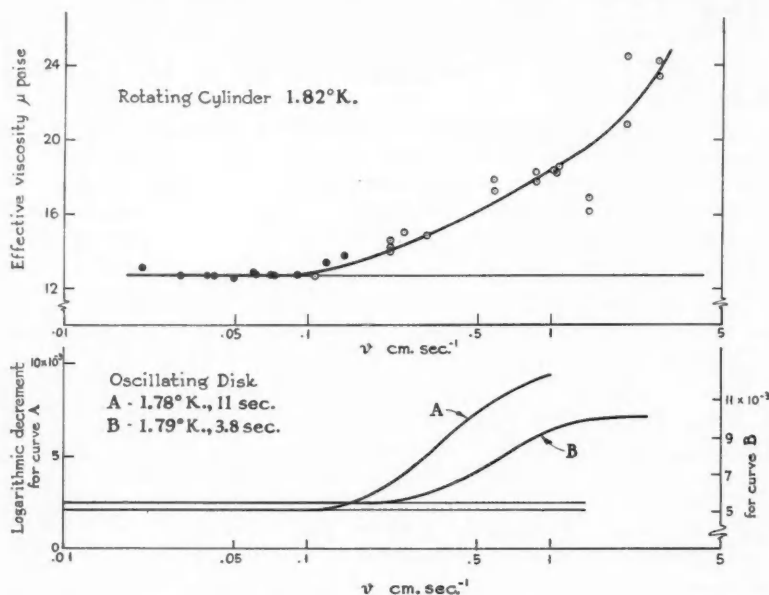


FIG. 3. Upper curve: The variation with velocity of the effective viscosity from the rotating cylinder. Lower curves: The variation of the logarithmic decrement of an oscillating disk with velocity (6).

cylinder, is plotted against the common logarithm of  $v$  in order to expand the velocity scale so that the results may be displayed clearly. The open circles ( $\circ$ ) represent higher velocity results taken from the previous paper (7). It can be seen from this figure that not only do the present results agree quite well with the earlier results, but also the curve as a whole is quite similar to the observed variation with velocity of the damping of an oscillating disk (6) which is shown for comparison in the lower curve of Fig. 3. The interpretation of the two curves appears to be the same. When the velocities are sufficiently small, the motion of the liquid is governed entirely by the properties of the normal component, particularly by its viscosity. As the velocity increases and exceeds some critical value, the motion of the fluid is governed by the action of some type of non-linear frictional force. This non-linear frictional force causes the damping of an oscillating disk to increase and exceed its constant small velocity value, and apparently the same force causes the effective viscosity calculated from the rotating cylinder observations to increase likewise and exceed its constant small velocity value. It should however be pointed out that in order to deduce values of the viscosity of the normal component of helium II from the observed small velocity constant damping of an oscillating disk, it is necessary to use data for the density of the normal component,  $\rho_n$ . Although values of  $\rho_n$  are in principle readily available from measurements of the velocity of second sound together with specific heat and entropy data, the rotating cylinder viscometer has the decided advantage that this density does not enter into the elementary theory of the viscometer at all, and values of the viscosity may be calculated directly from the observed deflection and velocity of rotation. The only condition which must be applied to the rotating cylinder results is that the deflection must be directly proportional to the velocity of rotation (equation [1]). In other words, the values of viscosity so deduced must be independent of velocity. It is therefore important to ascertain from the experimental results which values of the viscosity,  $\eta$ , are independent of velocity within experimental error and to average these together, weighting them inversely as their errors.

The results obtained are given in the accompanying Table I. The first column of the table gives the date of the experiment in order that the day-to-day reproducibility of the results can be demonstrated. The second column gives the peripheral velocity  $v$  of the outer cylinder while the observed deflection  $\phi$  corresponding to this velocity appears in column 3 together with the standard error calculated by the method described in the preceding section. The final column gives the value of the viscosity  $\eta$  calculated from equation [3], and the error indicated includes only the errors calculated for  $v$  and for  $\phi$ . Those values of  $\eta$  in the final column which, on a graph similar to Fig. 3, appear to be independent of velocity within the listed error are marked with an asterisk (\*) and the weighted mean of these values appears at the foot of each section of the table. The error quoted in these mean values merely represents the degree of consistency in the group of values for  $\eta$  from which the weighted mean was calculated. As was pointed out in the preceding section,

TABLE I  
THE VALUES OF THE EFFECTIVE VISCOSITY

Date	$\nu$ , cm. sec. <sup>-1</sup>	10 <sup>3</sup> $\phi$ , radians	$\eta$ , $\mu$ poise	Date	$\nu$ , cm. sec. <sup>-1</sup>	10 <sup>3</sup> $\phi$ , radians	$\eta$ , $\mu$ poise
(a) Temperature = 2.180°K.				(g) Temperature = 1.400°K.			
18-ii-54	.0202	1.055 $\pm$ .007	*23.15 $\pm$ 0.2	4-iii-54	.0200	0.66 $\pm$ .01	*14.6 $\pm$ 0.2
	.0404	2.11 $\pm$ .01	*23.15 0.13	2-iii-54	.0409	1.34 .015	*14.5 0.2
	.0609	3.16 .005	*23.00 0.05	23-iii-54	.0418	1.375 .045	*14.6 0.6
	.0789	4.07 .01	*22.9 0.08	4-iii-54	.0514	1.685 .01	*14.5 0.2
	.1020	5.29 .01	*23.0 0.06		.0611	1.99 .01	*14.4 0.15
	.1196	6.225 .01	*23.1 0.06	2-iii-54	.0840	3.03 .01	16.0 0.1
	.1570	8.225 .015	23.2 0.05		.1211	4.43 .01	16.2 0.1
		*Weighted average 23.04 $\pm$ 0.04				*Weighted average 14.5 $\pm$ 0.4	
(b) Temperature = 2.100°K.				(h) Temperature = 1.308°K.			
23-ii-54	.0214	0.828 $\pm$ .005	*17.2 $\pm$ 0.11	8-x-53	.0142	0.49 $\pm$ .025	*15.3 $\pm$ 0.9
	.0405	1.580 .007	*17.3 0.09		.0250	0.92 .03	*16.4 0.8
	.0594	2.36 .006	*17.6 0.09	28-xi-52	.0280	0.97 .025	*15.3 0.5
	.0811	3.19 .01	*17.4 0.14	11-xii-53	.0304	1.28 .015	*15.6 0.4
	.1017	4.06 .01	17.7 0.1	25-iii-54	.0394	1.37 .04	*15.4 0.4
	.1196	4.805 .025	17.8 0.1	22-x-53	.0483	1.66 .02	*15.3 0.4
	.1601	6.55 .03	18.1 0.1	28-xi-52	.0530	1.87 .03	*15.6 0.4
		*Weighted average 17.40 $\pm$ 0.09		18-xi-53	.0620	2.13 .015	*15.2 0.3
(c) Temperature = 2.002°K.				6-i-54	.0684	2.35 .02	*15.2 0.3
1-x-53	.0140	0.475 $\pm$ .03	*15.0 $\pm$ 1.0	8-x-53	.0734	2.565 .02	*15.5 0.3
24-ix-53	.0234	0.720 .012	*13.6 0.4	7-i-54	.0805	2.96 .02	16.2 0.4
1-x-53	.0293	0.96 .02	*14.5 0.4	18-xi-53	.0846	3.05 .025	15.9 0.3
23-vii-53	.0366	1.15 .02	*13.9 0.6	7-i-54	.0898	3.16 .03	15.6 0.3
6-x-53	.0471	1.47 .007	*13.8 0.15	22-x-53	.1030	3.87 .02	16.7 0.3
23-vii-53	.0535	1.68 .012	*13.9 0.5	22-v-53	.106	3.85 .05	16.1 0.4
6-x-53	.0616	1.97 .012	*14.2 0.2	28-xi-52	.109	4.08 .03	16.6 0.3
24-ix-53	.0718	2.24 .009	*13.9 0.15			*Weighted average 15.4 $\pm$ 0.06	
1-x-53	.0892	2.81 .025	*14.0 0.2	(i) Temperature = 1.250°K.			
6-x-53	.0996	3.325 .02	14.8 0.2	31-iii-54	.0199	0.79 $\pm$ .03	*17.6 $\pm$ 0.5
23-vii-53	.1128	3.685 .015	14.5 0.4	18-v-54	.0397	1.495 .075	*16.7 0.8
6-x-53	.1453	5.02 .015	15.3 0.15	31-iii-54	.0406	1.675 .025	*18.3 0.5
		*Weighted average 13.97 $\pm$ 0.07		11-vi-54	.0511	2.07 .05	*17.9 0.5
(d) Temperature = 1.820°K.				18-v-54	.0597	2.285 .075	*17.0 0.5
4-ii-54	.0210	0.62 $\pm$ .01	*13.1 $\pm$ 0.3	11-vi-54	.1028	4.335 .03	18.7 0.2
17-ii-54	.0301	0.857 .008	*12.65 0.18			*Weighted average 17.5 $\pm$ 0.4	
10-ii-54	.0388	1.115 .015	*12.70 0.23	(j) Temperature = 1.200°K.			
23-iii-54	.0416	1.185 .015	*12.65 0.2	2-vi-54	.0397	1.705 $\pm$ .04	*19.0 $\pm$ 0.4
17-ii-54	.0495	1.40 .006	*12.55 0.1	2-iii-54	.0402	1.775 .03	*19.5 0.4
4-ii-54	.0603	1.75 .03	*12.85 0.26	4-iii-54	.0605	2.785 .025	*20.4 0.3
17-ii-54	.0614	1.775 .005	*12.80 0.1			*Weighted average 19.6 $\pm$ 0.4	
	.0709	2.04 .01	*12.75 0.1	(k) Temperature = 1.131°K.			
	.0714	2.05 .01	*12.75 0.1	4-ii-54	.0105	0.54 $\pm$ .035	*22.9 $\pm$ 1.5
	.0927	2.665 .01	*12.75 0.1		.0206	1.02 .06	*22.0 1.0
	.1119	3.37 .01	13.35 0.1	29-x-53	.0294	1.61 .05	*24.1 1.0
	.1424	4.41 .01	13.7 0.1	19-xi-53	.0363	1.74 .06	*21.3 1.0
		*Weighted average 12.69 $\pm$ .04		30-x-53	.0371	1.45 .1	*17.3 2.0
(e) Temperature = 1.650°K.				29-x-53	.0482	2.17 .03	*19.9 0.5
1-vi-54	.0200	0.545 $\pm$ .015	*12.0 $\pm$ 0.3	19-xi-53	.0603	2.83 .05	*20.9 0.5
9-iii-54	.0211	0.635 .01	*13.3 0.2	25-xi-53	.0613	2.70 .03	*19.5 0.5
10-vi-54	.0304	0.91 .01	*13.3 0.2		.0617	2.79 .05	*20.1 0.5
2-vi-54	.0399	1.125 .01	*12.5 0.2	3-xii-53	.0721	3.11 .05	*19.1 0.5
9-iii-54	.0404	1.185 .008	*13.0 0.15		.0721	3.13 .07	*19.3 0.5
10-vi-54	.0515	1.47 .02	*12.6 0.2		.0721	3.22 .05	*19.9 0.5
9-iii-54	.0611	1.875 .015	13.6 0.2	30-x-53	.0732	3.51 .08	*21.2 0.5
1-vi-54	.0612	1.85 .03	13.4 0.2	29-i-54	.0800	4.02 .04	*22.3 0.5
9-iii-54	.0819	2.57 .02	13.9 0.2		.1019	4.79 .06	*20.9 0.5
		*Weighted average 12.8 $\pm$ 0.3				*Weighted average 20.6 $\pm$ 0.4	
(f) Temperature = 1.496°K.							
11-iii-54	.0198	0.62 $\pm$ .015	*13.9 $\pm$ 0.4				
2-vi-54	.0397	1.25 .015	*13.9 0.4				
11-iii-54	.0403	1.195 .02	*13.2 0.3				
	.0602	1.83 .02	*13.5 0.2				
	.0794	2.425 .02	*13.5 0.2				
11-vi-54	.1029	3.47 .02	14.9 0.2				
		*Weighted average 13.6 $\pm$ 0.2					

TABLE II

THE WEIGHTED AVERAGE VALUES OF THE VELOCITY INDEPENDENT VISCOSITY OF HELIUM II

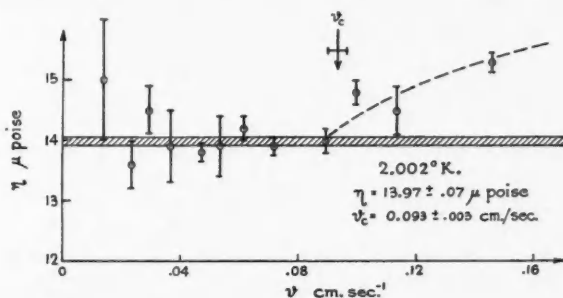
$T, ^\circ\text{K.}$	$\eta, \mu\text{poise}$	$T, ^\circ\text{K.}$	$\eta, \mu\text{poise}$
2.180	23.04	1.400	14.5
2.100	17.40	1.308	15.4
2.002	13.97	1.250	17.5
1.820	12.69	1.200	19.6
1.650	12.8	1.131	20.6
1.496	13.6		

the error of these mean values of  $\eta$  is estimated to be less than about 3% when additional errors due to calibration and eccentricity are taken into account.

The results at the two lowest temperatures, 1.200°K. and 1.131°K., were difficult to obtain. At these temperatures the random oscillation of the inner cylinder about a deflected position had a very much larger amplitude than at higher temperatures. Attempts to reduce the amplitude by application of damping were momentarily successful, but the random amplitude soon increased to its previous large value. In addition to this, there was also in these low temperature measurements the large and variable zero drift discussed in §3. The net result is a large uncertainty in the values of  $\phi$  listed in the table, and a corresponding large uncertainty in the calculated values of  $\eta$ .

The weighted average values of  $\eta$  are collected and shown in Table II.

Values of the 'critical velocity'  $v_c$ , which is to say the value of the velocity which marks the upper limit of the region for which  $\eta$  is independent of velocity, are not easily obtained with any precision. However, from graphs such as those shown in Fig. 4, it is possible to estimate  $v_c$  and to indicate

FIG. 4. The estimation of the 'critical velocity'  $v_c$ .

roughly the uncertainty in the estimate of  $v_c$ . In the representative curve of Fig. 4 the effective viscosity taken from Table I(c) is plotted against velocity, and the error associated with each point is indicated by the vertical bar through the point. The broad band drawn parallel to the velocity axis is centered on the weighted average value at small velocities, and extends

upwards and downwards from this value an amount equal to the error associated with this value. It is then possible to see immediately the departures from the small velocity constant value of  $\eta$  and to estimate  $v_c$ . The vertical arrow in Fig. 4 represents the estimate of  $v_c$ , and the horizontal bar represents the uncertainty in the estimate. These values are collected in Table III and are plotted against temperature in Fig. 5. It can be seen from Fig. 5 that  $v_c$

TABLE III  
THE VALUES OF THE 'CRITICAL VELOCITY'

$T, ^\circ\text{K.}$	$v_c, \text{cm. sec.}^{-1}$	$T, ^\circ\text{K.}$	$v_c, \text{cm. sec.}^{-1}$
2.180	0.25?	1.400	$0.070 \pm .006$
2.100	$0.09 \pm .005$	1.308	$0.080 \pm .004$
2.002	$0.093 \pm .003$	1.250	$0.080 \pm .01$
1.820	$0.095 \pm .003$	1.200	?
1.650	$0.055 \pm .003$	1.131	0.12?
1.496	$0.085 \pm .007$		

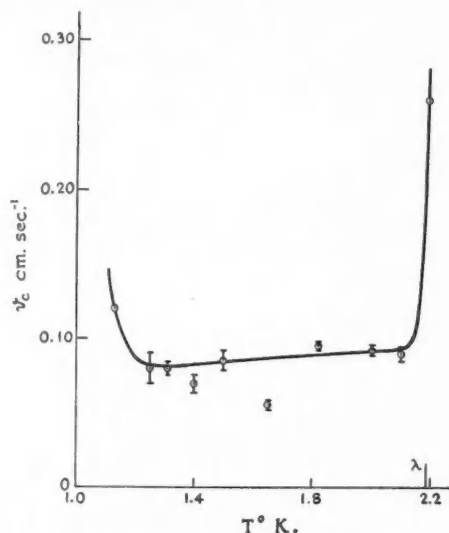


FIG. 5. The variation of the 'critical velocity' with temperature.

appears to increase very slowly with temperature, rising from 0.08 cm./sec. at 1.3°K. to 0.09 cm./sec. at 2.1°K., but increases rapidly between 2.1°K. and the lambda-point, and again below 1.3°K.

#### 6. DISCUSSION OF THE EXPERIMENTAL RESULTS

##### (a) The Values of $v_c$

The values of  $v_c$ , which is defined as the velocity at which the calculated values of  $\eta$  cease to be independent of velocity, are somewhat lower than the



values obtained from the oscillating disk experiments (6). This is, however, not unexpected because it was pointed out in connection with the oscillating disk results that the values of  $v_c$  were dependent upon the period of oscillation of the disk. It was generally observed that  $v_c$  decreased as the period of oscillation increased; at 3.8 sec. period  $v_c = 0.22$  cm. sec.<sup>-1</sup>, and at 11 sec.,  $v_c = 0.16$  cm. sec.<sup>-1</sup>, both being taken at about 1.8°K. Consequently, if one regards the rotating cylinder as equivalent to an oscillating disk of infinite period, the values of  $v_c = 0.08$  cm. sec.<sup>-1</sup> are perhaps not out of line with the oscillating disk values. Again, the temperature dependence of  $v_c$  is qualitatively similar for the two types of experiment, although the rotating cylinder values show a marked increase below 1.3°K. which is not found in the oscillating disk experiments.

There is little one can add to the previous discussion (6, 7) as to the nature of the effects causing the friction in the liquid to increase as  $v_c$  is passed. The maximum Reynolds number which can be calculated for the observed velocities  $v_c$  is 130, this being the value at the lambda-point; the representative distance which appears in the calculation of the Reynolds number has been taken as the width of the gap between the two cylinders. Such a Reynolds number seems too small to suggest turbulence for velocities greater than  $v_c$ , and the results appear to suggest the existence of some strong non-linear frictional forces which are present in the fluid when the velocity exceeds  $v_c$ .

(b) *Comparison of the Present Results with the Extrapolated Values of  $\eta$  Given in the Previous Paper (7)*

The values of  $\eta$  quoted in Table II are all somewhat higher than the values given earlier (7). This is scarcely surprising since the earlier results did not cover the velocity range below 0.1 cm. sec.<sup>-1</sup>, and values of  $\eta$  could only be obtained by extrapolating these large velocity values linearly to zero velocity. It can be seen from Fig. 4 that such a linear extrapolation of the results above 0.1 cm. sec.<sup>-1</sup> will give at zero velocity values of  $\eta$  which are less than those represented by the horizontal band on this curve.

(c) *Comparison of the Present Results with the Theory of Landau and Khalatnikov*

Landau and Khalatnikov (11) have given a theory of the viscosity of liquid helium II which is based on Landau's (10) system of quantum hydrodynamics. The theory considers collision processes between the two types of elementary excitations, phonons and rotons, which Landau's theory provides for liquid helium II. The liquid is considered to be an intimate mixture of two ideal gases, one of phonons and one of rotons, and the theoretical results are valid only if the density of the two gases is not too large. Practically this means that the theory holds for temperatures less than about 1.8°K., and cannot be applied between 1.8°K. and the lambda-point. The effective viscosity of the liquid is considered to be the sum of two parts, one due to collisions of rotons with rotons and phonons, which is independent of temperature. The other part is due to the collisions of phonons with rotons and with phonons, and leads to a viscosity which varies with temperature as  $T^{-\frac{1}{2}} \exp(\Delta/kT)$ . Here  $\Delta$  is the energy gap between the ground states of the

phonon and the roton excitations,  $k$  and  $T$  are respectively Boltzmann's constant and the absolute temperature. The constants in the expression for  $\eta$  involve a number of parameters which are not known with any certainty, so a test of the Landau-Khalatnikov expression can be made if it is written in the form

$$\eta = A + BT^{-\frac{1}{2}} \exp(\Delta/kT)$$

where  $A$  and  $B$  are considered as undetermined constants. A value of  $(\Delta/k) \sim 8^\circ$  has been obtained by Kramers, Wasscher, and Gorter (9) from measurements of the specific heat of liquid helium, and the full curve drawn in Fig. 6 is given by the equation

$$\eta(\mu\text{poise}) = 12.2 + 9.1 \times 10^{-3} T^{-\frac{1}{2}} \exp(8^\circ/T), \quad T < 1.8^\circ\text{K.},$$

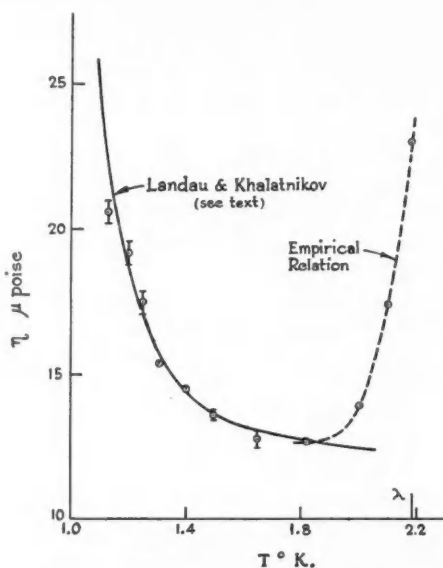


FIG. 6. The variation of the viscosity with temperature.

and it can be seen from this figure that the curve fits the data below  $1.8^\circ\text{K.}$  quite well. Above  $1.8^\circ\text{K.}$ , the Landau-Khalatnikov theory is no longer applicable, and the dashed curve is drawn from the empirical relation

$$\eta(\mu\text{poise}) = 12.7 + 218(T - 1.820)^3, \quad T > 1.8^\circ\text{K.},$$

which fits the results well and is recommended for interpolation purposes.

It should be pointed out that even with  $(\Delta/k)$  chosen, there still remain two adjustable constants  $A$  and  $B$  in the Landau-Khalatnikov expression, and that the agreement between the experimental results and the full curve in Fig. 6 may be to some extent the result of successful curve fitting. It should

also be noted that the theory has been tested against viscosity data which only vary by a factor of 2 in the temperature range covered, and this is scarcely sufficient to determine whether the viscosity varies as  $T^{-1}\exp(\Delta/kT)$  or as some other rapidly varying function of temperature. In spite of this, the Landau-Khalatnikov theory does have the great merit that it predicts the rapid rise of viscosity with decreasing temperature; such a prediction has yet to come from any other theory.

(d) *Comparison with the Oscillating Disk Results*

The present values of  $\eta$ , plotted against temperature, are represented by the full curve in Fig. 7. The various points which appear on the same graph are taken from the oscillating disk results of Andronikashvili (2), de Troyer *et*

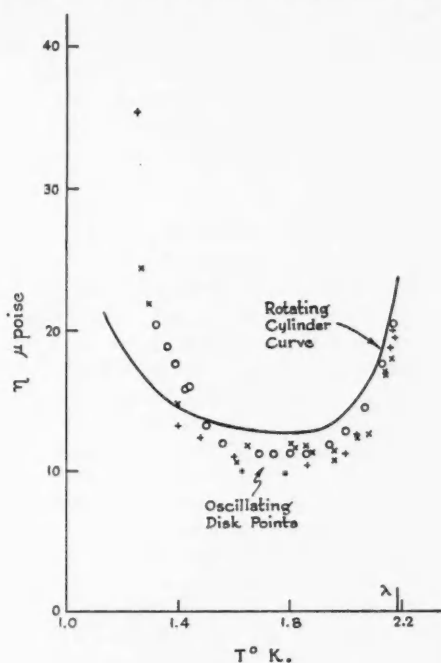


FIG. 7. Comparison of the viscosity results from the rotating cylinder with the oscillating disk values of Andronikashvili (O) (2), Hallett (+) (6), and de Troyer *et al.* (x) (14).

*al.* (14), and Hallett (6). The Leiden results (14) were originally calculated using the total density  $\rho$  rather than the density of the normal component,  $\rho_n$ , and for the purposes of Fig. 7 these results have been recalculated using  $\rho_n$ . It can be seen from this figure that there are considerable discrepancies over the whole temperature range. Below about 1.4°K. the oscillating disk results lie above the rotating cylinder results, but between 1.4°K. and the lambda-point the oscillating disk results are lower.

It should be remembered that for the oscillating disk experiment, the values of  $\eta$  depend on the square of the difference between the observed logarithmic decrement in helium and the logarithmic decrement *in vacuo*. The decrement in helium decreases rapidly as the temperature is lowered, and below 1.4°K. this decrement is of the same order as the vacuum decrement. Consequently, any errors in the vacuum decrement (which is somewhat difficult to obtain exactly) are reflected in the values of  $\eta$  giving them a larger error. This is confirmed by the recent unpublished experiments by Benson of this laboratory, and his results suggest that the discrepancies below 1.4°K. are mainly due to comparatively small errors in the vacuum decrements. In fact, his results below 1.4°K. (actually obtained with an oscillating sphere) agree much better with the full curve of Fig. 7 than with the points which are actually shown on the graph.

Above 1.4°K. the two different types of experiment seem to differ by about 16%, the rotating cylinder results being the higher. In §4(e) it was explained that if corrections for thermal contraction were applied to the results of both types of experiment, the rotating cylinder results might be increased by 4% and the oscillating disk results increased by 2%. Consequently the difference will be increased by about 2%, which almost balances the estimated 3% error in the rotating cylinder results and leaves a discrepancy of about 15% still remaining. There is, of course, considerable scatter in the oscillating disk results, and this scatter would absorb some of the 15% difference between the two sets of results. However, as Fig. 7 shows, the rotating cylinder values of  $\eta$  lie consistently above the oscillating disk values, and it would seem that there is a definite and real discrepancy, perhaps as large as 10%, and that this discrepancy persists right up to the lambda-point. In this connection it should be mentioned that experiments performed to investigate whether or not this discrepancy existed in helium I were unsuccessful because of the jolting of the inner cylinder against its constraints by the bubbles of gas formed in the boiling helium I. Although several attempts were made to eliminate this disturbance, they were only successful for short periods of time, and it was not possible to establish sufficiently steady conditions for the hour required to measure deflections right and left of zero at one velocity.

It is tempting to suggest that the reason for the discrepancy may lie in the data for  $\rho_h$  used to reduce the oscillating disk results, particularly because the data are usually calculated from the velocity of second sound using an equation which has been criticized by Gorter, Kasteleijn, and Mellink (5). But, the discrepancies appear at the highest temperatures where confirming values of  $\rho_h$  have been obtained directly by Andronikashvili (1) using the oscillating pile of plates.

It appears therefore that the discrepancies are real and in some way significant, perhaps associated with the different types of fluid motion which are found in the two experiments. In the rotating cylinder experiment, the fluid velocities are constant and accelerations are zero. In the oscillating disk experiments, the fluid accelerations are large and variable, and are the important factor in the motion. Perhaps too, the discrepancy may point to

the existence of some sort of relaxation process in the fluid, the characteristic time being larger than about 20 sec., the largest period of oscillation used in oscillating disk experiments. It is difficult to conceive of a process in liquid helium II, according to the present understanding of the substance, which would give a relaxation time of the order of minutes, and it is fruitless to discuss this point further until the results of more definitive experiments on this problem are fully known.

#### ACKNOWLEDGMENTS

The authors are indebted to the Royal Society Mond Laboratory of Cambridge, England, for the extended loan of the viscometer with which these measurements were made. They are also indebted to the National Research Council of Canada for numerous grants in aid of research, and to the Canadian General Electric Company for the tungsten suspension fibers. One of us (WJH) is indebted to the trustees of the Garnet W. McKee - Lachlan Gilchrist Scholarship for their grants of scholarships.

#### REFERENCES

1. ANDRONIKASHVILI, E. L. J. Phys. (U.S.S.R.), 10: 201. 1946. J. Exptl. Theoret. Phys. (U.S.S.R.), 18: 424. 1948.
2. ANDRONIKASHVILI, E. L. J. Exptl. Theoret. Phys. (U.S.S.R.), 18: 429. 1948.
3. BEARDEN, J. A. Phys. Rev. 56: 1023. 1939.
4. VAN DIJK, H. and SHOENBERG, D. Nature, 164: 151. 1949.
5. GORTER, C. J., KASTELEIJN, P. W., and MELLINK, J. H. Physica, 16: 113. 1950.
6. HOLLIS HALLETT, A. C. Proc. Roy. Soc. (London), A, 210: 404. 1952.
7. HOLLIS HALLETT, A. C. Proc. Cambridge Phil. Soc. 49: 717. 1953.
8. HOUSTON, W. V. Phys. Rev. 52: 751. 1937.
9. KRAMERS, H. C., WASSCHER, J. D., and GORTER, C. J. Physica, 19: 329. 1952.
10. LANDAU, L. D. J. Phys. (U.S.S.R.), 5: 71. 1941; 11: 91. 1947.
11. LANDAU, L. D. and KHALATNIKOV, I. M. J. Exptl. Theoret. Phys. (U.S.S.R.), 19: 637, 709. 1949.
12. MILLIKAN, R. A. Ann. Physik, 41: 759. 1913.
13. MILNE-THOMSON, L. M. Theoretical hydrodynamics. 2nd ed. The MacMillan Co., New York. 1950. p. 519.
14. DE TROYER, A., VAN ITERBEEK, A., and VAN DEN BERG, G. J. Physica, 18: 50. 1951.

# SOME CONSIDERATIONS REGARDING THE PRINCIPLE OF PHASE INVARIANCE<sup>1</sup>

BY F. A. KAEMPFER

## ABSTRACT

Taking the view that "particles" are in fact excitations of the motion of an all-pervading medium (or "ether"), it is shown that the conservation laws characterizing the ether, which are different from the well-known laws of conservation of energy and momentum, flow from a single principle, the principle of phase invariance, provided a complex field is used to describe the ether. There are at least two different self-consistent types of Lorentz-invariant ether theories which satisfy the principle of phase invariance.

In view of the fact that the accepted classical and quantum field theories cannot explain the reason for the very existence of the various so-called elementary particles, a number of authors (2, 5), led by Dirac (4), have reverted in recent years to the old idea of an all-pervading medium, or "ether", which is considered as the underlying substance in which all material phenomena are generated, so that in particular the different possible receptacles for energy and momentum, usually called "particles", appear as different possible excitations of the motion of that substance.

The common feature of these initially widely different approaches is the necessity to introduce variables designed to describe the "glue" which holds the various excitations of the motion together, so that the appearance of stable entities or "particles" becomes possible.

It is the purpose of this paper to show that the conservation laws characterizing the all-pervading medium, (which have to be distinguished and are quite different from the laws of conservation of energy and momentum characterizing the excitations of that medium), can be derived from a single principle, the principle of phase invariance, provided a complex field is used to describe the medium.

For simplicity's sake let us assume that the all-pervading medium can be described by a scalar complex function  $\psi(x, y, z, t)$  so that the following Lorentz-invariant action principle is satisfied:

$$[1] \quad \delta \int \mathcal{L} dt = 0, \quad \mathcal{L} = \int L dV, \quad L = \frac{\partial \psi^*}{\partial x_\nu} \frac{\partial \psi}{\partial x_\nu}, \quad \nu = 1, 2, 3, 4, \quad x_4 = ict.$$

In the conventional language one would say that we are considering the classical (i.e. unquantized) field of spinless mesons of mass zero.

It was Dirac (3) who first quite clearly observed the fact that the phase of any complex  $\psi$ -field can be utilized to describe the presence of forces acting on the  $\psi$ -field. Writing

$$[2] \quad \psi = \psi_0 e^{i\Omega}, \quad \psi_0 = R e^{i\chi}, \quad R \text{ real, } \chi \text{ single-valued,}$$

where  $\Omega$  is the multivalued part of the phase, so that only its derivatives  $\partial\Omega/\partial x_\nu$  are defined uniquely everywhere, we obtain from [1]

<sup>1</sup>Manuscript received April 25, 1955.

Contribution from the Department of Physics, University of British Columbia, Vancouver 8, British Columbia.

$$[3] \quad L = \frac{\partial \psi_0^*}{\partial x_r} \frac{\partial \psi_0}{\partial x_r} + i \left( \psi_0 \frac{\partial \psi_0^*}{\partial x_r} - \psi_0^* \frac{\partial \psi_0}{\partial x_r} \right) \frac{\partial \Omega}{\partial x_r} + \psi_0^* \psi_0 \frac{\partial \Omega}{\partial x_r} \frac{\partial \Omega}{\partial x_r}.$$

It is very tempting indeed to identify the derivatives  $\partial \Omega / \partial x_r$  with the electromagnetic potentials  $\epsilon A_r$ , because imposition of the principle of phase invariance in the form

$$[4] \quad \frac{\delta \mathcal{L}}{\delta \Omega} = 0, \quad \text{i.e.} \quad \frac{\partial}{\partial x_r} \frac{\partial L}{\partial (\partial \Omega / \partial x_r)} = 0,$$

yields a conservation law

$$[5] \quad \frac{\partial j_r}{\partial x_r} = 0, \quad \text{with } j_r = i \left( \psi_0 \frac{\partial \psi_0^*}{\partial x_r} - \psi_0^* \frac{\partial \psi_0}{\partial x_r} \right) + 2 \psi_0^* \psi_0 \frac{\partial \Omega}{\partial x_r},$$

which can be interpreted as the law of conservation of charge, in a form familiar from the usual interpretation of wave mechanics, provided

$$[6] \quad \partial \Omega / \partial x_r = \epsilon A_r.$$

In addition, variation of the Lagrangian [3] with respect to  $\psi_0^*$  yields the well-known Klein-Gordon equation, which is generally believed to describe a charged "particle" (of mass zero in the case considered here) moving in an electromagnetic field derived from the potentials  $A_r$ . Dirac (3) puts it this way: "The whole effect of the field when there is one is in making the phase non-integrable".

Unfortunately, the principle of phase invariance, when put in the form [4], has no foundation at all. One cannot use a multivalued function  $\Omega$  as independent variable in a variational principle. In fact,  $\Omega$  is characterized by four independent variables, namely its derivatives  $\partial \Omega / \partial x_r$ , which we have assumed to be uniquely defined everywhere.

It appears that there are at least two possible ways out of this difficulty, provided one wishes to hang on to the principle of phase invariance, which we definitely do.

One possibility is to keep the interpretation [6] of  $\partial \Omega / \partial x_r$  being the electromagnetic potentials and to express the principle of phase invariance in the form

$$[7] \quad \delta \mathcal{L} / \delta A_r = 0.$$

In order to make this meaningful, one has to add to [3] the well-known Lagrangian density of the radiation field

$$[8] \quad L_{\text{rad.}} = -\frac{1}{4} \left( \frac{\partial A_r}{\partial x_\mu} - \frac{\partial A_\mu}{\partial x_r} \right)^2 - \frac{1}{2} \left( \frac{\partial A_\mu}{\partial x_\mu} \right)^2$$

so that equations [7] become Maxwell's equations

$$[9] \quad \square^2 A_r = j_r, \quad \text{with } j_r = i \left( \psi_0 \frac{\partial \psi_0^*}{\partial x_r} - \psi_0^* \frac{\partial \psi_0}{\partial x_r} \right) + 2 \psi_0^* \psi_0 \epsilon A_r,$$

which together with the Klein-Gordon equation

$$[10] \quad \left( \frac{\partial}{\partial x_r} - i \epsilon A_r \right)^2 \psi_0 = 0$$

form a simultaneous system of five nonlinear equations for the five variables  $\psi_0, A_\nu$ . One might look upon the electromagnetic potentials  $A_\nu$  in this case as the "glue" which holds the massless  $\psi_0$ -field together, so that stationary solutions of the nonlinear system [9], [10] can be interpreted as "particles", the electromagnetic properties of which would be revealed to an observer through the potentials  $A_\nu$ , while their mechanical properties can be calculated uniquely for each solution of the system [9], [10] from the energy-momentum tensor

$$[11] \quad T_{\mu\nu} = -\frac{\partial f_\sigma}{\partial x_\nu} \frac{\partial L}{\partial (\partial f_\sigma / \partial x_\mu)} + L \delta_{\mu\nu}, \quad f_\sigma = (\psi_0, \psi_0^*, A_1, A_2, A_3, A_4).$$

The observable mass of each "particle", in particular, would be given by

$$[12] \quad m = -\frac{1}{c^2} \int T_{44} dV.$$

Since this approach can be extended easily to a description of the "ether" in terms of a spinor field of mass zero, it has been favored by Kaempffer (6), who seems to believe that neutrinos and photons are basic building stones of elementary particles.

A quite different approach, which avoids somewhat arbitrary additions of the type [8] to the original Lagrangian density [3], is contained in an interesting transformation suggested by Schönberg (8). Introduce two pairs of Clebsch potentials  $\lambda_s, \mu_s$  ( $s = 1, 2$ ), so that

$$[13] \quad \frac{\partial \Omega}{\partial x_\nu} = \lambda_s \frac{\partial \mu_s}{\partial x_\nu}.$$

The total phase of the  $\psi$ -field is thus characterized by five independent variables  $\chi, \lambda_s, \mu_s$ . Contact transformations of the type

$$[14] \quad \lambda_s d\mu_s - \lambda'_s d\mu'_s = d\chi$$

can be absorbed by the single-valued part of the phase  $\chi$ . Now the Lagrangian density [3] takes the form

$$[15] \quad L = \left( \frac{\partial R}{\partial x_\nu} \right)^2 + R^2 \left( \frac{\partial \chi}{\partial x_\nu} + \lambda_s \frac{\partial \mu_s}{\partial x_\nu} \right)^2.$$

Imposition of the principle of phase invariance yields then five conservation laws

$$[16] \quad \frac{\delta \mathcal{L}}{\delta \chi} = 0, \quad \frac{\delta \mathcal{L}}{\delta \lambda_s} = 0, \quad \frac{\delta \mathcal{L}}{\delta \mu_s} = 0,$$

which read explicitly

$$[16a] \quad \frac{\partial}{\partial x_\nu} \left\{ R^2 \left( \frac{\partial \chi}{\partial x_\nu} + \lambda_s \frac{\partial \mu_s}{\partial x_\nu} \right) \right\} = 0,$$

$$[16b] \quad \left( \frac{\partial \chi}{\partial x_\nu} + \lambda_r \frac{\partial \mu_r}{\partial x_\nu} \right) \frac{\partial \mu_s}{\partial x_\nu} = 0,$$



$$[16c] \quad \left( \frac{\partial \chi}{\partial x_r} + \lambda_r \frac{\partial \mu_r}{\partial x_r} \right) \frac{\partial \lambda_s}{\partial x_r} = 0,$$

while the "equation of motion" follows from [15] upon variation of  $R$ :

$$[17] \quad \left( \frac{\partial \chi}{\partial x_r} + \lambda_r \frac{\partial \mu_r}{\partial x_r} \right) \frac{\partial \chi}{\partial x_r} = \frac{\square^2 R}{R}.$$

(In [16c] use has been made of [16a], and in [17] use has been made of [16b].) Introduction of the "velocity" of the ether

$$[18] \quad u_r = \frac{\partial \chi}{\partial x_r} + \lambda_r \frac{\partial \mu_r}{\partial x_r}$$

casts the conservation laws [16] into the form

$$[16a] \quad \frac{\partial}{\partial x_r} (R^2 u_r) = 0,$$

$$[16b] \quad u_r \frac{\partial \mu_s}{\partial x_r} = 0,$$

$$[16c] \quad u_r \frac{\partial \lambda_s}{\partial x_r} = 0,$$

which invite a simple interpretation. If  $R^2 = |\psi|^2$  is called the "density" of the ether, [16a] expresses the conservation of substance, while [16b] and [16c], stating that the substantial derivatives of  $\lambda_s$  and  $\mu_s$  vanish, express the law of conservation of vorticity, i.e. that the vortex lines, which from [18] are seen to be identical with the intersections of the surfaces  $\lambda_s = \text{constant}$  and  $\mu_s = \text{constant}$ , move with the substance. We have, in fact, recovered Buneman's theorem (which was derived by Buneman (1) on quite different premises): *The flow vector of the ether maintains constant circulation*. This theorem has also been used, again in an apparently different context, by Takabayasi (9).

It might be worth noting here that both Buneman (2) and Takabayasi (9) impose on the velocity vector  $u_r$  the condition

$$[19] \quad u_r u_r = -c^2.$$

The present author thinks that this is an unnecessary restriction. It is true that [19] holds for observable matter, and in particular for "particles". But since we are contemplating here the possibility that "particles" are particular manifestations of a mother substance of higher rank, we should not expect that this substance behaves in every respect like ordinary matter. It might turn out to be necessary to consider, say, action at a distance in the underlying medium; this need not be at variance with experimental facts, as long as the mechanical behavior of the excitations of the motion as a whole, to be calculated from the energy-momentum tensor

$$[20] \quad T_{\mu\nu} = -\frac{\partial g_\sigma}{\partial x_\nu} \frac{\partial L}{\partial (\partial g_\sigma / \partial x_\mu)} + L \delta_{\mu\nu}, \quad g_\sigma = (R, \chi, \lambda_1, \lambda_2, \mu_1, \mu_2),$$

exhibits the properties of observable matter.

In this approach the variables  $\chi$ ,  $\lambda_s$ ,  $\mu_s$  play the part of the glue which holds the  $R$ -field together. Stationary solutions of the simultaneous system of nonlinear equations [16], [17] can again be interpreted as "particles", provided reasonable boundary conditions are satisfied by these solutions.

No attempt will be made here to solve this difficult mathematical problem. (An instructive solution for the nonrelativistic case has been studied by Schönberg (7).) It should be noted, however, that the observable mass associated with each "particle" can again in principle be calculated uniquely according to the prescription [12], with  $T_{44}$  now given by the definition [20]. Once the Clebsch potentials  $\lambda_s$ ,  $\mu_s$  have been calculated explicitly for a given excitation interpreted as a particle, the electromagnetic properties of that particle should also follow uniquely from the identification [6]. One may thus distinguish between neutrino-like, photon-like, and electron-like excitations, as has been suggested by Kaempffer (5).

Only a detailed investigation of all possible solutions of the nonlinear systems [9], [10] and [16], [17] respectively can decide which of the two approaches possesses contact with reality. If it should turn out that the concept of an ether is indeed the key to the understanding of the structure of elementary particles, the principle of phase invariance may well emerge as the one fundamental principle from which flow all conservation laws which characterize that ether.

#### REFERENCES

1. BUNEMAN, O. Proc. Roy. Soc. (London), A, 215: 346. 1952.
2. BUNEMAN, O. Proc. Cambridge Phil. Soc. 50: 77. 1954.
3. DIRAC, P. A. M. Proc. Roy. Soc. (London), A, 133: 60. 1931.
4. DIRAC, P. A. M. Proc. Roy. Soc. (London), A, 209: 291. 1951; 212: 330. 1952.
5. KAEMPFER, F. A. Can. J. Phys. 31: 629. 1953; 32: 430. 1954.
6. KAEMPFER, F. A. Phys. Rev. In press. 1955.
7. SCHÖNBERG, M. Nuovo cimento, 12: 300. 1954.
8. SCHÖNBERG, M. Nuovo cimento, 12: 649. 1954.
9. TAKABAYASI, T. Progr. Theoret. Phys. (Japan), 9: 187. 1953.

# CAPTURE RADIATION AND NEUTRONS FROM THE BOMBARDMENT OF $C^{14}$ WITH PROTONS<sup>1</sup>

BY G. A. BARTHOLOMEW, F. BROWN,<sup>2</sup> H. E. GOVE,  
A. E. LITHERLAND, AND E. B. PAUL

## ABSTRACT

The yield and angular distribution of ground state  $\gamma$ -rays and of neutrons resulting from the proton bombardment of  $C^{14}$  have been studied for proton energies from 0.2 to 2.5 Mev. Assignments of spin and parity are made to most of the resonances observed in this range. A single particle proton state which may have isotopic spin  $3/2$  has been observed. The interference of this state, which has spin  $1/2+$ , with a neighboring state of the same spin and parity is observed in the total yield of the ground state  $\gamma$ -ray. Three states below the neutron threshold which have been observed previously in the  $N^{14}(d, p)N^{15}$  reaction are also observed in the  $C^{14}(p, \gamma)N^{15}$  reaction. The  $N^{14}(n, p)C^{14}$  cross section at thermal energies can be accounted for by a resonance observed in this experiment, but another resonance below the neutron threshold must be assumed to account for the thermal  $(n, n)$  and  $(n, \gamma)$  cross sections.

## INTRODUCTION

The neutron, proton, and  $\alpha$ -particle binding energies in  $N^{15}$  are all very similar and therefore the unbound states which are reached by bombarding energies of a few Mev. can be studied by many different reactions. Excited states above 10.8 Mev. are produced by the  $N^{14}+n \rightarrow N^{15*}$  reaction, while states below this energy have been reached by the  $N^{14}(d, p)N^{15}$  reaction. Excited states above 11 Mev. are produced by the  $B^{11}+He^4 \rightarrow N^{15*}$  reaction. Finally, the reaction  $C^{14}+H^1 \rightarrow N^{15*}$ , which, because of the long life of  $C^{14}$ , is feasible experimentally, produces excited states above 10.2 Mev. Below 10.8 Mev. only radiation will compete with elastic proton scattering, while above 11 Mev. decay by emission of neutrons, protons, alpha particles, and radiation will all compete.

The yield curve for elastic scattering of neutrons from  $N^{14}$  has been studied up to about  $E_n = 4$  Mev. (6, 7, 11, 16, 18), and the angular distribution of the neutrons has been observed at a few of the resonances (6). About 14 resonances are observed in this energy range. The yield curve for the  $N^{14}(n, p)C^{14}$  reaction has been studied in a similar energy range (4, 10, 24, 25, 28). The  $N^{14}(n, \alpha)B^{11}$  reaction has been studied up to  $E_n = 8.7$  Mev. (4, 10, 24, 25, 28). About six of the resonances are seen in all three neutron reactions. The  $N^{14}(d, p)N^{15}$  reaction leading to states above the proton binding energy has been studied by Sperduto *et al.* (23), who observed proton groups corresponding to four states in the region between the proton and neutron binding energies at excitations 10.46, 10.54, 10.70, and 10.81 Mev. Numerous resonances have been reported (8, 27) in the reaction  $B^{11}(\alpha, n)N^{14}$ , but these in general correspond to higher excitation in  $N^{15}$  than that being considered here.

<sup>1</sup>Manuscript received March 22, 1955.

Contribution from Physics Division, Atomic Energy of Canada Limited, Chalk River Laboratory, Chalk River, Ontario. Issued as A.E.C.L. No. 182.

<sup>2</sup>Present address: Department of Chemistry, Atomic Energy Research Establishment, Harwell, England.

The yield of neutrons from the reaction  $C^{14}(p, n)N^{14}$  has been studied from threshold to  $E_p = 2.5$  Mev. (20, 21). Again nine of the resonances seen in other reactions are observed and the angular distribution of the neutrons at four of these resonances has been reported (12). The yield of the reaction  $C^{14}(p, \gamma)N^{15}$  for the ground state  $\gamma$ -ray in the region  $E_p = 0.8$  to 2.0 Mev. has been studied by Spearman *et al.* (22).

In the work reported here the yield of the ground state  $\gamma$ -ray in the reaction  $C^{14}(p, \gamma)N^{15}$  has been measured from  $E_p = 0.2$  to 2.5 Mev., and angular distributions have been measured at the resonances observed. A preliminary report of this work has already been published (2). The yield of the  $C^{14}(p, n)N^{14}$  reaction was measured simultaneously with that of the  $(p, \gamma)$  reaction and the angular distributions of the neutrons were observed at 12 proton energies throughout the energy range.

#### EXPERIMENTAL ARRANGEMENTS

The proton beam from the Chalk River electrostatic accelerator was used to bombard the carbon targets. For some of the work below  $E_p = 0.7$  Mev. the mass-2 or mass-3 beams from the magnetic analyzer were used instead of the atomic ion beam. The magnetic field was held constant by a proton resonance fluxmeter. A pair of plates forming a horizontal slit at the exit of the magnet provided a signal to control a corona load which stabilized the energy to about 1 kev. The absolute voltage of the machine, calibrated on known thresholds and resonances in terms of a proton resonance fluxmeter in the field of the analyzer magnet, was known to 2 or 3 kev. in this work. The targets consisted of elemental carbon containing 25%  $C^{14}$  deposited on 0.020-in. Ta sheet. They were prepared by heating the 1-in. square Ta blanks, after careful cleaning and outgassing, in an atmosphere of carbon monoxide containing  $C^{14}$ . The heating was done by an induction furnace and was carried on until a target of the desired thickness was obtained. Two targets were used in this work, one about 6 kev. thick (at  $E_p = 1$  Mev.), and the other about 50 kev. thick. The targets were quite stable under long bombardment with beam currents up to 10  $\mu$ a. A liquid air trap around the beam pipe about one foot from the target was used to trap organic vapors in the vacuum system. The general layout is shown in Fig. 1. The  $C^{14}$  abundance in the carbon monoxide was determined in a mass spectrometer.

The  $\gamma$ -rays were detected during most of the work by a 2 in. long by 2 in. diameter NaI(Tl) crystal mounted on a Dumont 6292 photomultiplier. In some of the later work a 4 in. long by 5 in. diameter crystal mounted on a Dumont K-1198 photomultiplier was used. The amplified pulses were displayed on a 30-channel pulse height analyzer. The computed efficiency of the 2-in. spectrometer was checked using the 6.13 Mev.  $\gamma$ -ray from the  $F^{19}(p, \alpha\gamma)O^{16}$  reaction. The computed yield agreed with the known yield (1) to within five per cent. The computed efficiency curve was therefore used to obtain the efficiency for the  $\gamma$ -rays from capture in  $C^{14}$ . For angular distributions the scintillation spectrometer could be rotated around the target in the plane of the proton beam. An identical spectrometer was fixed at  $90^\circ$  to the beam and served as a monitor. The geometry of the system was fixed by mounting

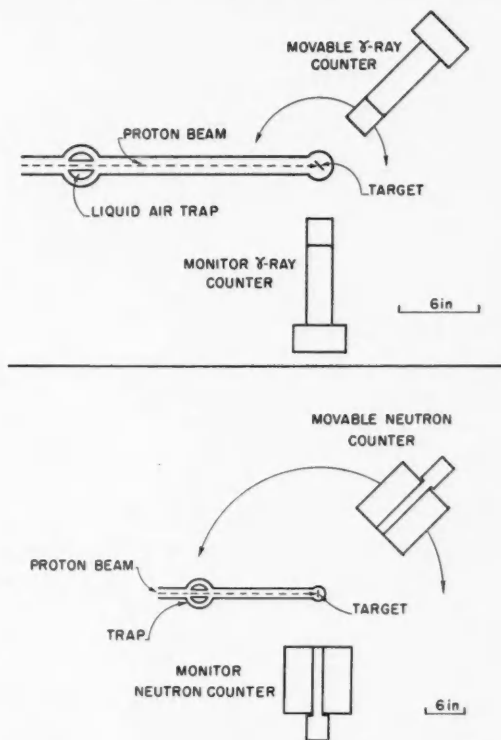


FIG. 1. Schematic view of the arrangements for  $\gamma$ -ray and neutron angular distribution measurements in the proton bombardment of  $C^{14}$ .

both spectrometers on a heavy table which could be accurately oriented with respect to beam and target.

The neutrons were detected with two slightly different counters. One consisted of a  $B^{10}F_3$  counter of 2 in. diameter by 6 in. long sensitive volume, surrounded by a 2-in. layer of paraffin wax. This counter was used to measure the yield curve (see Fig. 5). For the angular distributions two similar  $BF_3$  counters, mounted axially in paraffin cylinders 10 in. in diameter and 10 in. long, were used, one as the movable counter on a light frame, the other fixed at  $90^\circ$  to the beam as a monitor (see Fig. 1).

For most of the experiments, the front face of the 2-in. scintillation spectrometer was fixed at 4 in. from the target spot which was defined by apertures to be  $\frac{1}{8}$  in. diameter. For some of the weaker resonances the counter was set at  $2\frac{1}{2}$  in. from the target, but all angular distribution measurements were made at the former distance. For yield curves the neutron counter was set at 8 in. from the target, while for neutron angular distributions the front face of the counter was 13 in. from the target.

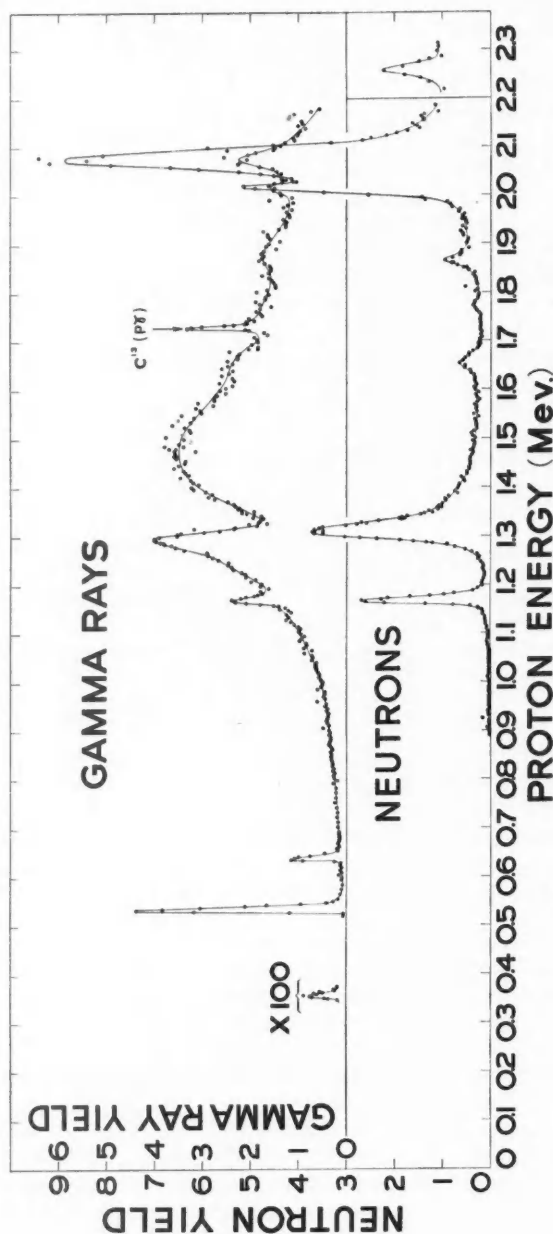


Fig. 2. Relative yields of ground state  $\gamma$ -rays and of neutrons from the proton bombardment of  $C^{13}$ . For both curves below 2.2 Mev., measurements were made at  $90^\circ$ . The neutron yield above 2.2 Mev. was measured at  $0^\circ$ .

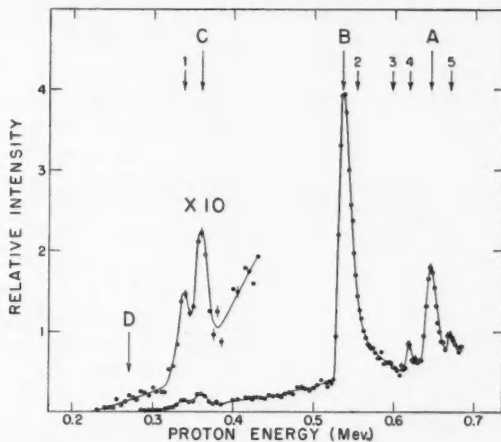


FIG. 3. Yield curve for  $\gamma$ -rays of energy greater than 3.8 Mev. The resonances A, B, and C at  $E_p = 0.646$ , 0.537, and 0.361 Mev. are produced by the  $C^{14}+p$  reaction. A fourth  $C^{14}$  resonance, D, expected at  $E_p = 0.270$ , was not observed.  $F^{19}(p, \alpha\gamma)$  resonances 1 and 5 at  $E_p = 0.340$  and 0.669 Mev. were used to calibrate the energy scale. Another  $F^{19}(p, \alpha\gamma)$  resonance at 0.598 Mev., (3), and a  $C^{13}(p, \gamma)$  resonance at 0.554 Mev., (2), presumably contribute to the counting rate between peaks A and B. The origin of the resonance, (4), at 0.619 Mev. is unknown. The errors shown are statistical errors.

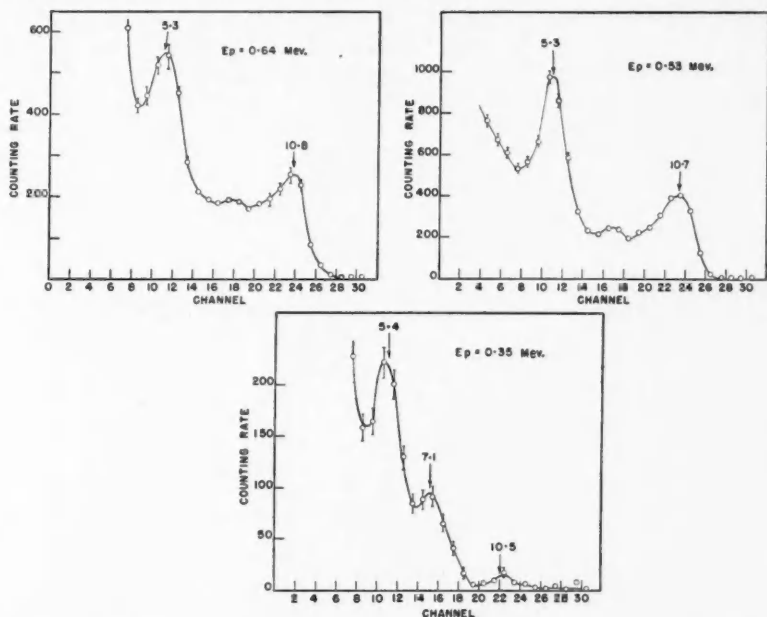


FIG. 4. High energy  $\gamma$ -ray spectra at  $C^{14}(p, \gamma)$  resonances  $E_p = 0.361$ , 0.537, and 0.646 Mev. measured with a 2 in. long by 2 in. diameter NaI crystal. The errors shown are statistical errors. The ordinate scale is in arbitrary units.

## YIELD CURVES

The complete yield curve for both neutrons and the ground state  $\gamma$ -ray is shown in Fig. 2. The yield of  $\gamma$ -rays of energy greater than 3.8 Mev. for proton energies below the neutron threshold is shown in more detail in Fig. 3. Table I lists the observed resonance positions together with the positions of

TABLE I  
 $C^{14}(p, \gamma)N^{15}$  RESONANCES BELOW THE NEUTRON THRESHOLD

	$E_p$ , Mev.	$N^{15}$ level, <sup>a</sup> Mev.	$N^{15}$ levels from $N^{14}(d, p)N^{15}$ , <sup>b</sup> Mev.
A	0.646	$10.818 \pm .008$	$10.811 \pm .012$
B	0.537	$10.716 \pm .008$	$10.705 \pm .012$
C	0.361	$10.552 \pm .008$	$10.544 \pm .012$
D	(0.270)	Not observed	$10.458 \pm .012$

<sup>a</sup>Q-value assumed to be  $10.215 \pm .007$  Mev.

<sup>b</sup>As reported by Sperduto et al. (23).

the levels reported from the  $N^{14}(d, p)N^{15}$  reaction (23). The proton energy calibration for this region was based on the positions of the 0.340 and 0.669 Mev. resonances in  $F^{19}(p, \alpha\gamma)$ , which were also observed, and arose from a slight fluorine contamination on the target. In Fig. 4 are shown the high energy spectra obtained with the 2-in. spectrometer at the three resonances. The ground state transition at the 0.361 Mev. resonance is extremely weak and no evidence was found that this weak  $\gamma$ -ray is resonant here. No resonance

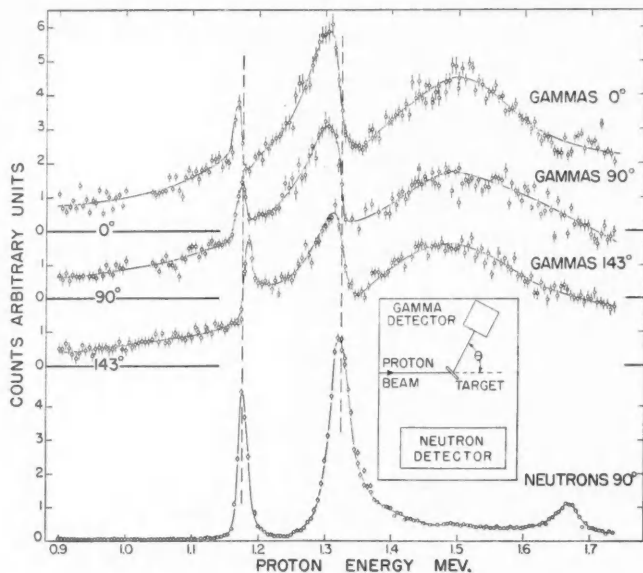


FIG. 5. Relative yields of  $\gamma$ -rays and of neutrons between 0.9 and 1.7 Mev. The errors shown are statistical errors.



was found in the region of 0.27 Mev. proton energy corresponding to the state reported in the  $N^{14}(d, p)N^{15}$  reaction at 10.458 Mev.

In Fig. 5 is shown the next portion of the yield curve, the lower curve being that for neutrons emitted at  $90^\circ$  to the beam, and the three upper curves being the yield of the ground state  $\gamma$ -ray ( $\gamma_0$ ) only, at  $0^\circ$ ,  $90^\circ$ , and  $143^\circ$  to the proton beam. The neutron curve agrees well with the observations of Roseborough *et al.* (20). The broad  $\gamma$ -ray resonance at 1.5 Mev. was also observed by Spearman *et al.* (22), although our observations differ from theirs in some other details. It is to be noted that in the region of 1.31 Mev. the  $\gamma$ -ray yield curve shows an interference shape which proceeds from maximum to minimum near the position of the resonance in the neutron yield. Moreover, this shape persists at all three angles, suggesting that it represents the total cross section variation. The yield in the region of 1.17 Mev., however, shows a cosine dependence on angle, and at  $90^\circ$  shows the usual resonance shape. More detailed angular distributions will be discussed below.

Although the yield curve for ground state  $\gamma$ -radiation is shown in Fig. 2 up to  $E_p = 2.2$  Mev., no yield measurements are being reported for resonances higher than 1.7 Mev. Above this energy the separation of the ground state  $\gamma$ -ray line in the spectrum was not always so distinct as at lower energies. Part of the  $\gamma$ -ray background may have been due to slow neutron capture in the iodine in the crystal, and in some cases secondary  $\gamma$ -rays of energies approaching that of the ground state transition in  $N^{15}$  were appearing above the bias used and could not easily be separated. Accordingly the appearance of resonances above 1.7 Mev. must be accepted with some reserve.

The absolute yields of  $\gamma$ -rays and neutrons for each of the resonances are listed in Table II. The  $\gamma$ -ray yields are based on the calibration of the spectrometer as described above. As noted in Table II the  $\gamma$ -ray yield quoted for the resonance at 1.31 Mev. is much less accurate than the other yields. This is because most of the yield curve in this region arises from the interference of

TABLE II  
RESONANT YIELDS FOR  $C^{14}(p, \gamma_0)N^{15}$  AND  $C^{14}(p, n)N^{14}$  REACTIONS

$E_p$ , Mev.	$Y_{\gamma_0}^a$ , photons/ $10^{11}$ protons	$Y_n^a$ , neutrons/ $10^8$ protons	$J^b$
0.361	0.01		
0.537	5.7		
0.646	0.49		
1.165	3.1	20	1/2, (3/2)
1.310	7.9	120	1/2
1.50	49	88	
1.66		17	3/2
1.79		1.5	3/2, 5/2
1.88		5.6	1/2
2.02		40	5/2
2.08		290	3/2, 5/2
2.27		10	5/2

<sup>a</sup>Errors in the yields are estimated to be about 20%, except for the  $(p\gamma_0)$  yield at 1.31 Mev., which may be in error by a factor of two.

<sup>b</sup>Assignments based on a comparison with the reported values of  $\sigma_{nn}$  as described in text.

this state and the wide state at 1.50 Mev., and a detailed fit which can determine the phase difference between the two resonances must be made before the maximum resonant yield can be determined. Such a calculation is under way. The quoted value represents the result of a very crude preliminary fit, and may be in error by as much as a factor of two. The neutron counter was not calibrated directly, but the yield for the  $N^{14}(n, p)C^{14}$  reaction quoted by Johnson and Barschall (10) was used to compute, by detailed balancing, the yield of the  $C^{14}(p, n)N^{14}$  reaction at the 1.31 Mev. resonance. Then the yield of neutrons of the other resonances was computed from this calibration, assuming the counter efficiency to be independent of energy. The width of this state was assumed to be 43 kev.

From the values of the absolute neutron yield and the total width of a resonance, the value of the  $(p, n)$  cross section may be derived. The ratio of the neutron elastic scattering cross section to the  $(p, n)$  cross section can then be used to derive a value of  $\Gamma_n/\Gamma_p$ . The  $(p, n)$  yield also leads to a value of  $\frac{(2J+1)}{2(2I+1)} \frac{\Gamma_n \Gamma_p}{\Gamma}$  where  $J$  is the spin of the compound state and  $I$  is the spin of the target nucleus. Thus one is led to a value of  $J$  most consistent with these data, and it is this assignment which is listed in Table II. The values of  $\sigma_{nn}$  used in these estimates are those reported by Hinchey *et al.* (7). The value of  $\sigma_{nn}$  at the 1.50 Mev. resonance is unknown.

#### ANGULAR DISTRIBUTIONS

The angular distributions of the ground state  $\gamma$ -ray at the six resonances observed are shown in Fig. 6. The smooth curve in each case is a least squares

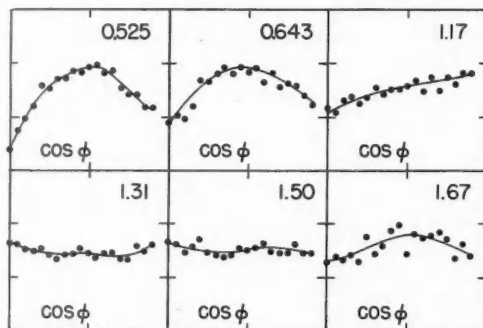


FIG. 6. Angular distribution of the ground state  $\gamma$ -ray from the  $C^{14}(p, \gamma)N^{15}$  reaction. The relative intensities are plotted as a function of the cosine of the center of mass angle (from +1.0 to -1.0). The numbers on the curves refer to the proton energy in Mev. The ordinate scales in different graphs are not related.

fit to a series of Legendre polynomials up to and including  $P_4$ . The fitted coefficients (with errors computed according to the method suggested by Rose (19)) are listed in Table III.

TABLE III  
GROUND STATE  $\gamma$ -RAY ANGULAR DISTRIBUTIONS: FITTED CURVES  
 $W(\theta) = a_0P_0 + a_1P_1 + a_2P_2 + a_3P_3 + a_4P_4$

$E_p$	$a_1/a_0$	$a_2/a_0$	$a_3/a_0$	$a_4/a_0$
0.537	$+0.039 \pm 0.033$	$-0.625 \pm 0.043$	$-0.166 \pm 0.052$	$+0.040 \pm 0.048$
0.646	$-0.033 \pm 0.049$	$-0.412 \pm 0.064$	$-0.089 \pm 0.078$	$+0.072 \pm 0.072$
1.165	$-0.214 \pm 0.038$	$-0.008 \pm 0.050$	$+0.085 \pm 0.061$	$-0.045 \pm 0.056$
1.310	$-0.027 \pm 0.029$	$+0.135 \pm 0.037$	$-0.052 \pm 0.045$	$+0.063 \pm 0.042$
1.50	$+0.043 \pm 0.035$	$+0.000 \pm 0.047$	$-0.079 \pm 0.057$	$-0.019 \pm 0.052$
1.66	$-0.031 \pm 0.065$	$-0.236 \pm 0.085$	$+0.060 \pm 0.100$	$+0.051 \pm 0.096$

The angular distributions of the neutrons at a series of energies are shown in Fig. 7, and the fitted coefficients are listed in Table IV. A distribution was

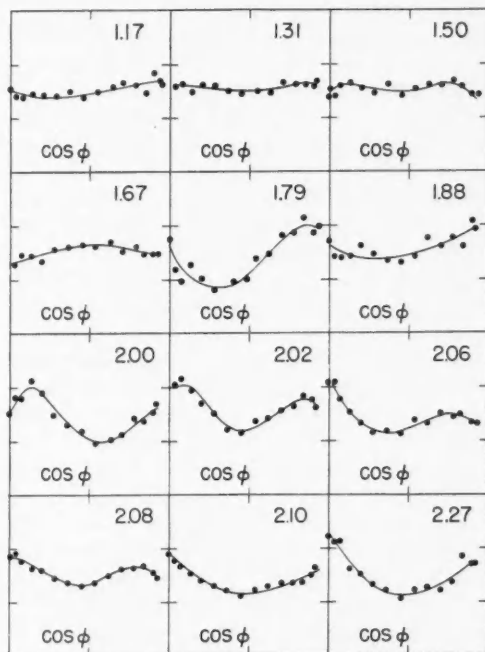


FIG. 7. Angular distributions of the neutrons from the  $C^{14}(p, n)N^{14}$  reaction at various proton energies. The relative intensities are plotted as a function of the cosine of the center of mass angle (from  $+1.0$  to  $-1.0$ ). The numbers on the curves refer to the proton energy in Mev. The ordinate scales in different graphs are not related.

taken at each resonance and, in addition, other distributions between the resonances were taken for reasons to be discussed below.

The angular distribution of the ground state  $\gamma$ -ray at the resonances at 0.646 and 0.537 Mev. is inconsistent with  $J = 1/2^\pm$  or  $5/2^+$  for these states.

TABLE IV  
NEUTRON ANGULAR DISTRIBUTIONS: FITTED CURVES  
 $W(\theta) = a_0P_0 + a_1P_1 + a_2P_2 + a_3P_3 + a_4P_4$

$E_p$	$a_1/a_0$	$a_2/a_0$	$a_3/a_0$	$a_4/a_0$
1.165 <sup>a</sup>	-0.092±0.026	+0.047±0.035	+0.022±0.043	+0.020±0.048
1.31 <sup>a</sup>	-0.016±0.017	+0.057±0.024	+0.010±0.032	-0.042±0.033
1.50 <sup>a</sup>	+0.022±0.022	-0.053±0.030	+0.083±0.039	-0.121±0.041
1.66 <sup>a</sup>	-0.043±0.022	-0.121±0.032	+0.009±0.041	+0.032±0.049
1.79 <sup>a</sup>	-0.408±0.056	+0.239±0.076	+0.350±0.103	-0.065±0.106
1.88 <sup>a</sup>	-0.166±0.049	+0.172±0.066	-0.004±0.090	+0.039±0.092
2.00	+0.184±0.031	+0.370±0.042	-0.196±0.057	-0.291±0.058
2.02 <sup>a</sup>	+0.096±0.024	+0.269±0.032	+0.166±0.044	-0.279±0.045
2.04	+0.113±0.025	+0.192±0.034	+0.325±0.047	-0.073±0.048
2.08 <sup>a</sup>	+0.075±0.012	+0.115±0.017	+0.200±0.023	-0.149±0.023
2.10	+0.026±0.015	+0.284±0.020	+0.029±0.027	+0.029±0.028
2.27 <sup>a</sup>	+0.065±0.040	+0.454±0.054	+0.081±0.074	-0.054±0.075

<sup>a</sup>These angular distributions were taken at the peaks of observed resonances. The remainder were taken at intermediate energies.

For  $J = 3/2+$  the theoretical distribution (assuming pure  $E1$  radiation\*) is  $P_0 - 0.5P_2$ , which is somewhat outside the quoted errors for both resonances. If  $J = 3/2-$ , mixed  $M1$  and  $E2$  radiation to the ground state is possible, and the observed distribution can be fitted with a suitable multipole ratio and phase difference. Agreement with the observed distributions is obtained with the intensity ratio  $I_{E2}/I_{M1} = 0.003$  ( $180^\circ$  out of phase) or 3.8 (in phase) for the 0.646 Mev. resonance, and  $I_{E2}/I_{M1} = 0.005$  (in phase) or 2.2 (in phase) for the 0.537 Mev. resonance. The expected ratio for this energy from the Weisskopf formulae is about 0.02, so that it is likely that the first-mentioned interpretation is correct for each resonance.

The interference in the total yield of  $\gamma_0$  observed near the 1.31 Mev. resonance indicates that this resonance and the broad resonance at 1.50 Mev. with which it is interfering must have the same spin and parity. The  $\gamma$ -ray angular distributions below 1.6 Mev. are all essentially isotropic except at the 1.165 Mev. resonance, where a  $\cos \theta$  term is present. This limits the possible assignments for the three states to  $1/2^\pm$  or  $3/2-$ , subject to the condition that the 1.165 Mev. state must have opposite parity to the broad state. The  $N^{14}(n, n)$  yield curve of Hinchey *et al.* (7) near the 1.31 Mev. resonance shows the characteristic  $s$ -wave interference with the potential scattering and, with their cross section measurement, establishes this as  $1/2+$ . Hence the wide state at 1.50 Mev. must also be  $1/2+$ , and the state at 1.165 Mev. may be  $1/2-$  or  $3/2-$ . (From the  $\sigma_{nn}$  for this latter resonance it is probably  $1/2-$ .) The  $\gamma_0$  distribution at 1.66 Mev. suggests  $J = 3/2$  for this resonance in agreement with the value in Table II. The absence of appreciable odd term interference with the broad resonance at 1.50 Mev. indicates that the 1.66 Mev. resonance has positive parity. It should be remarked that the observed negative coefficient of  $P_2$  in this distribution is only one half the value expected for this assignment, and this may be a result of two effects, (a) an isotropic

\*The  $M2/E1$  ratio is expected to be about  $10^{-6}$ .

background from the 1.50 Mev. state at this energy, and (b) interference between two states of the same parity ( $3/2+$  and  $1/2+$ ), which would appreciably change the  $P_2$  term.

Turning now to the neutron distributions of Table IV, the essentially isotropic distributions at the 1.165, 1.31, and 1.50 Mev. resonances are consistent with the interpretations of the  $\gamma$ -ray results. At the 1.66 Mev. resonance, the distribution favors  $J = 3/2$  in agreement with the  $\sigma_{nn}$  results, and the absence of odd interference terms is further evidence favoring positive parity. It is clear from the yield curve that two or more levels are interfering with the level at 1.79 Mev. The large odd interference terms indicate that one at least of these has opposite parity to the 1.79 Mev. state. Assuming that the states at 1.50, 1.66, and 2.08 Mev. are the main interfering states, and that these have been correctly assigned positive parity, then the 1.79 Mev. resonance will have negative parity. The ratio of the  $P_3$  to  $P_1$  coefficients gives slight weight to a  $5/2-$  assignment, but  $3/2-$  cannot be excluded. The size of  $\sigma_{nn}$  for this resonance also does not serve to distinguish between the two  $J$  values. The resonance at 1.88 Mev. is also interfering with several resonances of both parities, and little definite information can be derived from the  $(p, n)$  angular distribution. It is quite consistent with  $J = 1/2-$  indicated by the magnitude of the  $\sigma_{nn}$  cross section and the absence of  $s$ -wave interference in the  $(n, n)$  scattering (7, 11). At the 2.02 Mev. resonance the observation of a  $P_4$  term which disappears at the higher resonance at 2.08 Mev. supports the  $J$  value of  $5/2$  given in Table II. Moreover, the relative magnitudes of the coefficients of  $P_4$  and  $P_2$  exclude an assignment of  $5/2+$ . Just above the resonance at 2.08 Mev. a fairly pure  $P_0 + aP_2$  distribution is observed. This indicates the assignment  $J = 3/2$  for the 2.08 Mev. resonance,  $5/2$  being excluded by the small  $P_2$  coefficient and the absence of a  $P_4$  coefficient. Further information about the parities of these two states can be deduced from the value of the ratio of the coefficient of  $P_3$  to that of  $P_1$  between the two resonances. We assume that the channel spin mixture is that derived from the coefficients of even Legendre polynomials at each resonance, and that the relative amplitudes and phases of interfering neutron orbitals are those computed from the usual Coulomb functions. Assignments of  $5/2+$ ,  $3/2-$  would predict a ratio  $a_3/a_1$  of either  $-7$  or  $-0.7$ , while the  $5/2-$ ,  $3/2+$  assignment would predict a ratio of either  $+2$  or  $+0.5$ . The observed ratio of the coefficient of  $P_3$  to that of  $P_1$  is  $+2.6 \pm 0.7$ , which again strongly favors  $5/2-$  for the 2.02 Mev. state and  $3/2+$  for the 2.08 Mev. state. The  $\sigma_{nn}$  cross section values for those resonances are consistent with  $J = 5/2$  for the lower resonance and  $J = 3/2$  or  $5/2$  for the upper resonance (Table II). The resonance at 2.27 Mev. shows very small odd interference terms, indicating that it has the same parity as the 2.08 Mev. resonance. The angular distribution is consistent with  $J = 3/2$  or  $5/2$ . The  $\sigma_{nn}$  cross section clearly indicates  $J = 5/2$ .

Fowler *et al.* (6) have recently measured the angular distribution of elastically scattered neutrons from the  $N^{14}(n, n)$  reaction for some of these reso-

nances. For the resonance corresponding to  $E_p = 1.79$  Mev. they assign  $3/2^-$ . For the resonances corresponding to proton energies of 2.08 and 2.27 Mev. they assign parities opposite to those obtained in the present work. The two experiments are in agreement in assigning the same parity to both states. Our assignment of positive parity to the 2.08 Mev. state is based, as stated above, on the interference with the state at 2.02 Mev. and also on the absence of appreciable odd interference at energies around 1.6 to 1.7 Mev. where the background is made up of about equal parts of the broad 1.5 Mev. state and the 2.08 Mev. state. The conclusions from the  $(n, n)$  work are based on the assumption that neighboring states do not interfere, which may be unjustified.

#### PARTIAL WIDTHS

The observed partial widths for proton emission, neutron emission, and ground state  $\gamma$ -radiation are listed in Columns 4, 5, and 6 of Table V, for those

TABLE V  
REDUCED WIDTHS AND  $\gamma$ -RAY TRANSITION PROBABILITIES

1 $E_p$ , Mev.	2 Excitation in $N^{15}$ , Mev.	3 $\Gamma$ , kev.	4 $\Gamma_n$ , kev.	5 $\Gamma_p$ , kev.	6 $\Gamma_\gamma(\gamma_0)$ , ev.	7 $J\pi$	8 $T$	9 $I_n$	10 $\theta_n^2$	11 $I_p$	12 $\theta_p^2$	13 $L(\gamma_0)$	14 $\Delta(\gamma_0)$
0.537	10.70				0.12	3/2-	1/2			1		M1	0.005
0.646	10.81				0.010	3/2-	1/2			1		M1	0.0005
1.165	11.29	12	1.6	10.4	0.29	1/2-	1/2	1	0.002	1	0.04	M1	0.5
1.31	11.43	41	32.8	8.2	2.15	1/2+	1/2	0	0.01	0	0.007	E1	0.10
1.50	11.61	475	5.0	470	26.3	1/2+	3/2	0	0.001	0	1.0	E1	0.19
1.66	11.77	37	36.5	0.5		3/2+	1/2	0	0.01	2	0.004		
1.79	11.88	24.5	24.5	0.03		5/2-	1/2	1	0.01	3	0.003		
1.88	11.96	21.5	21.2	0.3		1/2-	1/2	1	0.009	1	0.0004		
2.02	12.09	18	17.2	0.8		5/2-	1/2	1	0.007	3	0.05		
2.08	12.14	53	38.0	15.0		3/2+	1/2	0	0.008	2	0.06		
2.27	12.32	22	21.7	0.3		5/2+	1/2	2	0.007	2	0.0009		

Columns 3-6 list experimental partial widths; Columns 7, 8, 9, 11, and 13 list values of spin, isotopic spin, and orbital angular momenta assumed for the calculation of reduced widths; and Columns 10, 12, and 14 list the dimensionless reduced particle widths and the ratio of observed to theoretical radiation widths.

resonances for which they could be derived. In Columns 10 and 12 are listed the ratios,  $\theta^2$ , of the reduced particle widths to  $(\hbar^2/Ma^2)(T_p I T_p M_i | T M_T)^2$ , which is expected to be close to the theoretical single particle reduced width (14). The interaction radius,  $a$ , used was  $4.85 \times 10^{-13}$  cm. The Clebsch-Gordon coefficient involving the isotopic spins of the parent state,  $T_p$ , of the emitted particle,  $I$ , and of the compound state,  $T_i$  is introduced, since a definite type of particle, proton or neutron, is being distinguished. The reduced particle width,  $\gamma^2$ , is defined as  $\gamma^2 = (\Gamma_x/2ka)(F_l^2 + G_l^2)$  where  $\Gamma_x$  is the observed partial width,  $k$  is the wave number of the particle, and  $F_l$  and  $G_l$  are the usual Coulomb functions. Thomas (26) has pointed out that, for reduced widths which are a large fraction of the single particle reduced width, a further correction must be made which depends on the energy derivative of the wave function at the nuclear surface. This correction has been applied only to the resonance at 1.50 Mev. using formulae quoted by Lane (14).

In Column 14 is listed  $A$ , the ratio of the observed partial width for ground state radiation to the width calculated using the model of Lane and Radicati (15) for a three particle system in  $j$ - $j$  coupling. It has been assumed in both this and the reduced width calculation that in the initial state there is one particle in a shell different from that occupied by the other two. In particular, the following configurations have been assumed for  $s$ ,  $p$ ,  $d$ , and  $f$  states respectively:  $(1p_{1/2})^2 2s_J$ ,  $(1p_{1/2})^2 2p_J$ ,  $(1p_{1/2})^2 1d_J$ , and  $(1p_{1/2})^2 1f_J$ , where  $J$  is the total spin of the state. The isotopic spin assumed for each state is also indicated in Table V, Column 8. The ground state of  $N^{16}$  has been assumed to have a configuration  $(1p_{1/2})^3$ .

#### DISCUSSION

For the 1.50 Mev. state the neutron reduced width is only 1/1000 of the proton reduced width, which has the full single particle value. One possible reason for this is that the state has isotopic spin 3/2. Below a proton energy of 3 Mev. the neutrons can only lead to the ground state of  $N^{14}$ , which has  $T = 0$ . A compound state of  $T = 3/2$  accordingly cannot break up into  $N^{14}$  and a neutron, except via admixture of  $T = 1$  states into the ground state of the  $N^{14}$  parent.

The  $C^{15}-N^{15}$  mass difference is  $8.64 \pm 0.1$  Mev. (1). Coulomb energy correction would put the analogue of the ground state of  $C^{15}$  at an excitation in  $N^{15}$  of  $10.7 \pm 0.1$  Mev. This corresponds to a proton bombarding energy of  $0.54 \pm 0.1$  Mev. The two lowest states of  $C^{15}$  would be expected, from analogy with  $O^{17}$  and  $F^{17}$ , to be  $d_{5/2}$  and  $s_{1/2}$ , with the  $s_{1/2}$  state about 0.75 Mev. above the  $d_{5/2}$  state. Thus it is quite possible that the  $s_{1/2}$  state at  $E_p = 1.50$  Mev. has  $T = 3/2$  and is the analogue of the first excited (or at least a low lying) state of  $C^{15}$ . The size of the neutron reduced width would imply an admixture of at least 3% in amplitude of  $T = 1/2$  configuration.

The other state of particular interest is that at 1.165 Mev., where the radiation width is 50% of the theoretical width. The reduced proton width is only 4% of the single particle value. However, the neutron reduced width is about 0.2% of the single particle width, which again implies that this may be a fairly pure single particle proton state. It is not clear why the proton width is so small if this is the case. It may be that where considerable configuration mixing occurs, the particle widths may combine out of phase where the radiation transition probabilities do not.

For most of the other states the particle reduced widths are very small, which may be due to configurations in which more than one particle is in a higher configuration than the  $(1p)$  shell. A similar interpretation can be given for the two states below the neutron threshold which have small radiation widths.

#### THE THERMAL NEUTRON CROSS SECTION IN $N^{14}$

It is interesting to consider which of the resonances under discussion are responsible for the thermal neutron capture and reaction cross sections in  $N^{14}$ . Only  $s$ -wave neutron states ( $J = 1/2+$  or  $3/2+$ ) can participate, and reference to Table V shows that the resonances at  $E_p = 0.646$  and  $0.537$

Mev., below the neutron binding energy, which have negative parity, cannot contribute. While the states at 1.31 and 1.66 Mev. are too narrow to contribute appreciably, the same is not true of the wide state at  $E_p = 1.50$  Mev. These remarks would appear to be corroborated by the comparison of the neutron and proton capture  $\gamma$ -ray spectra. In Fig. 8 are shown the  $C^{14}(p, \gamma)N^{15}$

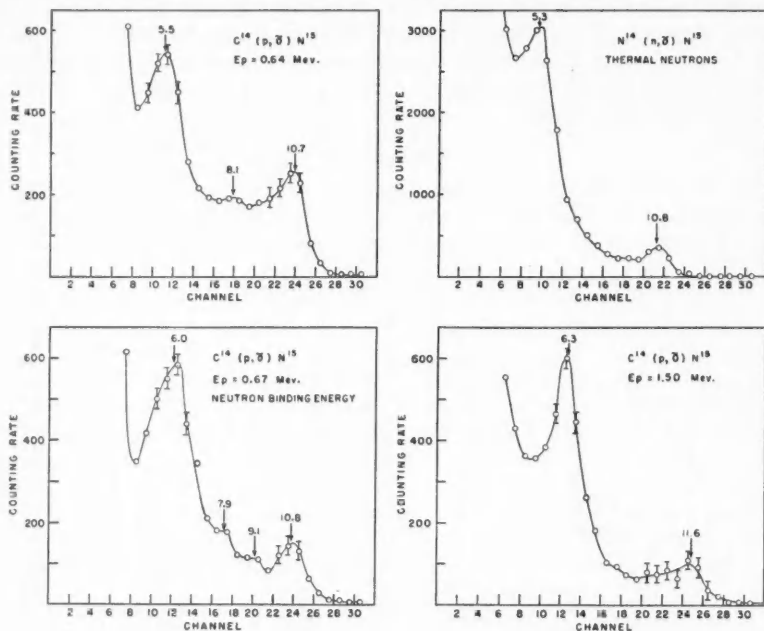


FIG. 8. Comparison of the  $C^{14}(p, \gamma)N^{15}$   $\gamma$ -ray spectra at the 0.646 Mev. resonance, at the neutron threshold at 0.67 Mev., and at the 1.50 Mev. resonance and the  $N^{14}(n, \gamma)N^{15}$  spectrum. The errors shown are statistical errors. The ordinate scale is in arbitrary units.

capture spectra at the 0.646 Mev. resonance, at the neutron threshold ( $E_p = 0.67$  Mev.), at the 1.50 Mev. resonance, and finally the  $N^{14}(n, \gamma)N^{15}$  thermal capture spectrum. All were recorded on the same 2-in. scintillation spectrometer, using for the last spectrum the N.R.X. reactor as a neutron source. The proton capture spectrum from the 1.50 Mev. state resembles the neutron capture spectrum, while the proton capture spectrum at the neutron threshold does not, but shows the influence of the nearby  $p$ -state at 0.646 Mev.

The thermal neutron capture cross sections derived from the 1.50 Mev. resonance have been computed using the level constants listed in Table V. The computed thermal  $N^{14}(n, p)C^{14}$  cross section is 1.9 barns in good agreement with the experimental value of 1.7 barns (12). However, the computed thermal  $N^{14}(n, \gamma)N^{15}$  cross section for the ground state transition is 0.4 mb.,



while the experimental value is 13 mb.\* This discrepancy of a factor of 30 seems definitely outside any possible errors in either measurement, and therefore other levels must contribute the greater part of the thermal neutron radiative cross section. The evidence of the capture  $\gamma$ -ray spectra discussed above is not inconsistent with this conclusion, since similar spectra might be expected if the level mainly responsible for the  $(n, \gamma)$  cross section and the 1.50 Mev. level had the same spin.

It has been pointed out (17) that the large neutron scattering cross section at thermal energies (9) may be produced by a resonance of negative energy, and the shape of the neutron scattering cross section curve at higher energies (7, 11) also calls for this interpretation. If the same resonance is responsible for the large radiative cross section at thermal energies, this resonance must have a very small proton width since the  $(n, p)$  cross section is already fully accounted for by the 1.50 Mev. state. From the present observations it would seem probable that the resonance at negative neutron energy also has  $J = 1/2+$  and a large radiative width. Thus it may be another single particle  $s$ -state with the  $N^{14}+n$  configuration.

If we assume that a single level below the neutron threshold is responsible for the large neutron radiative capture and scattering cross sections, we deduce from the magnitudes of the scattering cross sections that this level is in the region 10.2 to 10.7 Mev. Three levels are known in this region at 10.458, 10.544, and 10.705 Mev. (Table I), and for the sake of thoroughness we shall also consider the nearest neighbors at 10.06 and 10.81 Mev. (22). The 10.705 and 10.81 Mev. levels have already been ruled out because of their negative parity. From the yield of the ground state  $\gamma$ -ray at the 10.544 Mev. level ( $E_p = 0.361$  Mev., Table II), we obtain an upper limit for  $\Gamma_\gamma$  of only 0.004 ev. Since, moreover, the spectrum at this energy (Fig. 4) contains a strong  $\gamma$ -ray at 7.1 Mev. which is not detected in the  $N^{14}(n, \gamma)N^{15}$  spectrum, it seems unlikely that this level can account for the thermal neutron cross sections. We therefore conclude that the 10.458 Mev. level, or possibly that at 10.06 Mev., is the one required. (The failure to detect the 10.458 Mev. state in the  $(p, \gamma)$  yield curve, Fig. 3, is consistent with the requirement of small proton width for the state responsible for the neutron scattering cross section. On the other hand, if the 10.458 Mev. state has a high spin, the low cross section might be accounted for by the barrier for incoming waves of high orbital momenta.) If either of the levels at 10.458 or 10.06 Mev. is assumed to be the one required we may deduce from the neutron cross section data that it must have a dimensionless neutron reduced width,  $\theta_n^2$ , of approximately unity, and a partial width for the ground state  $\gamma$ -ray of about one volt. We note that such a level is expected at this energy from a comparison with the level in the mirror nucleus  $O^{16}$  at 9.8 Mev. (5), which has  $J = 1/2+$  or  $3/2+$ , a total radiation width,  $\omega\Gamma_\gamma$ , of 46 ev., and a proton width of 1.25 Mev. (corresponding to a

\*The reported upper limit for the total radiative cross section (13) obtained from a comparison of the nitrogen and beryllium neutron capture  $\gamma$ -ray spectra is 160 mb. A revised estimate based on a more complete knowledge of the  $Be^{10}$  capture  $\gamma$ -ray decay scheme (3) gives 110 mb. for the total radiative cross section and 13 mb. for the cross section for  $\gamma_0$ .

dimensionless reduced width  $\theta_p^2 = 0.4$ ). These level constants suggest a  $N^{14} + p$  configuration for the  $O^{15}$  state.

#### ACKNOWLEDGMENTS

We take pleasure in thanking Dr. L. G. Elliott, Mr. W. T. Sharp, Dr. J. M. Kennedy, and Dr. A. M. Lane for helpful discussions in connection with this work. The analysis of the angular distributions on the FERUT computer was arranged by Dr. H. Gellman. We are grateful to Mr. R. Shuttleworth, Mr. H. Smythe, and their staff for their efficient operation of the accelerator.

#### REFERENCES

1. AJZENBERG, F. and LAURITSEN, T. *Revs. Mod. Phys.* **27**: 77. 1955.
2. BARTHOLOMEW, G. A., BROWN, F., GOVE, H. E., LITHERLAND, A. E., and PAUL, E. B. *Phys. Rev.* **96**: 1154. 1954.
3. BARTHOLOMEW, G. A. and KINSEY, B. B. *Can. J. Phys.* **31**: 49. 1953.
4. BOLLMAN, W. and ZÜNTI, W. *Helv. Phys. Acta*, **24**: 517. 1951.
5. DUNCAN, D. B. and PERRY, J. E. *Phys. Rev.* **82**: 809. 1951.
6. FOWLER, J. L., JOHNSON, C. H., and RISSER, J. R. *Phys. Rev.* **91**: 441A. 1953.  
FOWLER, J. L. and JOHNSON, C. H. *Phys. Rev.* **98**: 728. 1955.
7. HINCHEY, J. J., STELSON, P. H., and PRESTON, W. M. *Phys. Rev.* **86**: 483. 1952.
8. HORNYAK, W. F., LAURITSEN, T., MORRISON, P., and FOWLER, W. A. *Revs. Mod. Phys.* **22**: 291. 1950.
9. HUGHES, D. J. *et al.* U.S. Atomic Energy Comm. Rept. No. AECU 2040. 1952.
10. JOHNSON, C. H. and BARSCHALL, H. H. *Phys. Rev.* **80**: 818. 1950.
11. JOHNSON, C. H., PETREE, B., and ADAIR, R. K. *Phys. Rev.* **84**: 775. 1951.
12. KAY, R., MARK, H., and GOODMAN, C. *Phys. Rev.* **91**: 472A. 1953.
13. KINSEY, B. B., BARTHOLOMEW, G. A., and WALKER, W. H. *Can. J. Phys.* **29**: 1. 1951.
14. LANE, A. M. Atomic Energy Research Establishment Rept. No. T/R 1289. 1954.
15. LANE, A. M. and RADICATI, L. A. *Proc. Phys. Soc. (London)*, **A**, **67**: 167. 1954.
16. MEIER, R., RICAMO, R., SCHERRER, P., and ZÜNTI, W. *Helv. Phys. Acta*, **26**: 451. 1953.  
HUBER, P. and STRIEBEL, H. R. *Helv. Phys. Acta*, **25**: 157A. 1954.  
SPEISER, D. and FIERZ, M. *Helv. Phys. Acta*, **25**: 159A. 1954.
17. MELKONIAN, E. *Phys. Rev.* **76**: 1744. 1949.
18. RICAMO, R. and ZÜNTI, W. *Helv. Phys. Acta*, **24**: 302. 1951.
19. ROSE, M. E. *Phys. Rev.* **91**: 610. 1953.
20. ROSEBOROUGH, W. D., McCUE, J. J., PRESTON, W. M., and GOODMAN, C. *Phys. Rev.* **83**: 1133. 1951.
21. SHOUPP, W. E., JENNINGS, B., and SUN, K. H. *Phys. Rev.* **75**: 1. 1949.
22. SPEARMAN, K. R., HUDSPETH, E. L., and MORGAN, I. L. *Phys. Rev.* **94**: 806A. 1954;  
and private communication from I. L. Morgan.
23. SPERDUTO, A., BUECHNER, W. W., BOCKELMAN, C. K., and BROWNE, C. P. *Phys. Rev.* **96**: 1316. 1954.
24. STEBLER, A. and HUBER, P. *Helv. Phys. Acta*, **21**: 59. 1948.
25. STETTER, W. and BOTHE, W. *Z. Naturforsch.* **6a**: 61. 1951.
26. THOMAS, R. G. *Phys. Rev.* **81**: 148. 1951.
27. TRUMBLE, R. E. *Phys. Rev.* **94**: 748A. 1954.
28. VON GIERKE, G. *Z. Naturforsch.* **8a**: 567. 1953.

# THE THERMAL NEUTRON CAPTURE CROSS SECTION OF $\text{Au}^{198}$ AND THE HALF-LIFE OF $\text{Au}^{199}$ <sup>1</sup>

By R. E. BELL,<sup>2</sup> R. L. GRAHAM, AND L. YAFFE<sup>3</sup>

## ABSTRACT

The thermal neutron capture cross section of radioactive  $\text{Au}^{198}$  has been measured by the activation method as  $26,000 \pm 1200$  barns, assuming 99 barns for the thermal neutron cross section of  $\text{Au}^{197}$ . Metallic  $\text{Au}^{197}$  was bombarded in fluxes up to  $9 \times 10^{18}$  thermal neutrons  $\text{cm}^{-2} \text{sec}^{-1}$  to produce a mixture of  $\text{Au}^{198}$  and  $\text{Au}^{199}$  by the successive neutron capture reactions  $\text{Au}^{197}(n, \gamma)\text{Au}^{198}(n, \gamma)\text{Au}^{199}$ . The ratio of the  $\text{Au}^{199}$  activity to  $\text{Au}^{198}$  activity so produced yields  $\sigma_c(\text{Au}^{197})$ . In a preliminary experiment, the half-life of  $\text{Au}^{199}$  was measured as  $3.148 \pm 0.010$  days.

## I. INTRODUCTION

Several measurements have been made of the thermal neutron capture cross section of radioactive  $\text{Au}^{198}$ , using the activation method and the successive neutron capture reactions  $\text{Au}^{197}(n, \gamma)\text{Au}^{198}(n, \gamma)\text{Au}^{199}$ . Neutron capture in  $\text{Au}^{198}$  was first postulated by Hill and Mihelich (12) to explain the appearance, in the  $\beta$ -ray spectrum of neutron-irradiated gold, of faint conversion lines characteristic of  $\text{Au}^{199}$ , in addition to the  $\beta$ -ray spectrum of  $\text{Au}^{198}$ . From the measured intensity of the  $K$  conversion line of the 158  $\gamma$ -ray transition following  $\text{Au}^{199}$  decay relative to the intensity of the  $K$  conversion line of the 411.6-keV  $\gamma$ -ray accompanying the decay of  $\text{Au}^{198}$ , Hill and co-workers were able to estimate the thermal neutron capture cross section of  $\text{Au}^{198}$ . This estimate unfortunately depends upon the details of the disintegration scheme of  $\text{Au}^{199}$ , with the result that three different values for the cross section have been quoted as knowledge of the  $\text{Au}^{199}$  disintegration scheme has progressed (12, 11, 18). Other estimates for this cross section have since been reported (9, 1) which differ widely from those of Hill and his co-workers. The present experiments reduce the uncertainties by using neutron fluxes of up to 80 times that used by Hill *et alii*; since the ratio of activities  $\text{Au}^{199}/\text{Au}^{198}$  is nearly proportional to the neutron flux, the observed effects become very large, and the relative intensity  $\text{Au}^{199}/\text{Au}^{198}$  can be measured by methods not depending critically on knowledge of the disintegration scheme of  $\text{Au}^{199}$ . The fact that, as shown later, the large effects anticipated were observed is a verification of the successive neutron capture mechanism proposed by Hill and Mihelich (12).

The capture cross section of  $\text{Au}^{198}$  is obtained by measuring the ratio of  $\text{Au}^{199}$  activity to  $\text{Au}^{198}$  activity in samples of metallic gold irradiated under known conditions, and calculating the desired cross section in terms of the known thermal neutron capture cross section of  $\text{Au}^{197}$ . Since the half-lives of both  $\text{Au}^{198}$  and  $\text{Au}^{199}$  enter the calculations, the half-life of  $\text{Au}^{199}$  (hitherto

<sup>1</sup>Manuscript received May 3, 1955.

Contribution from Physics and Chemistry Divisions, Atomic Energy of Canada Limited, Chalk River, Ontario. Issued as A.E.C.L. No. 183.

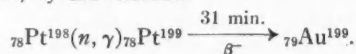
<sup>2</sup>Present address: Radiation Laboratory, McGill University, Montreal, Quebec.

<sup>3</sup>Present address: Department of Chemistry, McGill University, Montreal, Quebec.

known only roughly) was measured to the same accuracy as that of the well-known half-life of  $\text{Au}^{198}$  (5). This value for the  $\text{Au}^{199}$  half-life was privately circulated and is reported by Hollander *et al.* (13).

## II. HALF-LIFE OF $\text{Au}^{199}$

A source of  $\text{Au}^{199}$  was made by irradiating platinum in the Chalk River NRX nuclear reactor, by the reaction



In this manner  $\text{Au}^{199}$  may be prepared free from  $\text{Au}^{198}$ , unless the platinum used for irradiation contains appreciable quantities of gold as an impurity. The platinum used in this work contained less than one part per million of gold, as shown by spectrographic analysis.

Gold was separated from the irradiated platinum by the following chemical procedure. The platinum was allowed to stand for 10 hr. after irradiation to allow the 31 min.  $\text{Pt}^{199}$  to decay to  $\text{Au}^{199}$ . The platinum sample was then dissolved in aqua regia with 0.5 mgm. gold as carrier. The solution was made 4 *M* with respect to hydrochloric acid, and the gold extracted with an equal volume of ethyl acetate.

An aliquot of this source was deposited on a 1/16-in. aluminum plate, evaporated to dryness, and covered with a coat of plastic varnish. The decay of this source was followed with a quartz fiber air electroscopically previously checked for linearity and stability (17). Readings were taken every day or two for 20 half-lives of the source, during which the activity decayed from  $10^5$  times background to the background level. Small corrections were made to the individual readings for temperature and barometric pressure (17). Between measurements the  $\text{Au}^{199}$  source was stored in a closely fitting glass vessel. Periodic examination of the inside surfaces with a Geiger counter proved that activity was not escaping from the source. Examination of a similarly prepared source in the  $\beta$ -ray spectrometer (see Section III) showed no radiations other than those of  $\text{Au}^{199}$ . The decay curve found is not shown in a diagram, since a line through the 23 experimental points for the first 13 half-lives (decay factor  $10^4$ )—i.e. those whose value is greater than 10 times background—is indistinguishable from a straight line on a semilogarithmic plot. The r.m.s. deviation from the straight line fitted to the points by the method of least squares is 0.6%. The slope of the fitted line gave a value for the half-life of  $\text{Au}^{199}$  of  $3.1476 \pm 0.0008$  days, the indicated standard deviation arising only from the internal consistency of the points. To make allowance for any possible systematic error, we give

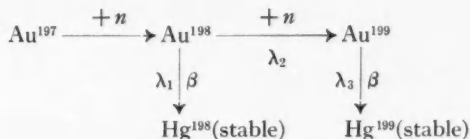
$$T_{1/2}(\text{Au}^{199}) = 3.148 \pm 0.010 \text{ days.}$$

This value is not in disagreement with previously measured approximate values of 3.3 days (16) and 3.2 days (7).

## III. NEUTRON CAPTURE CROSS SECTION OF $\text{Au}^{198}$

### (a) Method

If a sample of  $A$  atoms of  $\text{Au}^{197}$  is irradiated in a thermal neutron flux  $F$  neutrons  $\text{cm}^{-2} \text{sec}^{-1}$ ,  $B(t)$  atoms of  $\text{Au}^{198}$  and  $C(t)$  atoms of  $\text{Au}^{199}$  are produced after a period of  $t$  sec. according to the reaction:



The decay constants for  $\beta$  decay of  $\text{Au}^{198}$  and  $\text{Au}^{199}$  are  $\lambda_1 \text{ sec.}^{-1}$  and  $\lambda_3 \text{ sec.}^{-1}$  respectively, and the neutron capture probability for  $\text{Au}^{198}$  atoms is  $F\sigma(\text{Au}^{198}) = \lambda_2 \text{ sec.}^{-1}$ . Neglecting the destruction of  $\text{Au}^{197}$  atoms ( $<2\%$  in these experiments) the equations for growth and decay during a period of  $t \text{ sec.}$  at constant neutron flux are

$$[1] \quad B(t) = B(\infty) \left[ 1 - \left\{ 1 - \frac{B(0)}{B(\infty)} \right\} e^{-(\lambda_1 + \lambda_2)t} \right],$$

$$[2] \quad C(t) = \frac{\lambda_2 B(\infty)}{\lambda_3} [1 - e^{-\lambda_3 t}] + \left\{ 1 - \frac{B(0)}{B(\infty)} \right\} \frac{\lambda_2 B(\infty)}{\lambda_1 + \lambda_2 - \lambda_3} [e^{-(\lambda_1 + \lambda_2)t} - e^{-\lambda_3 t}] + C(0)e^{-\lambda_3 t}.$$

Here  $B(0)$  and  $C(0)$  are the number of atoms of  $\text{Au}^{198}$  and  $\text{Au}^{199}$  present at the beginning of the period, and the saturation value of the number of  $\text{Au}^{198}$  atoms is

$$[3] \quad B(\infty) = (\lambda_1 + \lambda_2)^{-1} A F \sigma_{\text{eff}}(\text{Au}^{197}).$$

The effective capture cross section for  $\text{Au}^{197}$  is here taken to be the thermal cross section times a factor  $R$  which corrects for the experimentally determined resonance activation. In the above equations  $\lambda_2 = F\sigma(\text{Au}^{198})$  is the only unknown, being the product of two unknown quantities. This quantity is proportional to the pile flux and hence, in any one irradiation, to the pile power.

An experiment to measure  $\sigma(\text{Au}^{198})$  consists of a measurement of  $\lambda_1 B$ , the  $\text{Au}^{198}$  activity induced in the sample, and of  $\lambda_3 C / \lambda_1 B$ , the ratio of  $\text{Au}^{199}$  to  $\text{Au}^{198}$  activity in the same sample. These two experimental quantities are used together with equations [1], [2], and [3] to solve for the two unknowns  $\sigma(\text{Au}^{198})$  and  $F$  as follows. For a given pile power, a series of values for  $\lambda_2 = F\sigma(\text{Au}^{198})$  is assumed, and for each of these a ratio  $\lambda_3 C / \lambda_1 B$  is computed from the record of pile power during the irradiation, using equations [1] and [2]. Graphical interpolation to the measured value of  $\lambda_3 C / \lambda_1 B$  then yields the actual value of  $\lambda_2$ . The measured value of  $\lambda_1 B$  then gives  $F$  directly from equations [1] and [3],  $\lambda_2$  now being known. Finally,  $\sigma(\text{Au}^{198})$  is given by  $\lambda_2 / F$ . The graphical procedure does not introduce any appreciable error in the results.

The contribution due to the pronounced resonance at 4.9 ev. in  $\text{Au}^{197}$  was determined experimentally by irradiating at the same time and in the same irradiation assembly as the main sample Au foils of identical surface density in a small cadmium pouch made from 0.015-in. cadmium. This cadmium pouch was so placed that its effect on the thermal flux at the unshielded Au foil was less than one per cent. The rate of production of  $\text{Au}^{198}$  atoms is for convenience here defined as  $R \times F\sigma(\text{Au}^{197})$  where  $F$  and  $\sigma$  are the thermal

flux and cross section and the factor  $R$  makes allowance for the resonance activation. Actually we distinguish here only between epi-cadmium and cadmium absorbed neutrons, and hence the factor is here taken as

$$[4] \quad R = \int_0^{\infty} \sigma(\text{Au}^{197}) F(\epsilon) d\epsilon / \int_0^{0.5\text{ev.}} \sigma(\text{Au}^{197}) F(\epsilon) d\epsilon,$$

where  $F(\epsilon)d\epsilon$  is the neutron flux in the energy interval  $\epsilon$  to  $\epsilon+d\epsilon$ , and 0.5 ev. is the cutoff for 0.015-in. cadmium foil. This factor is then equal to (unshielded  $\text{Au}^{198}$  activity)/(unshielded—shielded) after corrections for foil weights and  $\text{Au}^{198}$  burnout using equations [1] and [3], and using  $\lambda_2 = 0$  (verified later) for the shielded foil. The  $1/v$  portion of the thermal neutron cross section of  $\text{Au}^{197}$  has been measured as  $97.8 \pm 0.5$  barns by Carter *et al.* (6) and  $97.4 \pm 0.9$  barns by Egelstaff (8). To this must be added a correction of 1.5% to allow for the tail of the 4.9 ev. resonance (non- $1/v$  part) integrated over the thermal (20°C.) portion of the pile neutron spectrum.\* We use here a value of 99 barns for the thermal capture cross section, and hence  $99 \times R$  barns as the effective thermal neutron capture cross section for  $\text{Au}^{197}$ . The capture cross section for  $\text{Au}^{198}$  is thus  $\lambda_2/F$  and is measured in terms of the thermal neutron capture cross section of the  $\text{Au}^{197}$  atoms in the same sample.

#### (b) Experiments

Before examining mixed sources of  $\text{Au}^{198}$  and  $\text{Au}^{199}$  made by the successive neutron capture process, a sample of  $\text{Au}^{199}$  was examined as a comparison source. The sample was prepared as described in the previous section, and deposited on 1.5-mgm./cm.<sup>2</sup> polystyrene film with a grounding ring of alcohol dag. This source was measured in one of the pair of lens  $\beta$ -ray spectrometers placed end to end, described in previous publications (3, 4). The results on  $\text{Au}^{199}$  published by two of us (4, 10) were obtained using this source, and further studies on  $\text{Au}^{199}$  have given results substantially in agreement with those of Sherk and Hill (18). The observed  $\beta$ -ray spectrum of  $\text{Au}^{199}$  is shown in Fig. 1(a), where the number of counts per unit momentum interval is plotted on an arbitrary scale as a function of  $H\rho$ . The stronger conversion lines of the  $\gamma$ -rays of energy 49, 158, and 207 kev. are labelled in the usual way, and the high energy part of the spectrum has been plotted on an expanded scale to show the weak high energy component of the  $\text{Au}^{199}$   $\beta$ -spectrum. The sensitivity of the scintillation counter used as detector in the  $\beta$ -ray spectrometer was constant above  $H\rho = 900$ , but fell off sharply below  $H\rho = 600$  (30 kev.), and the shape of the spectrum below  $H\rho = 600$  has been filled in with a dashed line calculated on the assumption that the  $\text{Au}^{199}$   $\beta$ -ray spectrum components have the allowed shape. The total area of the primary  $\beta$ -ray spectrum, using this calculated line, is insensitive to this assumption and to any small errors in the measured values (4) of the end points of the components of the  $\text{Au}^{199}$  spectrum.

\*The correction of one per cent quoted by both Carter *et al.* and Egelstaff applied only to mono-kinetic neutrons of velocity 2200 meters sec.<sup>-1</sup>.

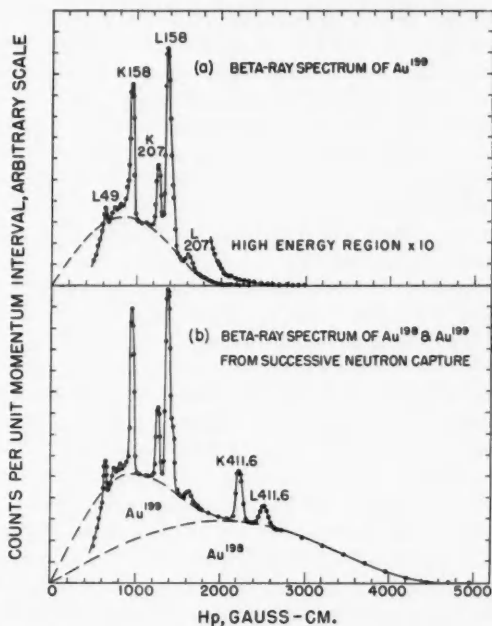


FIG. 1. (a)  $\beta$ -ray spectrum of  $\text{Au}^{199}$  observed in a magnetic lens spectrometer having a line-width at half maximum of 3.5%. The shape of the  $\beta$ -ray spectrum below the counter cutoff at  $H\rho = 600$  has been calculated and is shown as a broken line. The statistical standard deviations are everywhere smaller than the diameter of the circles used to indicate the points.

(b)  $\beta$ -ray spectrum of  $\text{Au}^{198} + \text{Au}^{199}$  formed by the successive neutron capture process. The shape of the  $\text{Au}^{198}$  spectrum below  $H\rho = 2000$  has been calculated and is shown as a broken line. The statistical standard deviations are everywhere smaller than the diameter of the circles used to indicate the points.

After establishing the details of the  $\text{Au}^{199}$  spectrum in this manner, the successive neutron capture effect was first examined using a sample of gold leaf known to contain less than one part per million of platinum\*. A disk of this material 5.3 mm. in diameter, of surface density  $171 \mu\text{gm./cm.}^2$ , was irradiated in the NRX reactor at a point where the thermal neutron flux was known to be about  $4 \times 10^{13} \text{ cm.}^{-2} \text{ sec.}^{-1}$ . The irradiation period lasted 14.4 days, with interruptions that were short compared with the total period; only two of the interruptions were long enough to require correction in the calculations.

After this source had decayed for 15 days, it was mounted on  $1.5 \text{ mgm./cm.}^2$  aluminum foil and examined in the same  $\beta$ -ray spectrometer as was used for the  $\text{Au}^{199}$  source. The  $\beta$ -ray spectrum of this source, Fig. 1(b), is a mixture of the well-known  $\text{Au}^{198}$  spectrum and the  $\text{Au}^{199}$  spectrum illustrated in Fig. 1(a).

\*Hill and Mihelich (12) have already shown that the effect observed by them could not be explained by a platinum impurity in their gold sample; the same is true *a fortiori* in the present case.



The  $\text{Au}^{199}$  component of Fig. 1(b) was identified by its similarity to Fig. 1(a), by the fact that the  $\text{Au}^{199}$  conversion lines decayed with the 3.15-day half-life appropriate to them, and by the measurement in this source of the  $2.35 \times 10^{-9}$ -sec. half-life with which the 158 kev. gamma-ray follows the nuclear  $\beta$ -rays of  $\text{Au}^{199}$  (10). The source was thin and uniform, and the  $\text{Au}^{199}$  part was so strong that some of the conversion lines belonging to the  $\text{Au}^{199}$  decay were most conveniently studied using mixed sources.

The ratio of the source strength of  $\text{Au}^{199}$  relative to that of  $\text{Au}^{198}$  was deduced from the spectrum shown in Fig. 1(b) in two different ways, neither of which requires detailed information on the disintegration schemes of  $\text{Au}^{198}$  and  $\text{Au}^{199}$ . In the first method, the underlying  $\text{Au}^{198}$   $\beta$ -ray continuum in Fig. 1(b) is assumed to follow the allowed shape, as found by Langer and Price (15); the calculated shape of the part lying under the  $\text{Au}^{199}$  spectrum is shown in Fig. 1(b) as a broken line, which separates the mixed spectrum into the required two parts. In the second method the area of the stronger conversion lines in Fig. 1(a) was measured as a fraction of the area under the  $\text{Au}^{199}$   $\beta$ -ray continuum; measurement of the corresponding line areas in Fig. 1(b) then gives a figure for the area of the  $\text{Au}^{199}$  continuum in Fig. 1(b). The two methods agree within five per cent, giving a ratio  $\text{Au}^{199}/\text{Au}^{198}$  of  $0.49 \pm 0.02$  at the time the data used in Fig. 1(b) were recorded. The value of this ratio calculated back to the end of the pile irradiation period is  $0.277 \pm 0.015$ , using half-lives of 2.698 days for  $\text{Au}^{198}$  (5) and 3.15 days for  $\text{Au}^{199}$ . The specific activity of the  $\text{Au}^{198}$  component was determined by conversion electron - beta-ray coincidence counting in the pair of lens spectrometers, as described on p. 44 of Reference (4). The weight of the sample foil was 37.7  $\mu\text{gm}$ .

The resonance correction factor  $R = 1.434$  used for this experiment was determined during a later irradiation in a different pile position. Separate experiments have shown that  $R$  is nearly constant for the various irradiation positions throughout NRX. The cross section for  $\text{Au}^{198}$  deduced from this experiment is listed in Table I.

TABLE I  
SUMMARY OF PRESENT  $\text{Au}^{198}$  CAPTURE CROSS SECTION MEASUREMENTS

Reactor	Date	$R$ (see Eq. [4])	Thermal flux ( $\text{cm}^{-2} \text{ sec}^{-1}$ )	$\sigma_c(\text{Au}^{198})$ (barns)	Error (%)
NRX	1951	(1.434) <sup>a</sup>	$4.6 \times 10^{13}$	26,800	9.9
NRX	1954	1.434	$5.0 \times 10^{13}$	27,300	8.3
Brookhaven	1953	1.837	$4.0 \times 10^{12}$	21,400	22.9
MTR	1953	1.165	$8.6 \times 10^{13}$	25,100	7.2
Weighted average $26,000 \pm 1200$ barns					

<sup>a</sup> Value assumed the same as that for the 1954 NRX irradiation (see text, Section III(b)).

To test for any possible dependence of the  $\text{Au}^{198}$  cross section on neutron flux or temperature, three other irradiations were made, using the NRX reactor, the Materials Testing Reactor at Arco, Idaho, and the Brookhaven reactor. In each case cadmium-shielded gold foils were included in the same



container, and the procedure for evaluating results was the same as for the first sample. The results from the four irradiations are tabulated in Table I. The error listed in the last column is the standard deviation due to a combination of the errors in (a) sample weights, (b)  $\text{Au}^{199}/\text{Au}^{198}$  ratio, (c)  $\text{Au}^{198}$  source strength, and (d) cadmium ratio and hence  $R$ . It is gratifying to see that the four values agree well within the limits of error despite the large differences in flux and resonance activation. A valuable by-product of the experiments is the measurement of the neutron flux to approximately five per cent for each irradiation; the values so obtained are listed in Table I.

In the course of one experiment the  $\beta$ -ray spectrum of a cadmium-shielded gold foil was examined carefully for the possible presence of  $\text{Au}^{199}$  lines. Comparing with the  $\text{Au}^{199}/\text{Au}^{198}$  ratio observed in the unshielded foil we can set a limit of  $<5 \times 10^{-3}$  on the ratio of epi-cadmium to thermal neutron capture in  $\text{Au}^{198}$  in NRX.

During the course of another experiment a qualitative search was made for possible neutron capture in  $\text{Au}^{199}$ , which, if present, would of course influence the answers for  $\sigma(\text{Au}^{198})$ . Au foils with a known amount of  $\text{Au}^{199}$  present were irradiated for half-hour periods in a thermal neutron flux of about  $2 \times 10^{13}$  neutrons  $\text{cm}^{-2} \text{sec}^{-1}$ , and examined for the energetic 48-min. activity of  $\text{Au}^{200}$  (13). No activity with such a period was observed, and we can set an upper limit on the thermal neutron capture cross section of  $\text{Au}^{199}$  of about 3000 barns. The error in  $\sigma(\text{Au}^{198})$  caused by the neglect of neutron capture by  $\text{Au}^{199}$  is then less than approximately three per cent.

#### IV. DISCUSSION

Table II summarizes the various published values of the thermal neutron capture cross section of  $\text{Au}^{198}$  in order of their appearance in the literature.

TABLE II  
PUBLISHED VALUES OF  $\text{Au}^{198}$  CROSS SECTION

$\sigma_c$ (barns)	Experimenters	Ref.
35,000	Hill and Mihelich	(12)
16,000	Hill	(11)
38,000	Sherk and Hill	(18)
91,000	Fan	(9)
$26,400 \pm 5300$	Bedford and Crooker	(1, 2)
$26,000 \pm 1200$	Present work	

The first two values were tentative ones as pointed out in Section I above. The third value reported by Sherk and Hill followed a detailed examination of the disintegration scheme of  $\text{Au}^{199}$  in which accurate values were obtained for the intensities of the various conversion lines. Since their intensity values are in quite good agreement with those determined during the course of the present investigation the discrepancy in the cross section values must be largely due to other causes. The most probable source of error would seem to be in the thermal neutron flux of  $10^{12}$  neutrons  $\text{cm}^{-2} \text{sec}^{-1}$  assumed for their

irradiation. The very large discrepancy between Fan's value and the others "might be partly due to the pile neutron flux on which the calculations are based" (9). Careful comparison of Fig. 11 in Fan's paper (9) with Fig. 1 in the present paper suggests that the low energy part of his spectrum may not be entirely due to  $\text{Au}^{199}$ . The prominent  $K158$  and  $L158$  conversion lines are barely observable in his work while the intensity of the  $\text{Au}^{199}$  part of the spectrum at about  $2000 H\beta$  seems much too great. As pointed out elsewhere in this issue (2), the value first obtained by Bedford and Crooker (1), when corrected for finite irradiation time and "burnout" of  $\text{Hg}^{199}$  during the irradiation, is in agreement with the present work.

The large cross section determined in these experiments must be due to an energy level at a small (positive or negative) neutron energy, so that the cross section probably does not follow a  $1/v$  law. The measured cross section should therefore not be referred to as a thermal neutron cross section, but rather as an average cross section for "pile neutrons below 0.5 ev." On the other hand the relative constancy of the cross section measured in different reactors, where the epi-cadmium effect varies widely (see Table I), suggests that the departure from  $1/v$  is not very great. As pointed out by Hughes (Reference 14, p. 180) the activity ratio of two nuclei, one of which has a non- $1/v$  cross section, will depend somewhat upon the neutron temperature. The correction, if any, cannot be made here since we do not have an accurate measure of the neutron temperature and also we do not know the shape of the cross section curve for  $\text{Au}^{198}$ . The present experiments indicate only that the curve rises sharply below 0.5 ev. A transmission experiment to determine its shape is feasible in principle, since as shown in these experiments it is easily possible to obtain a neutron opacity due to  $\text{Au}^{198}$  which is comparable with that due to  $\text{Au}^{197}$ .

#### ACKNOWLEDGMENTS

The authors are indebted to Drs. L. G. Elliott and D. G. Hurst for many valuable discussions, and would like to thank Mr. J. S. Geiger for checking many of the calculations. The irradiation in the Materials Testing Reactor was made by the USAEC through the auspices of the Joint Technical Co-operation Program.

#### REFERENCES

1. BEDFORD, R. E. and CROOKER, A. M. Can. J. Phys. 33: 25. 1955.
2. BEDFORD, R. E. and CROOKER, A. M. Can. J. Phys. 33: 492. 1955.
3. BELL, R. E. and GRAHAM, R. L. Phys. Rev. 86: 212. 1952.
4. BELL, R. E., GRAHAM, R. L., and PETCH, H. E. Can. J. Phys. 30: 35. 1952.
5. BELL, R. E. and YAFFE, L. Can. J. Phys. 32: 416. 1954.
6. CARTER, R. S., PALEVSKY, H., MYERS, V. W., and HUGHES, D. J. Phys. Rev. 92: 716. 1953.
7. DE-SHALIT, A., HUBER, O., and SCHNEIDER, H. Helv. Phys. Acta, 25: 259. 1952.
8. EGELSTAFF, P. A. J. Nuclear Energy, 1: 57. 1954.
9. FAN, C-Y. Phys. Rev. 87: 252. 1952.
10. GRAHAM, R. L. and BELL, R. E. Phys. Rev. 84: 380. 1951.
11. HILL, R. D. Phys. Rev. 79: 413. 1950.
12. HILL, R. D. and MIHELICH, J. W. Phys. Rev. 79: 275. 1950.
13. HOLLANDER, J. M., PERLMAN, I., and SEABORG, G. T. Revs. Mod. Phys. 25: 469. 1953.
14. HUGHES, D. J. Pile neutron research. Addison-Wesley Press Inc., Cambridge, Mass. 1953.

15. LANGER, L. M. and PRICE, H. C. Phys. Rev. 76: 641. 1949.
16. McMILLAN, E. M., KAMEN, M., and RUBEN, S. Phys. Rev. 52: 375. 1937.
17. SARGENT, B. W., YAFFE, L., and GRAY, A. P. Can. J. Phys. 31: 235. 1953.
18. SHERK, P. M. and HILL, R. D. Phys. Rev. 83: 1097. 1951.

## THE INITIAL OXIDATION OF NICKEL<sup>1</sup>

BY URSULA M. MARTIUS

### ABSTRACT

This paper describes the first stages of oxidation of nickel. Under suitable experimental conditions small isolated crystallites are formed prior to the occurrence of a continuous oxide film. The shape, size, and number of the crystallites depends on the crystallographic orientation of the underlying metal. The specific features of the oxidation of grain boundaries are discussed and a tentative explanation of the observed phenomena is advanced.

The mechanism of oxidation of metals is a subject of considerable interest both from a theoretical and from a practical point of view. A number of recent publications have summarized the present state of our knowledge of this problem (6, 7, 8).

However, in spite of the attention which is paid at present to the elementary processes of the oxidation of metals, not much experimental evidence exists as to the mechanism of nucleation of an oxide layer on the surface of a metal crystal. The work of Bardolle and Benard on the oxidation of iron (1, 2) and brief reports on electron microscopic work on copper and iron (5, 4) seem to be the only experimental evidence of work done on this part of the problem of oxidation. Bardolle and Benard observed the formation of small oxide crystallites—they called them oxide "germs"—on the surface of an iron crystal heated up to 850°C. in vacuum or in H<sub>2</sub> containing traces of O<sub>2</sub>, at the very early stages of oxidation. These crystallites, which appeared on very slightly oxidized, electropolished surfaces prior to the formation of a continuous layer of oxide, were of fairly uniform shape. Their size and shape, as well as their number per unit surface area, varied with the crystallographic orientation of the underlying metal surface. Bardolle (1) found a ratio of 1:100 when comparing the number of crystallites on a (110) and a (100) plane of iron.

Bardolle and Benard, as well as Gulbransen and McMillan (4), reported that in the case of iron, on further oxidation and under otherwise constant experimental conditions, the number of oxide crystallites increases. This result holds, regardless of whether the increased oxidation is the result of an increase in oxygen pressure or an increase in oxidation time.

The electron microscope work of Harris and Ball (5) deals with the initial oxidation of a (311) face of a single crystal of copper, at temperatures between 150°C. and 250°C. With increasing oxidation time the number of crystallites and their individual diameters were reported to increase. Both quantities seem to reach a limiting value which is quoted as  $4 \times 10^{11}$  crystallites per mm.<sup>2</sup> and 80 Å respectively at 150°C.

In the following paragraphs the results of microscopic observations during the early stages of oxidation of high purity nickel are reported.

<sup>1</sup>Manuscript received April 4, 1955.

Contribution from the Department of Engineering and Metallurgy, Ontario Research Foundation, 43 Queen's Park, Toronto 5, Ontario.

## EXPERIMENTAL PROCEDURE

The starting material was a cold rolled nickel sheet of very high purity, which was mechanically polished and annealed for two hours at 1100°C. The samples were then electrolytically polished in a sulphuric acid bath and examined microscopically under polarized light and under dark field illumination. The sample showed no grain boundaries, no "surface structure", and only very few etch pits. The amount of electropolish was so slight that no waviness could be detected on the metal surface.

The specimens were then heated up to a temperature of 1100°C. under a stream of hydrogen, which contained a trace of water vapor, and kept at that temperature for times varying from 10 min. to two hours. The samples were allowed to cool down slowly, remaining under hydrogen until room temperature was reached. The samples were examined microscopically in bright field and dark field, with polarized light and by means of phase contrast arrangements. Photomicrographs were taken at 1000 $\times$ , some of which were subsequently magnified 2.5 $\times$ .

## OBSERVATIONS

The experimental conditions described above yield a sample at the initial stage of oxidation. It is not yet covered with a continuous oxide film (no interference colors are visible), but small individual oxide crystallites\* have formed on the surface. Each nickel grain, depending on its crystallographic orientation, shows a difference in the number, the size, and the orientation of the oxide crystallites on its surface. Fig. 1 and Fig. 2 are typical examples of this. Fig. 1 is a photograph taken on a sample after a 10 min. anneal at 1100°C. in H<sub>2</sub> containing a trace of water vapor. Fig. 2 was taken on a sample which was annealed for one hour under identical conditions. It was found that with increasing time the number of oxide crystallites on the surface increased. Their individual size increased also, although this increase in size is much less pronounced than the increase in number. Further oxidation led to a continuous oxide layer, which then showed interference colors.

## OXIDATION AT GRAIN BOUNDARIES

One of the most interesting features at the early stages of oxidation is the microscopic study of the oxidation at the grain boundaries. A study of varying oxidation behavior of grain boundaries of known orientation and dislocation arrangement may well provide useful and possibly conclusive information as to the mechanism responsible for the formation of these first oxide crystallites.

On the basis of the experimental material available the following observations can be made concerning the high temperature oxidation at grain boundaries in nickel.

(A) Some grain boundaries show a string of oxide crystallites, aligned

\*The word "crystallites" is used in preference to nuclei, which—although it describes the actual state of affairs very aptly—has a well-defined thermodynamic meaning, and within the framework of this thermodynamic usage small stable oxide crystals, which can be observed microscopically, are not "nuclei".

along the grain boundaries rather than following the shape and orientation of the oxide crystallites on the surface of the grains on either side of the boundary.

(B) Some grain boundaries show oxide crystallites of an orientation and shape similar to that of the oxide crystallites on one of the neighboring grains. (This is observed most frequently on very thin oxide layers.)

(C) Certain grain boundaries, especially twin boundaries, exhibit no oxidation pattern of their own.

All these cases are illustrated in the following figures:

Fig. 1 illustrates Case B, especially for the left-hand grain boundary.

Fig. 2 shows part of a nickel sheet where three grains of different orientation meet, one of them (top half of the figure) contains a twin crystal. It can be seen that the type of oxidation which occurs along the boundaries between the three grains (Case A) does not occur along the twin boundaries (Case C).

In Fig. 3 a twin crystal has just started to grow from a corner where three grains meet. As in Fig. 2, the grain boundaries show a distinct oxidation pattern (Case A) while the twin boundary has no such pattern. The appearance of annealing twins at high energy grain boundary corners in nickel has been observed frequently; measurements of the grain boundary angles, which will be reported separately, are in complete agreement with Fullmann and Fisher's theory of the origin of annealing twins, developed from studies of the twinning of copper (3).

Fig. 4 shows very clearly that the amount of oxidation along a grain boundary may depend on its orientation.

Fig. 5 illustrates the frequent observation that an old trace of a grain boundary can often be recognized by its oxide pattern.

Fig. 6 shows a photomicrograph of the region around a grain boundary, taken with phase contrast illumination. This picture, and many other similar observations, makes a very tempting case for the following tentative interpretation of the observed oxidation phenomena.

#### INTERPRETATION

From extensive theoretical and experimental work the over-all mechanism of oxidation of nickel is known (9). The rate of oxidation is determined by the self-diffusion of nickel. At the points on the nickel surface at which we find visible oxide crystallites during the initial oxidation the "local" rate of diffusion of nickel must have been high. The surface points at which the oxide crystallites begin to form and continue to grow are definitely related to the crystallography of the underlying metal surface. These "growth sites" will be positions at which nickel can diffuse preferentially, be it on account of the geometry of the lattice, or on account of existing lattice imperfections.

The observations at grain boundaries, especially pictures like Fig. 4, strongly stress the role of certain crystal imperfections, most likely screw dislocations, in the process of oxidation of metals. The fact that twin boundaries do not show oxide patterns of their own is another indication along the same lines.

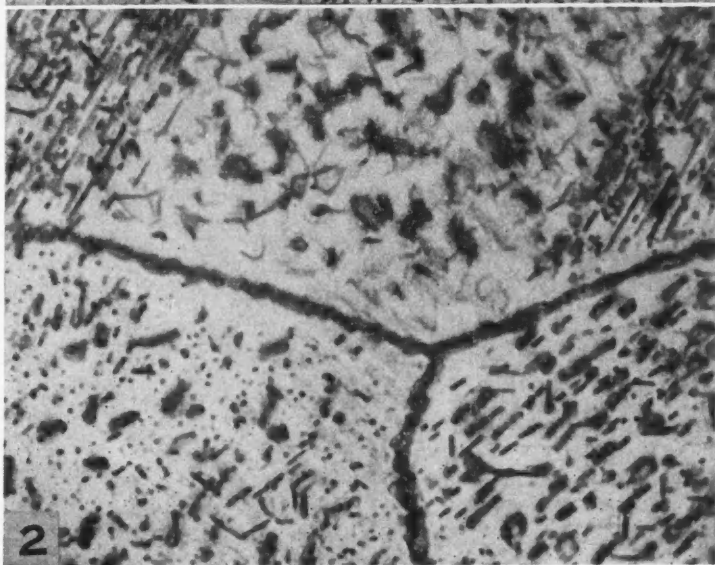
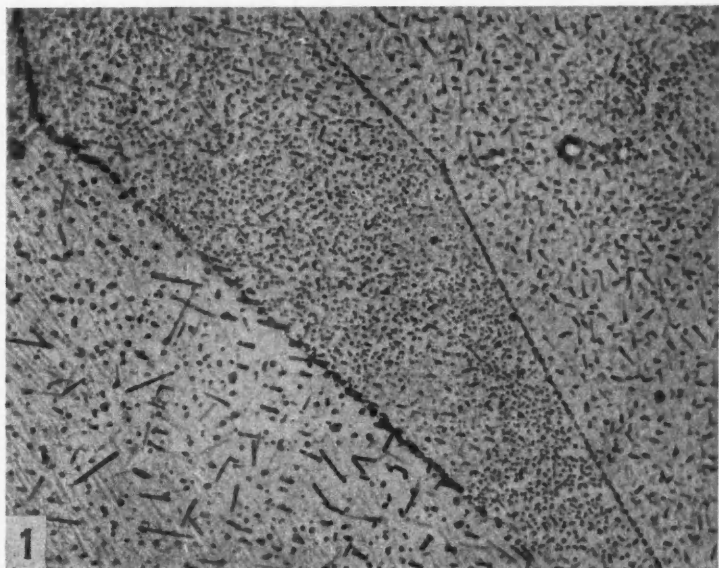


FIG. 1. 1000X. Bright field.

FIG. 2. 2500X. Bright field.

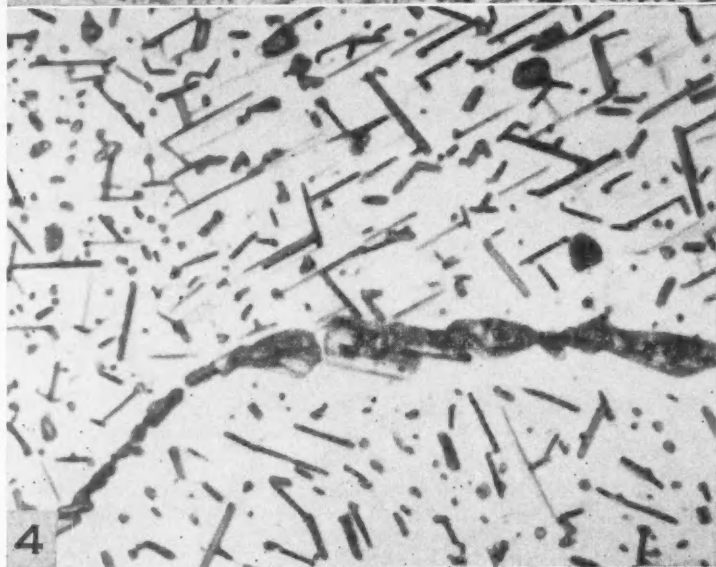


FIG. 3. 2500X. Bright field.

FIG. 4. 2500X. Bright field.



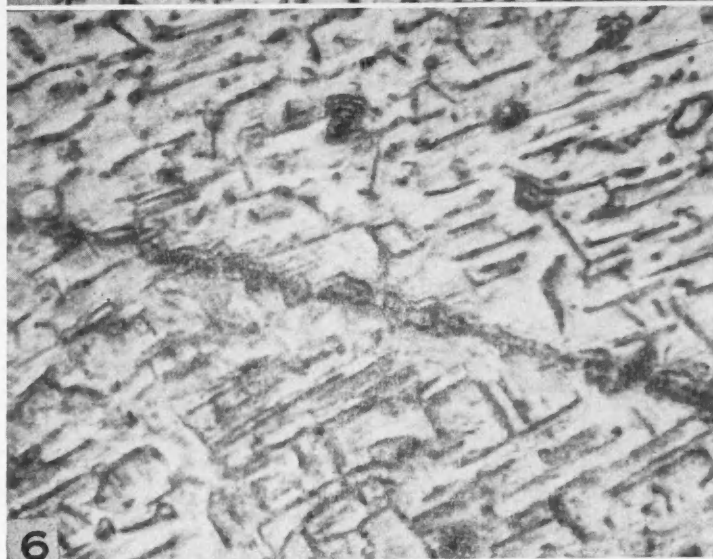
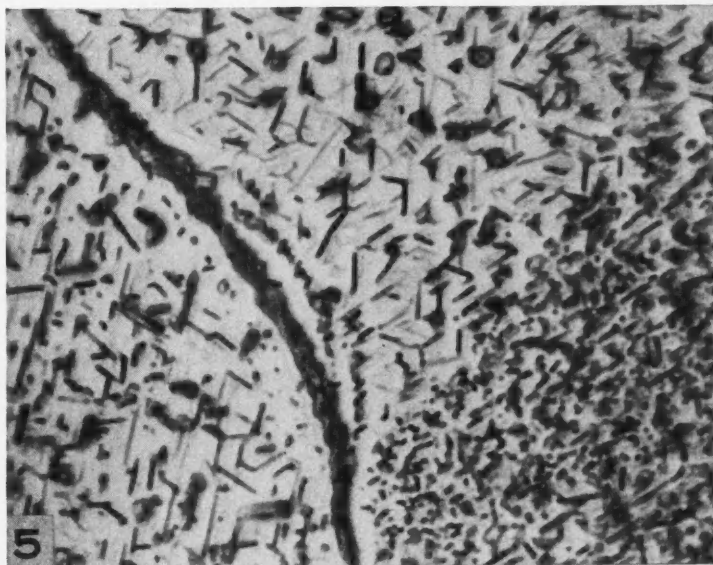


FIG. 5. 2500X. Bright field.

FIG. 6. 2500X. Phase contrast.

It would seem that the study of the rate of oxidation at grain boundaries of known orientation and dislocation composition might be a very fruitful approach towards a solution of this facet of the problem of oxidation of metals. Conversely, the technique of partial oxidation may develop into a useful tool for the detection of certain types of lattice imperfections. One might, for instance, attempt to supplement studies of creep by such observations. In addition one should not overlook the possible practical consequences that would arise from knowing the oxidation patterns of grain boundaries and from possibly being able to produce materials with grain boundaries of only low rates of oxidation.

#### ACKNOWLEDGMENTS

I would like to acknowledge Mr. E. Niskanen's experimental help and Mr. S. J. Majka's advice on microscopic techniques. My sincere thanks are due to Mr. P. E. Cavanagh, Director, Department of Engineering and Metallurgy, Ontario Research Foundation, for his continued interest and encouragement.

#### REFERENCES

1. BARDOLLE, J. *Rev. mét.* 51: 835. 1954.
2. BARDOLLE, J. and BENARD, J. *Rev. mét.* 49: 613. 1952.
3. FULLMANN, R. L. and FISHER, J. C. *J. Appl. Phys.* 22: 1350. 1953.
4. GULBRANSEN, E. A. and McMILLAN, W. R. *J. Appl. Phys.* 24: 1416 (A). 1953.
5. HARRIS, W. W. and BALL, F. L. *J. Appl. Phys.* 24: 1416 (A). 1953.
6. HAUFFE, K. The mechanism of oxidation of metals and alloys at high temperature. *Progress in Metal Physics*, Vol. IV. Pergamon Press, London. 1953.
7. KUBASCHEWSKI, O. and HOPKINS, B. E. *Oxidation of metals and alloys*. Academic Press, Inc., New York. 1953.
8. SEIFERT, F. *Epitaxis. Structure and properties of solid surfaces*. University of Chicago Press, Chicago. 1953.
9. WAGNER, C. and ZIMENS, K. E. *Acta Chem. Scand.* 1: 1954. 1947.

# A METHOD OF EXAMINING STRUCTURAL CHANGES OF METALS ON DEFORMATION IN LIQUID HELIUM: EXAMINATION OF INDIUM<sup>1</sup>

By W. B. PEARSON

## ABSTRACT

A Debye-Scherrer type of X-ray camera is described in which a soft metal can be deformed by extension and photographed *in situ* in liquid helium. Using this camera we have examined deformed indium at 4.2°K. and find no evidence of a lattice transformation when a tensile strain of ~15% is applied. The investigation was undertaken to examine the suggestion of Swenson, stemming from the observation of anomalies in the mechanical properties of indium at low temperatures, that a very slight deformation of indium at 4.2°K. might transform the face-centered tetragonal to a close-packed structure.

## INTRODUCTION

Investigations of the mechanical properties of indium at low temperatures by Swenson (2) reveal anomalies\* which have been interpreted as due to a shear-sensitive transition from the face-centered tetragonal to a close-packed structure below 50°K. It was suggested that in the liquid helium range very slight deformation of indium could nucleate the transition and cause it to run to completion. In order to test this suggestion, X-ray photographs have been made at 4.2°K. of indium strained *in situ* in liquid helium.

## EXPERIMENTAL

In order to examine metals strained *in situ* at liquid helium temperatures, we have followed the method of Reekie, Hutchison, and Beaumont (1) in which the X-ray camera is located in liquid helium in a Dewar flask. The camera (*S*, Fig. 1), 6 cm. in diameter and having asymmetric film mounting, is located at the end of a brass tube, *U*, down which the X-ray beam passes. The face plate, *T*, at the top of it is screwed to a Machlett X-ray tube, *A*, secured on a Hammond rack at an angle such that the brass tube lies in the vertical plane. With this arrangement exposures of four hours can be obtained using a total of some three liters of liquid helium.

The specimen under investigation, *M*, is mounted along the camera axis normal to the X-ray beam in such a way that it is soldered to the mounts, *L* and *N*, at each end of it. These mounts are, however, quite independent of each other. When the camera has been cooled to 4.2°K. in liquid helium, the lower of these specimen mounts, *N*, can be withdrawn 2 or 3 mm. through the base of the camera by operation of the lever, *F*, as also shown dotted in Fig. 1, *P*. This extends the specimen some 15% in length while it retains its position along the axis of the camera. By pushing the lower specimen mount, *N*, slightly in before the camera is cooled, it is possible to ensure that the specimen is not strained previously at some higher temperature during the

<sup>1</sup>Manuscript received March 23, 1955.

Contribution from the Division of Physics, National Research Council, Ottawa, Canada. Issued as N.R.C. No. 3667.

\*Anomalies were observed in the compressive yield strength, strain hardening coefficient, and extrusion pressure.

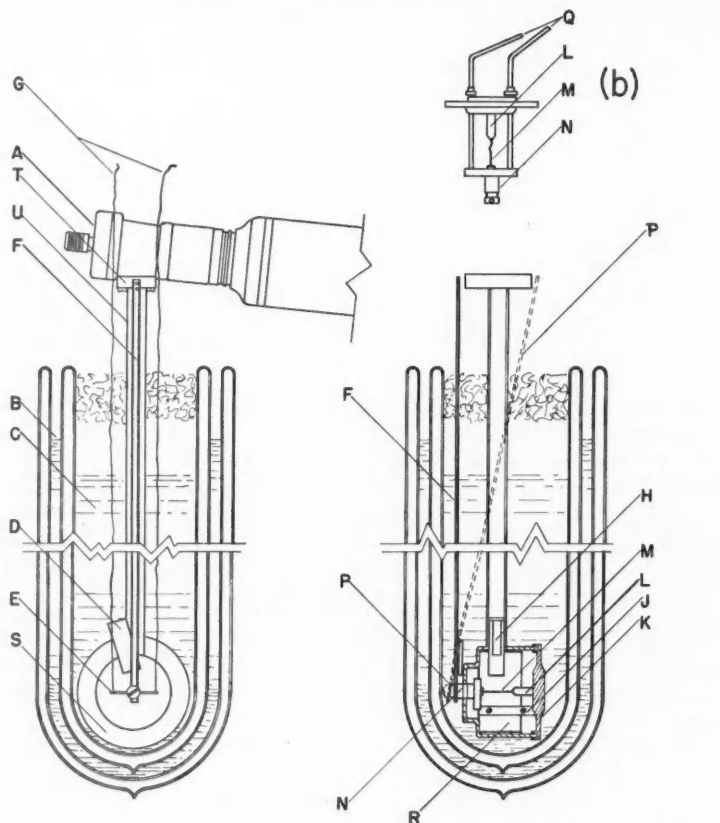


FIG. 1. X-ray camera used for examining metals strained *in situ* in liquid helium. (b) Jig for loading specimen in camera.

A Machlett X-ray tube  
 B Liquid nitrogen  
 C Liquid helium  
 D Pivot for lever F  
 E Rotation arm  
 F Extension lever in its normal position  
 G Wires for rotation of specimen  
 H Collimator slits for X-ray beam  
 J Film-retaining clip  
 K Camera lid  
 L Upper specimen mount

M Specimen  
 N Lower specimen mount  
 P Extension lever F in position for full extension  
 Q Screws comprising jig for specimen mounting  
 R X-ray film  
 S X-ray camera  
 T Flange at top of brass tube  
 U Brass tube securing camera to X-ray tube

cooling process as the materials of the camera contract. The two wires, G, attached to the ends of the rotation arm, E, on the lower specimen mount, N, permit a rotation of the specimen of some  $90^\circ$ . By rotating the specimen slightly backwards or forwards every few minutes during the exposure, fairly smooth diffraction rings are obtained.

In order to mount the specimen in the camera, we made use of the jig shown in Fig. 1(b). When this is assembled, the upper and lower specimen mounts, *L* and *N*, are held rigidly together by two screws, *Q*. The specimen is placed in axial holes in the specimen mounts and soldered in position. This ensures that it will be in the X-ray beam when mounted in the camera. The X-ray film, *R*, is loaded in the camera and the jig (and camera lid, *K*) is pressed in and fitted tightly. The rotation and extension levers, *E* and *F*, are then secured to the shaft of the lower specimen mount with a single screw. As the lower specimen mount is now held securely so that it can no longer be withdrawn inwards through the camera, the two screws, *Q*, in the assembly jig can be withdrawn leaving the upper and lower specimen mounts secured in the camera but independent of each other. In order to disassemble, this process is repeated in reverse.

#### OBSERVATIONS ON INDIUM

Using the arrangement described above, we have examined indium at 4.2°K. both unstrained and strained *in situ*. We find: (1) that indium has the same face-centered tetragonal structure at 4.2°K. as at room temperature; (2) that an indium rod ~0.75 mm. in diameter, prepared by rolling, extended 2 mm. from an unstrained length of 13 mm. at 4.2°K. and photographed, showed no change of crystal structure; (3) that an indium wire prepared by extrusion and extended 2 mm. in a length of 14 mm. at 4.2°K. gave a similar result.

In experiment (2) the strain was not uniform along the length of the rod; however, in (3) this was remedied and the region examined by X-rays (the collimator slit was 4×0.5 mm.) was without any doubt strained by 10 or more per cent. This was confirmed by comparing the diameter of the specimen located in the X-ray beam before and after straining. In the present experiments strong absorption by the indium in the transmission region prevented observation of weak reflections at low Bragg angles. This renders the experiments insensitive for detecting very small amounts of a possible transition. But it is certain that, under the conditions of the experiment when a tensile strain of more than 10% is applied, there has been no transition of as much as say 15–25% of the indium present.

If, therefore, indium does undergo a shear-sensitive transition at low temperatures, the transition can involve only a relatively small proportion of the bulk metal, and it *may* be necessary to look to another mechanism in order to explain the reported anomalies in the mechanical properties.

#### ACKNOWLEDGMENT

I am grateful to Dr. C. A. Swenson for bringing this problem to my notice and for showing me manuscripts before publication, also to Mr. F. W. Richardson who constructed the camera.

#### REFERENCES

1. REEKIE, J., HUTCHISON, T. S., and BEAUMONT, C. F. A. Proc. Phys. Soc. (London), A, 66: 409. 1953.
2. SWENSON, C. A. Private communication. 1954.

# RADIO STAR SCINTILLATIONS AND THE IONOSPHERE<sup>1</sup>

By T. R. HARTZ

## ABSTRACT

The observed intensity at the surface of the earth of radiation at a frequency of 50 Mc./s. from a radio star has been studied. A relationship is shown to exist between the fluctuations, or scintillations, in this observed radiation intensity and the angle of its incidence on the 400 km. level of the earth's ionosphere. The occurrence of these scintillations is compared with other ionospheric phenomena as determined by vertical soundings from the earth. The probable cause of the fluctuations has been localized to a source in the high ionospheric regions.

## INTRODUCTION

It has been shown that the observed radiation from "radio stars" fluctuates in a random manner (2, 3, 5, 6). This fluctuation, or scintillation, results from the passage of the radiation through inhomogeneities in the ionosphere, and is analogous to the twinkling or scintillation of the visual stars. The small-scale structure of the ionosphere is such as to diffract, refract, or absorb some of the radiation, thereby causing a relatively rapid variation in the observed intensity. From a study of these fluctuations it is possible to draw certain conclusions about the ionospheric irregularities, and to make comparisons with other ionospheric data obtained by methods which measure essentially large-scale structure.

## EXPERIMENTAL

The radiation from the intense source in the constellation of Cassiopeia (R.A. 23 h. 21 m. 12 s., Dec.  $+58^{\circ} 32'$ ) was recorded at a frequency of 50 Mc./s. for some 18 months at Ottawa (lat.  $45.4^{\circ}\text{N.}$ , long.  $75.9^{\circ}\text{W.}$ ). An interferometer type antenna consisting of two horizontal dipoles spaced 10 wavelengths apart was used. A phase reversing switch was employed in the cable from one antenna, and this, together with a phase sensitive detector at the receiver output, permitted the cancellation of the general background radiation. With the exception of the phase reversing switch, which was a new one developed in the Radio Physics Laboratory, the equipment was similar to that suggested by Ryle (4). The records obtained showed a series of maxima and minima characteristic of the interferometer type antenna, with zero sensitivity at the center of the chart. The displacement from the chart center was essentially a measure of the radiation from the discrete source only. The use of dipole antennas permitted continuous recording over a 24 hr. period, so that with the exception of times of equipment failure a continuous record of the source was obtained.

The receiver used had a bandwidth of 17 kc./s., and the recording system employed a time constant of 60 sec.

<sup>1</sup>Manuscript received May 4, 1955.

Contribution from the Radio Physics Laboratory, Defence Research Board, Ottawa, Canada. This work was performed under project PCC No. D48-28-01-02.

## RESULTS AND THEIR INTERPRETATION

As the earth rotates, the source appears to move through a series of antenna lobes. The records obtained from such a system should consist essentially of a sinusoidal trace in the absence of atmospheric effects. When the radiation is affected by the ionosphere, the recorder trace shows fluctuations superimposed on the sinusoidal trace. Fig. 1 shows examples of these fluctuations or scintillations on the normal sinusoidal trace of the recorder.

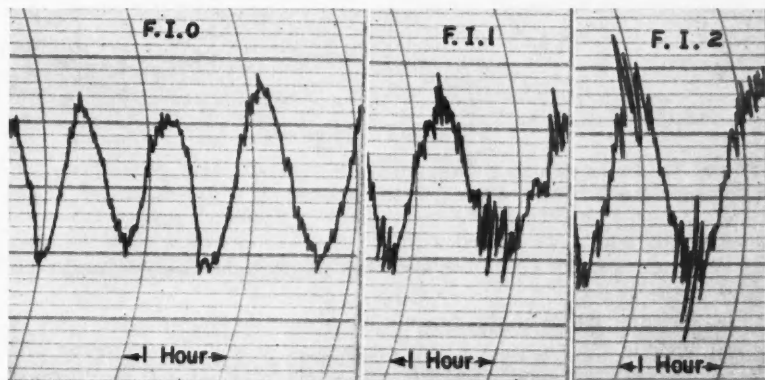


FIG. 1. Typical records of intensity fluctuations of the Cassiopeian source showing the fluctuation indices (F.I.) used.

The records have been analyzed for the occurrence of scintillations by assigning a fluctuation index to the record for each hour. This fluctuation index is the ratio of the r.m.s. deviation of the amplitude to the mean amplitude, and has been used as such by other observers (1). Because of the large time constant used in the recording system, it has been convenient to limit the indices used to the integers 0, 1, and 2. Typical records for each index are shown in Fig. 1.

#### A. Sidereal Dependence

A preliminary survey of the results indicated that, in general, the larger fluctuation index corresponded to large zenith angles of the source. A similar result has been obtained by Hewish (1). In order, then, to obtain results which indicate occurrence of scintillations, the indices 1 and 2 were grouped into one class. That is, the present records were analyzed using only the fluctuation indices 0 and 1, indicating respectively 'no scintillation' and 'scintillation' for the corresponding hour.

The results from 18 months of recordings have been reduced to results for a year by averaging records for corresponding times of the year. These results have been summed and plotted against sidereal time as shown in Fig. 2. The ordinate is a plot of the percentage occurrence of scintillations with respect to the total number of observations for the corresponding hour. The

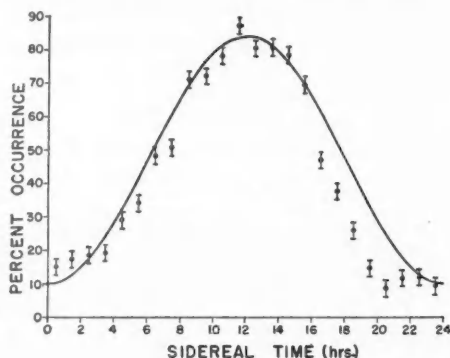


FIG. 2. The sidereal variation of the occurrence of scintillations. The full trace is a sinusoidal curve which has been included for comparison.

experimental points are plotted with the standard deviation error indicated. For comparison a sine curve has also been plotted; this is shown as the full curve in the figure.

Fig. 2 clearly indicates the dependence of scintillation occurrence on the zenith angle of the source; the greatest number of scintillations occur when the source is at lower transit, and the least when the source is at upper transit. At Ottawa, the source moves between zenith angles of  $13.1^\circ$  and  $76.1^\circ$ . A similar result might be expected from a simple consideration of dependence on the length of the path through the ionosphere in the direction of the source and, hence, on the secant of the angle of incidence. If the secant of the angle of incidence of the ray on the "top" of the ionosphere (400 km. level) is used, as illustrated in Fig. 3, the scintillation dependence shown graphically in Fig. 4 results.

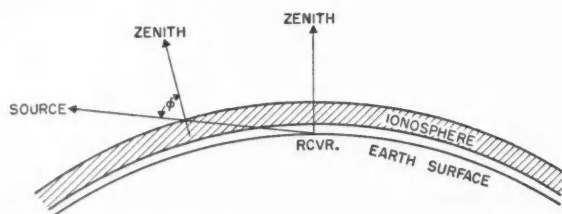


FIG. 3. Geometrical configuration of incident ray on the ionosphere.

In Fig. 4 the observed percentage occurrence of scintillations is plotted against the common logarithm of the secant of the angle of incidence at the 400 km. level. It may be seen that the experimental points approximate a straight line, whose equation is:

$$\% \text{ occurrence} = 194 \log_{10} \sec \phi + 10.$$



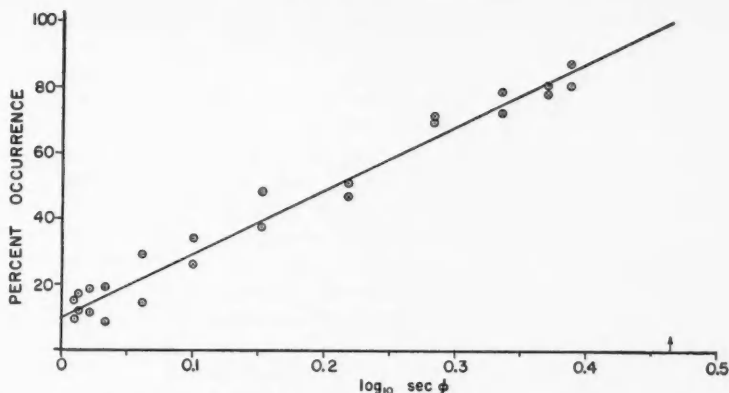


FIG. 4. The dependence of the percentage occurrence of scintillations on the logarithm of the secant of the angle of incidence on the 400 km. level of the ionosphere.

This may alternately be expressed as:

$$P = 1.94 \log_{10} \sec \phi + 0.1,$$

where  $P$  is the probability of observing scintillations from a source which subtends a zenith angle of  $\phi$  at the 400 km. level of the ionosphere. It follows that:

$$e^{1.19 P_1} = \sec \phi,$$

where  $P_1 = P - 0.1$  is the probability in excess of 0.1 of observing scintillations.

In Fig. 4 the line has been extrapolated to 100%. This point on the graph corresponds to an angle of incidence at the 400 km. level of  $70^\circ$ , which is the largest angle of incidence possible at this height if the ray is to reach the ground. It follows, then, that a radio star on or near the observer's horizon should always be scintillating.

#### B. Solar Dependence

The results of the record analysis have been summed for a year and plotted against solar time. In such a plot the sidereal component is disregarded since over a year its effect will be averaged out. The lower frame of Fig. 5 shows the percentage occurrence of scintillations as a function of local standard time. The rest of the diagram shows other observed geophysical phenomena for the same period. The ionospheric data are those obtained by vertical sounding at the Ottawa station with a conventional ionospheric sounder. The magnetic data are from the Agincourt observatory which is some 200 miles distant.

The second curve from the bottom of Fig. 5 is a plot of the percentage occurrence of high  $F2$  critical frequencies for the year; that is, the percentage of the observations that showed the  $F2$  critical frequency more than 15% above the monthly median. The third curve gives the percentage occurrence of spread  $F2$  echoes on the ionospheric recorder. The fourth curve shows the percentage occurrence of  $K$  indices greater than 3 for the Agincourt magnetic

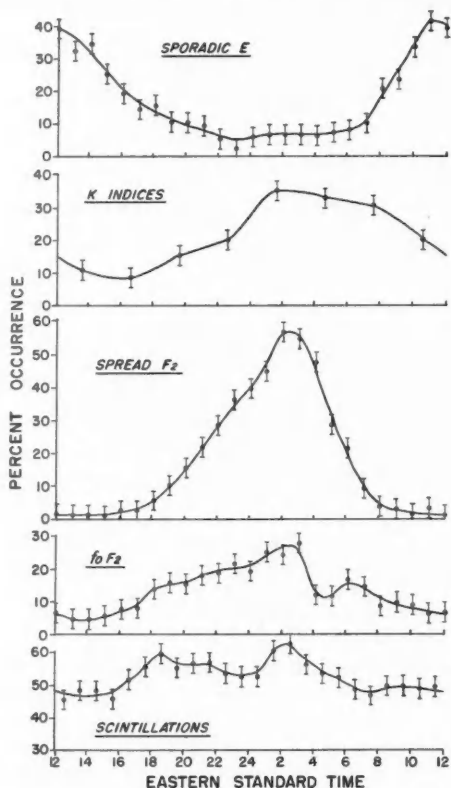


FIG. 5. The diurnal variation of the occurrence of scintillations, high  $F_2$  critical frequencies, spread  $F_2$  echoes, high  $K$  indices, and sporadic  $E$  echoes.

records. The last curve shows the percentage occurrence of sporadic  $E$  echoes on the ionospheric recorder. All curves are plotted against local standard time as indicated in the lower part of the figure. For each curve the standard deviation has been indicated.

The scintillation curve in Fig. 5 shows a higher occurrence of fluctuations at night than during the day, with two maxima, one before and one after midnight. Hewish (1) reported a similar nighttime maximum, but he also reported very low daytime values, which were not found in this investigation.

The  $F_2$  critical frequencies are a measure of the  $F_2$  layer ionization densities. A comparison of this curve with the scintillation curve shows a fairly close agreement on a yearly basis. In a similar manner it can be shown from the curves in Fig. 5 that the occurrence of spread  $F_2$  echoes averaged over a year

correlates positively with the occurrence of scintillations averaged over a year, as does the occurrence of large  $K$  indices. In each case there is a pronounced maximum after midnight. On the other hand, the occurrence of sporadic  $E$  echoes does not correlate positively with the occurrence of scintillations.

Correlation coefficients for the above relationships have not been given since on an hour-to-hour, or even day-to-day basis, the correlations are not as pronounced. Only a very slight positive correlation is found for each of high  $F2$  critical frequencies, spread  $F2$  echoes, and high  $K$  indices with the occurrence of scintillations indicating that no well-defined relationship exists.

In this connection several reservations must be made. The ionosphere data are obtained for the ionosphere overhead whereas the scintillation records are related to the ionosphere which is considerably to the north of Ottawa. The  $F2$  layer activity seems to correlate best with the scintillation records, but this layer is frequently obscured during disturbances by a lower layer and the data are thus missing just at times when they are likely to be most useful. The radio star fluctuation data probably pertain to a small-scale phenomenon such as may not be observable by means of the ionospheric recorder. However, the fact that there is a high positive correlation between  $F2$  layer activity and scintillation data taken over long periods of time indicates agreement between average ionospheric conditions in both cases. This alone would seem to indicate the region of the ionosphere active in the production of the scintillations to be the  $F2$  region. It would moreover also indicate that the region active in producing scintillations is one of considerable depth in the ionosphere as contrasted to the fairly well defined layer seen by the ionospheric recorder.

The agreement between  $F2$  layer activity and occurrence of scintillation can be shown in another way from the records. The fluctuation indices 0, 1, and 2 were used for record analysis, and the times of occurrence of index 2 noted. In a significant number of cases the corresponding ionospheric records indicated increased  $F2$  layer ionization or spread  $F2$  echoes. In other cases the times of occurrence of fluctuation index 2 corresponded only to a large angle of incidence.

### *C. Seasonal Dependence*

No significant seasonal dependence of occurrence of scintillations was observed during the 18 months for which records are available.

### SUMMARY

Records of the radiation at 50 Mc./s. from the intense source in the constellation of Cassiopeia for an 18 month period have been studied for the occurrence of scintillations. The probability of observing scintillations has been related to the angle of incidence on the 400 km. level of the ionosphere. The occurrence of scintillations has also been related to activity in the  $F2$  layer of the ionosphere when long-term averages are taken, but very little relationship is observed on a day-to-day basis. Considerably more work is necessary before this problem is resolved.

## ACKNOWLEDGMENTS

The author wishes to acknowledge the work of Mr. C. H. Costain who built the receiving system, Mr. J. Brown and Mr. W. A. Sharf who maintained and operated the equipment, and Mr. R. P. Mercier who made a preliminary survey of parts of the records. He would also like to thank Mr. E. L. Hagg for his advice on the ionospheric observations, and Dr. P. A. Forsyth for his interest and encouragement.

## REFERENCES

1. HEWISH, A. Proc. Roy. Soc. (London), A, 214: 494. 1952.
2. LITTLE, C. G. and LOVELL, A. C. B. Nature, 165: 423. 1950.
3. LITTLE, C. G. and MAXWELL, A. Phil. Mag. 42: 267. 1951.
4. RYLE, M. Proc. Roy. Soc. (London), A, 211: 351. 1952.
5. RYLE, M. and HEWISH, A. Monthly Notices Roy. Astron. Soc. 110: 381. 1950.
6. SMITH, F. G. Nature, 165: 422. 1950.

# AN AUDIO-FREQUENCY CIRCUIT MODEL OF THE ONE-DIMENSIONAL SCHROEDINGER EQUATION AND ITS SOURCES OF ERROR<sup>1</sup>

BY J. H. BLACKWELL, D. R. FEWER, L. J. ALLEN, AND R. S. CASS

## ABSTRACT

An audio-frequency circuit model of the one-dimensional Schroedinger equation has been constructed, based on original suggestions by G. Kron. The previous theory of such devices has been re-examined thoroughly and errors due to the basic finite-difference approximation separated from those due to electrical causes. It is found that the former type of error is likely to be dominant in practice and that in the past discrepancies due to errors of this kind have actually been ascribed to experimental causes.

## INTRODUCTION

An audio-frequency circuit model of the one-dimensional Schroedinger equation (3) has been constructed as an aid in solving vibrational problems arising in the spectroscopy of diatomic molecules, its design being based on original suggestions by Kron (4). The possible advantages of such a model over the use of analytical techniques are two-fold:

(i) if an adequate library of "potential function elements" (in our case, inductors) is available, the speed with which solutions to a given problem are obtained is independent of the analytical form of the potential function and in general more rapid than numerical or analytical methods;

(ii) the reaction on eigenvalues and eigenfunctions of small modifications to the constants and/or form of a given potential function may be tested very rapidly.

The former and, to a lesser extent, the latter of these considerations presupposes adequate accuracy on the part of the model, and the authors have thoroughly re-examined the theory of such devices from the viewpoint of error determination.

## PRINCIPLES OF OPERATION

In its ideal form, the model can be considered as an artificial and (generally) non-uniform transmission line of pure reactive elements.

When excited from an external a-c. voltage source applied across the line, say at  $AB$ , the current flowing into the network is in general finite, but is zero when the network is set in voltage resonance by suitable adjustment of the ganged equal admittances  $Y_w$ .

At voltage resonance the difference equation relating adjacent shunt voltages  $\epsilon_k$  is

$$[1] \quad \epsilon_{k+1} - \left( 2 + \frac{|Y_{vk}| - |Y_w|}{|Y_H|} \right) \epsilon_k + \epsilon_{k+1} = 0$$

<sup>1</sup>Manuscript received March 18, 1955.

Contribution from Department of Physics, University of Western Ontario, London, Canada.

where the symbols are as shown in Fig. 1 and  $|Y_w|$  is the eigenvalue of the difference equation.

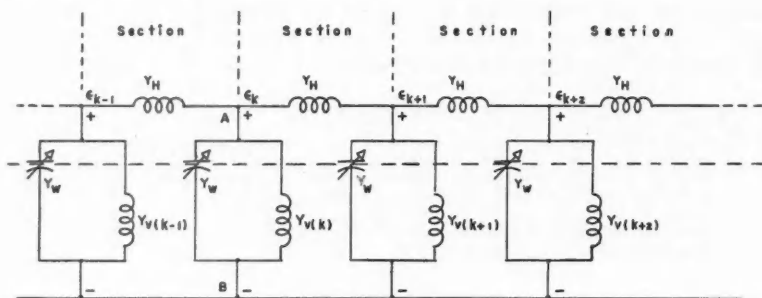


FIG. 1.

Introduce the quantities  $V_k$ ,  $W$ ,  $\kappa$ ,  $\Delta x$  such that

$$\frac{V_k}{|Y_{vk}|} = \frac{W}{|Y_w|} = \frac{1}{\kappa(\Delta x)^2 |Y_H|} = K, \quad \text{a scaling constant,}$$

and replace  $\epsilon$  by  $\psi$ . Equation [1] then becomes

$$[2] \quad \psi_{k+1} - [2 + (\Delta x)^2 (V_k - W)] \psi_k + \psi_{k-1} = 0$$

where  $\kappa$ ,  $\Delta x$  are constants and  $W$  is the eigenvalue.

Making the substitution  $x = k\Delta x$  and approximating equation [2] by Taylor's theorem (to second order in  $\Delta x$ ) we get

$$[3] \quad -\frac{1}{\kappa} \frac{d^2 \psi}{dx^2} + V(x) \psi = W \psi,$$

the one-dimensional Schroedinger equation.

We can thus use electrical solutions of equation [1] to approximate solutions of equation [3] for small  $\Delta x$ .

In a practical network the parameters are not lossless and the condition of zero current is replaced by that of zero reactive current, i.e., zero phase difference between applied voltage and input current.

The original experimental work on this idea by Carter and Kron (2) was done on a low-frequency network analyzer. The prototype model constructed by the authors was designed to operate at a fixed frequency of 10 kc./s., in order to reduce both size and cost, and contained 24 "sections". The eigenvalue admittances  $Y_w$  were represented by a set of ganged variable capacitors and  $Y_H$  and  $Y_{vk}$  by suitable inductors.

#### SOURCES OF ERROR

Errors in such a circuit model are of two distinct types, the basic "finite difference" error due to approximation of a differential equation by a difference equation, and true experimental errors due to coil losses, stray capacitance and inductance, inaccurate voltage measurement, etc.

In order to separate the two types it is convenient to compare results from the model for selected potential functions  $V(x)$  with the corresponding calculated *difference* equation solutions. It has been noted that in previous work on this type of circuit model, discrepancies in experimental results had been attributed wholly to electrical causes when in fact they had been due largely to the finite-difference approximation; in order to avoid this, the difference equations for the following typical potential functions were solved:

- I. Infinite well— $V(x) = 0 \quad |x| < a$   
 $\quad \quad \quad = \infty \quad |x| > a$
- II. Square well with one infinite wall— $V(x) = \infty \quad x < 0$   
 $\quad \quad \quad = 0 \quad 0 < x < a$   
 $\quad \quad \quad = V_0 \quad a < x < \infty$
- III. Harmonic oscillator— $V(x) = \frac{1}{2} kx^2 \quad -\infty < x < \infty$

It was felt that, together, these functions possessed the principal features of most potentials (e.g., the Morse) which the model (or an improved version) would be called upon to solve in practice. Cases I and II were solved using standard methods for linear constant-coefficient difference equations and in case II solutions were matched at  $x = a$  as in the differential equation case. Case III required the method of continued fractions (6, 1) and much laborious numerical work. The analysis is given in abbreviated form in Appendix A.

#### EXPERIMENTAL RESULTS

Comparison of theory with experiment was illuminating. In several experimental situations "difference" eigenvalues were very much greater or less than the corresponding "differential" eigenvalues, but although the model was of relatively crude electrical design, the discrepancy between experimental and difference equation eigenvalues was generally smaller than 1%. This discrepancy could be further reduced by the type of variational calculation suggested by Kron (5); it must be remembered however that the result of such a calculation approximates the *difference* equation eigenvalue, not that of the *differential* equation as might be inferred from his article.

Tables showing differential equation, difference equation, and experimental eigenvalues for the different types of potential function tested are given in Appendix B.

The principal experimental errors showed up in departures from difference equation theory at very low eigenvalues (low capacity of the variable capacitors) and at high eigenvalues. The former error was due to large stray capacitances which could not be compensated for in calibration of the variable capacitors. The latter was due to finite coil resistance and the consequent fact that circuit resonance in the practical, as against the ideal, system is affected by the location of the external voltage source. This point is fully discussed by Carter and Kron.

It is concluded from the theoretical and experimental studies made that considerable care must be taken in deciding how small ' $\Delta x$ ' need be for the "finite-difference" error to be negligible. This error is found to be a function

not only of the number of "sections" available to represent the Schroedinger equation for a given interval of the  $x$ -axis, but also of the shape of the potential and of the "quantum number". However, when the finite-difference error has been minimized, relatively little care in electrical design will result in high accuracy (better than 1%) in eigenvalues and eigenfunction amplitudes.

Sufficient information has been obtained to permit the design of an improved network of high accuracy and this design is approaching completion. It will include a new physical layout and switching arrangement for the decade capacitors to minimize the error due to stray capacitance at low eigenvalues; coil  $Q$ 's will be increased, better quality capacitors employed, and circuit losses generally reduced in order to reduce the electrical error at large quantum numbers.

#### CONCLUSION

It is considered that the work described may be of interest to those concerned with similar circuit models and, in particular, the analysis of Appendix A may be useful in the general field of numerical solutions of the Schroedinger equation.

#### ACKNOWLEDGMENTS

The authors would like to express their gratitude to Dr. G. P. Henderson, Department of Mathematics, University of Western Ontario, for suggesting the method of continued fractions used in Appendix A, Case III, and assisting in its application.

The research reported in this paper has been made possible through the support and sponsorship extended by the Geophysics Research Division of the Air Force Cambridge Research Centre, under Contract No. AF 19(122)-470.

#### REFERENCES

1. ALLEN, L. J. M.Sc. Thesis, University of Western Ontario, London, Ont. 1954.
2. CARTER, G. K. and KRON, G. Phys. Rev. 67: 44. 1945.
3. FEWER, D. R., ALLEN, L. J., and BLACKWELL, J. H. Sci. Rept. No. 15, Contract AF 19(122)-470. Dept. of Phys., University of Western Ontario, London, Ont.
4. KRON, G. Phys. Rev. 67: 39. 1945.
5. KRON, G. J. Appl. Phys. 16: 185. 1945.
6. MILNE-THOMPSON, L. M. The calculus of finite differences. McMillan & Co., Ltd., London. 1933, p. 378.
7. SCHIFF, L. I. Quantum mechanics. McGraw-Hill Book Company, Inc., New York. 1949.

#### APPENDIX A. ANALYSIS

##### Cases I and II

For case I there is a single constant-coefficient difference equation. In case II, there is one of these equations for each region of the potential, solutions being matched at the boundary using the conditions given below.

##### Case I.—The Infinite Potential Well

We have  $V_k = 0$ ,  $1 \leq k \leq N$ ,  
 $V_k = \infty$ ,  $k = 0, N+1$ ,

where the width of the well  $a = (N+1)\Delta x$ .



The difference equation [2] may be written

$$[4] \quad \{E^2 + (\alpha_n^2 - 2)E + 1\} \psi_k = 0,$$

where the operator  $E$  is defined by

$$Ef_k = f_{k+1}$$

and

$$\alpha_n = \sqrt{\kappa(\Delta x)^2 W} \quad (\text{independent of } k).$$

The solution of this equation subject to the boundary conditions

$$\psi_0 = \psi_{N+1} = 0$$

is

$$[5] \quad \psi_k = A \sin\left(\frac{nk\pi}{N+1}\right) \quad (n = 1, 2, \dots, N+1)$$

together with

$$[6] \quad \alpha_n^2 = 4 \sin^2\left(\frac{n\pi}{2(N+1)}\right).$$

The eigenvalues of the corresponding differential equation are given by

$$W = n^2 \pi^2 / \kappa a^2 \quad (n = 1, 2, \dots).$$

To compare these with the eigenvalues given by the difference equation, we may write equation [6] as

$$W = \frac{4}{\kappa(\Delta x)^2} \sin^2\left(\frac{n\pi\Delta x}{2a}\right).$$

It should be noted that, while the differential equation has an infinite number of eigenvalues, the difference equation has only a finite number (i.e.,  $N+1$ ).

It can be seen that as  $\Delta x \rightarrow 0$ , the solutions of the difference equation approach the solutions of the differential equation.

#### Case II.—The Rectangular Well with One Infinite Wall

In order to solve the difference equation,  $\psi$  is divided into two portions

$$\begin{aligned} &= \psi_k^I \quad \text{for } 0 \leq k \leq N+1, \\ &= \psi_k^{II} \quad \text{for } N \leq k, \end{aligned} \quad a = (N+1)\Delta x,$$

and the solution is obtained for  $0 < W < V_0$ , where  $V_0$  is the height of the finite side of the well (i.e., bound states).

The difference equation for  $\psi_k^I$  is identical with that of the infinite well. The difference equation for  $\psi_k^{II}$  may be written

$$[7] \quad \{E^2 - (\beta_n^2 + 2)E + 1\} \psi_k^{II} = 0,$$

where

$$\beta_n = \sqrt{\kappa(\Delta x)^2 (V_0 - W)} \quad (\text{which is independent of } k).$$

The boundary conditions are given by

$$(1) \quad \psi_0^I = 0,$$

$$(2) \quad \psi_\infty^{II} = 0,$$

$$(3) \quad \psi_N^I = \psi_N^{II},$$

$$(4) \quad \psi_{N+1}^I = \psi_{N+1}^{II}.$$

The last two conditions reduce in the limit to continuity of the function and its first derivative.

Application of these boundary conditions gives the following expressions for the eigenfunctions and eigenvalues of the rectangular well:

$$[8] \quad \psi_k^I = C_1 \sin \left[ k \tan^{-1} \left( \frac{\alpha_n \sqrt{4 - \alpha_n^2}}{2 - \alpha_n^2} \right) \right],$$

$$[9] \quad \psi_k^{II} = C_2 \exp(-k \ln \sigma_n),$$

where

$$\sigma_n = \frac{1}{2}(\beta_n^2 + 2 + \beta_n \sqrt{\beta_n^2 + 4}).$$

For  $W \ll V_0$

$$[10] \quad W \approx \frac{4}{\kappa(\Delta x)^2} \sin^2 \frac{n\pi\Delta x}{2a} \left[ 1 - \frac{(1/n\pi) \sin(n\pi\Delta x/a)}{\sigma - (1 - \Delta x/a) \cos(n\pi\Delta x/a)} \right],$$

where

$$\sigma = \frac{1}{2}(\beta^2 + 2 + \beta \sqrt{\beta^2 + 4}),$$

$$\beta = \sqrt{\kappa(\Delta x)^2 V_0}.$$

The solutions of the corresponding differential equation are given by (see reference (7))

$$[11] \quad \psi^I(x) = A_1 \sin \gamma x,$$

$$[12] \quad \psi^{II}(x) = A_2 \exp(-\delta(x-a)),$$

where

$$\gamma = \sqrt{\kappa W},$$

$$\delta = \sqrt{\kappa(V_0 - W)}.$$

For  $W \ll V_0$

$$[13] \quad W \approx \frac{n^2 \pi^2}{\kappa a^2} \left[ 1 - \frac{1}{1 + a \sqrt{\kappa V_0}} \right]^2.$$

In the limit  $\Delta x \rightarrow 0$ , equations [8], [9], [10] approach equations [11], [12], [13] as required.

It will be noted that eigenvalues are compared only for the special case  $W \ll V_0$ . Although for both differential and difference equations, the eigenvalues are given by the roots of transcendental equations, it is possible to obtain approximate explicit solutions in each case for  $W \ll V_0$ . It is considered that for purposes of demonstration equation [10] is more useful than the exact but complex transcendental equation from which it is derived.

*Case III.—The Linear Harmonic Oscillator*

The potential function for the linear harmonic oscillator is of the form

$$V_k = \frac{1}{2} L k^2 (\Delta x)^2$$

where  $L$  is the "force constant", and the difference equation for this case may be written

$$[14] \quad \psi_{k+1} + (\lambda - \sigma^2 k^2) \psi_k + \psi_{k-1} = 0,$$

where  $\lambda = \kappa(\Delta x)^2 W - 2$ , and  $\sigma^2 = \frac{1}{2} L \kappa (\Delta x)^4$ .

It can be shown, as for the corresponding differential equation, that the only well-behaved solutions have even or odd parity.

Solutions are obtained using the method of continued fractions (6) as follows. Let there be two independent solutions:  $X_k$  defined by  $X_0 = 0$ ,  $X_1 = 1$ , and  $Y_k$  defined by  $Y_0 = 1$ ,  $Y_1 = 0$ .

It can easily be shown that:

$$X_{-k} = -X_k$$

and  $Y_{-k} = -\lambda X_k + Y_k$ .

Then the even solutions of [14] are given by:

$$[15] \quad \psi_{ek} = A_e [2 Y_k - \lambda X_k]$$

and the odd solutions by:

$$[16] \quad \psi_{ok} = A_o X_k.$$

Applying the condition that these solutions be bounded at infinity, we obtain the eigenvalue equation for even solutions

$$[17] \quad \frac{\lambda}{2} = \frac{-1}{\sigma^2 - \lambda + 4} \frac{-1}{\sigma^2 - \lambda + 4} \cdots \frac{-1}{k^2 \sigma^2 - \lambda + 4} \cdots$$

and for the odd solutions

$$[18] \quad \lambda = \sigma^2 + \frac{-1}{4\sigma^2 - \lambda + 4} \frac{-1}{9\sigma^2 - \lambda + 4} \cdots \frac{-1}{k^2 \sigma^2 - \lambda + 4} \cdots$$

where the right-hand side of each equation is a continued fraction.

These two equations are then solved numerically for  $\lambda$  (and hence  $W$ ) by successive approximations, using as a first approximation the eigenvalue of the corresponding differential equation, i.e.,

$$W = (n + \frac{1}{2}) \sqrt{2L/\kappa} \quad (n = 0, 1, 2, \dots).$$

The eigenfunctions are calculated by forming  $\psi_0$  and  $\psi_1$  and then employing [14] as a recursion relation, i.e.,

$$\psi_{k+1} = -(\lambda - \sigma^2 k^2) \psi_k - \psi_{k-1}.$$

## APPENDIX B

Theoretical eigenvalues for both differential and difference equations together with the experimental values obtained are tabulated below for the potentials tested. The constants of the network are stated in mhos, the eigenvalues in micromicrofarads.

## (a) THE INFINITE WELL

$n$	Differential equation $\mu\mu f.$	Difference equation $\mu\mu f.$	Experimental values $\mu\mu f.$
(1) $ Y_H  = 4.521 \times 10^{-3}$ mho, $a = \text{well-width} = 20 \Delta x$			
1	1780	1770	1900
2	7120	7060	7100
3	16000	15700	15600
4	28500	27500	27400
5	44500	42200	42000
6	64100	59400	59100
7	87200	78700	78200
8	113900	99600	101000
9	144200	121600	124000
10	178000	144100	147200
(2) $ Y_H  = 2.546 \times 10^{-3}$ mho, $a = 15 \Delta x$			
1	1780	1770	1800
2	7120	7010	6900
3	16000	15500	15300
4	28500	26800	26500
5	44500	40500	39700
6	64100	56000	55100
7	87200	72600	74200
8	113900	89500	90600
9	144200	106100	108200
10	178000	121600	123600
(3) $ Y_H  = 1.629 \times 10^{-3}$ mho, $a = 8 \Delta x$			
1	7110	7070	7100
2	28400	27500	27400
3	64000	59400	59200
4	113800	99600	98900
5	177800	144100	143600
6	256000	183700	185400

## (b) SQUARE WELL WITH ONE INFINITE WALL

$|Y_{v0}| = 0.1532 \text{ mho}$

$n$	Differential equation $\mu\mu f.$	Difference equation $\mu\mu f.$	Experimental values $\mu\mu f.$
(1) $ Y_H  = 4.521 \times 10^{-3}$ mho, $a = 13 \Delta x$			
1	3940	4090	4200
2	15800	16200	16200
3	35500	35500	35500
4	63100	61200	60800
5	98600	91700	91400
(2) $ Y_H  = 2.546 \times 10^{-3}$ mho, $a = 10 \Delta x$			
1	3750	3900	4000
2	15000	15200	15100
3	33800	33000	32700
4	60100	55400	54800
5	93800	80300	78900
(3) $ Y_H  = 1.629 \times 10^{-3}$ mho, $a = 8 \Delta x$			
1	3750	3890	3900
2	15000	15000	14800
3	33800	31700	31400
4	60100	51500	51000
5	93800	71400	70400

## (c) LINEAR HARMONIC OSCILLATOR

$n$	Differential equation $\mu\text{mf.}$	Difference equation $\mu\text{mf.}$	Experimental values $\mu\text{mf.}$
(1) $ Y_H  = 4.521 \times 10^{-3} \text{ mho},  Y_{v_k}  = 0.825 \times 10^{-3} k^2 \text{ mho}$			
0	32500	31600	31900
1	94000	89600	89900
2	155500	144100	144000
3	217000	194000	193600
4	278500	238200	237100
5	340050	280300	281900
(2) $ Y_H  = 2.546 \times 10^{-3} \text{ mho},  Y_{v_k}  = 1.466 \times 10^{-3} k^2 \text{ mho}$			
0	32500	30900	31500
1	94000	86200	85600
2	155500	130100	129900
3	217000	182400	179200

## LETTERS TO THE EDITOR

*Under this heading brief reports of important discoveries in physics may be published. These reports should not exceed 600 words and, for any issue, should be submitted not later than six weeks previous to the first day of the month of issue. No proof will be sent to the authors.*

### Correction to: The Hyperfine Structure of Mercury Extracted from Neutron-irradiated Gold\*

We have been advised by Drs. R. E. Bell, R. L. Graham, and L. Yaffe that the neutron capture cross section,  $\sigma_1$ , for  $\text{Au}^{198}$  obtained in the above paper should be corrected for (1) finite irradiation time and (2)  $\text{Hg}^{199}$  "burnout" during irradiation. Certainly both these corrections were omitted from our considerations, the first intentionally since the irradiation schedule was not exactly known and we estimated its effect as being of the same magnitude as the uncertainty in the flux (20%). However if one assumes continuous irradiation in a constant flux  $F$  for a time  $T$  ( $10^8$  sec.) then, neglecting (2),

$$\frac{\text{Hg}^{199}}{\text{Hg}^{198}} = \left( \frac{\sigma_1 F}{\lambda_1} \right) \left\{ \frac{T - [1 - e^{-\alpha T}]/\alpha}{T + (\sigma_1 F/\lambda_1)[1 - e^{-\alpha T}]} \right\},$$

where  $\sigma_1 = 2.6 \times 10^4$  barns,  $F = 4.6 \times 10^{13}$  neutrons  $\text{cm}^{-2} \text{sec}^{-1}$ ,  $\lambda_1 = 0.298$  ( $10^5 \text{ sec.}$ ) $^{-1}$ ,  $\alpha = (\lambda_1 + \sigma_1 F) = 0.418$  ( $10^8 \text{ sec.}$ ) $^{-1}$ . The correction factor in braces for  $T = 11.48 \times 10^8 \text{ sec.} \approx 320$  hr. amounts to 0.733.

Regarding the neutron capture by the  $\text{Hg}^{199}$  formed during irradiation, this effect leads to a correction which is considerably smaller for short irradiation times. We estimate it, under the above conditions, to amount to  $9 \pm 2\%$ . Both these corrections make the observed ratio  $\text{Hg}^{199}/\text{Hg}^{198}$  smaller than the value  $\sigma_1 F/\lambda_1$ .

Our value of  $\sigma_1$  for pile neutrons, with these two corrections included, amounts to

$$1.78 \times 10^4 \times 1.09 / 0.733 = 2.64 \times 10^4 \text{ barns.}$$

We understand that this value is very close to the value† of Drs. Bell, Graham, and Yaffe to whom we are much indebted for a prepublication notice of their results and for their communication of the above correction factors.

RECEIVED MARCH 7, 1955.  
DEPARTMENT OF PHYSICS,  
UNIVERSITY OF BRITISH COLUMBIA,  
VANCOUVER 8, BRITISH COLUMBIA.

R. E. BEDFORD  
A. M. CROOKER

\**Can. J. Phys.* 33: 25. 1955.

†*Can. J. Phys.* 33: 457. 1955.

## THE PHYSICAL SOCIETY

MEMBERSHIP of the Society is open to all who are interested in Physics.

FELLOWS pay an Entrance fee of £1 1s. (\$3.00) and an Annual Subscription of £2 2s. (\$6.00).

STUDENTS: A candidate for Studentship must be between the ages of 18 and 26, and pays an Annual Subscription of 7s. 6d. (\$1.10).

MEETINGS: Fellows and Students may attend all Meetings of the Society including the annual Exhibition of Scientific Instruments and Apparatus.

PUBLICATIONS include the *Proceedings of the Physical Society*, published monthly in two sections, and *Reports on Progress in Physics*, published annually. Volume XVII, 1954, is now available (price 50s. (\$7.15)). Members are entitled to receive many of the Publications at a reduced rate.

Further information can be obtained from:

THE PHYSICAL SOCIETY  
1, LOWTHER GARDENS, PRINCE CONSORT ROAD  
LONDON, S.W.7, ENGLAND





# CANADIAN JOURNAL OF PHYSICS

## Notes to Contributors

### Manuscripts

(i) **General.** Manuscripts, in English or French, should be typewritten, double spaced, on paper  $8\frac{1}{2} \times 11$  in. **The original and one copy are to be submitted.** Tables and captions for the figures should be placed at the end of the manuscript. Every sheet of the manuscript should be numbered.

Style, arrangement, spelling, and abbreviations should conform to the usage of this journal. Names of all simple compounds, rather than their formulas, should be used in the text. Greek letters or unusual signs should be written plainly or explained by marginal notes. Superscripts and subscripts must be legible and carefully placed.

Manuscripts and illustrations should be carefully checked before they are submitted. Authors will be charged for unnecessary deviations from the usual format and for changes made in the proof that are considered excessive or unnecessary.

(ii) **Abstract.** An abstract of not more than about 200 words, indicating the scope of the work and the principal findings, is required, except in Notes.

(iii) **References.** References should be listed **alphabetically by authors' names**, numbered, and typed after the text. The form of the citations should be that used in this journal; in references to papers in periodicals, titles should not be given and only initial page numbers are required. All citations should be checked with the original articles and each one referred to in the text by the key number.

(iv) **Tables.** Tables should be numbered in roman numerals and each table referred to in the text. Titles should always be given but should be brief; column headings should be brief and descriptive matter in the tables confined to a minimum. Vertical rules should be used only when they are essential. Numerous small tables should be avoided.

### Illustrations

(i) **General.** All figures (including each figure of the plates) should be numbered consecutively from 1 up, in arabic numerals, and each figure referred to in the text. The author's name, title of the paper, and figure number should be written in the lower left corner of the sheets on which the illustrations appear. Captions should not be written on the illustrations (see Manuscripts (i)).

(ii) **Line Drawings.** Drawings should be carefully made with India ink on white drawing paper, blue tracing linen, or co-ordinate paper ruled in blue only; any co-ordinate lines that are to appear in the reproduction should be ruled in black ink. Paper ruled in green, yellow, or red should not be used unless it is desired to have all the co-ordinate lines show. All lines should be of sufficient thickness to reproduce well. Decimal points, periods, and stippled dots should be solid black circles large enough to be reduced if necessary. Letters and numerals should be neatly made, preferably with a stencil (**do NOT use typewriting**) and be of such size that the smallest lettering will be not less than 1 mm. high when reproduced in a cut 3 in. wide.

Many drawings are made too large; originals should not be more than 2 or 3 times the size of the desired reproduction. In large drawings or groups of drawings the ratio of height to width should conform to that of a journal page but the height should be adjusted to make allowance for the caption.

**The original drawings and one set of clear copies (e.g. small photographs) are to be submitted.**

(iii) **Photographs.** Prints should be made on glossy paper, with strong contrasts. They should be trimmed so that essential features only are shown and mounted carefully, with rubber cement, on white cardboard with no space or only a **very** small space (less than 1 mm.) between them. In mounting, full use of the space available should be made (to reduce the number of cuts required) and the ratio of height to width should correspond to that of a journal page ( $4\frac{1}{2} \times 7\frac{1}{4}$  in.); however, allowance must be made for the captions. Photographs or groups of photographs should not be more than 2 or 3 times the size of the desired reproduction.

**Photographs are to be submitted in duplicate**; if they are to be reproduced in groups one set should be mounted, the duplicate set unmounted.

### Reprints

A total of 50 reprints of each paper, without covers, are supplied free. Additional reprints, with or without covers, may be purchased.

Charges for reprints are based on the number of printed pages, which may be calculated approximately by multiplying by 0.6 the number of manuscript pages (double-spaced typewritten sheets,  $8\frac{1}{2} \times 11$  in.) and including the space occupied by illustrations. An additional charge is made for illustrations that appear as coated inserts. The cost per page is given on the reprint requisition which accompanies the galley.

Any reprints required in addition to those requested on the author's reprint requisition form must be ordered officially as soon as the paper has been accepted for publication.

## Contents

	Page
A Study of Nucleon Forces with Repulsive Cores. I. The Effect of Cores of Finite Strength— <i>J. R. Bird and M. A. Preston</i> - - -	399
Diffraction of Microwaves by Long Metal Cylinders— <i>Albert W. Adey</i>	407
The Viscosity of Liquid Helium II— <i>W. J. Heikkila and A. C. Hollis Hallett</i> - - - - -	420
Some Considerations Regarding the Principle of Phase Invariance— <i>F. A. Kaempffer</i> - - - - -	436
Capture Radiation and Neutrons from the Bombardment of $^{14}\text{C}$ with Protons— <i>G. A. Bartholomew, F. Brown, H. E. Gove, A. E. Litherland, and E. B. Paul</i> - - - - -	441
The Thermal Neutron Capture Cross Section of $\text{Au}^{198}$ and the Half-life of $\text{Au}^{199}$ — <i>R. E. Bell, R. L. Graham, and L. Yaffe</i> - - -	457
The Initial Oxidation of Nickel— <i>Ursula M. Martius</i> - - - -	466
A Method of Examining Structural Changes of Metals on Deformation in Liquid Helium: Examination of Indium— <i>W. B. Pearson</i>	473
Radio Star Scintillations and the Ionosphere— <i>T. R. Hartz</i> - - -	476
An Audio-frequency Circuit Model of the One-dimensional Schrodinger Equation and Its Sources of Error— <i>J. H. Blackwell, D. R. Fewer, L. J. Allen, and R. S. Cass</i> - - - - -	483
 Letter to the Editor:	
Correction to: The Hyperfine Structure of $^{201}\text{Hg}$ Mercury Extracted from Neutron-irradiated Gold— <i>R. E. Bedford and A. M. Crooker</i>	492

